UNIVERSITY *of the*
WESTERN CAPE

Nuclear level densities and gamma-ray strength functions in Ta isotopes and nucleo-synthesis of ^{180}Ta

UNIVERSITY of the
WESTERN CAPE

KGASHANE LEROY MALATJI

A thesis presented in partial fulfillment of the requirements for the degree of Master of Science in the Department of Physics, University of the Western Cape.

Supervisor: Dr. M. Wiedeking (iThemba LABS)
Co-supervisors: Dr. B.V. Kheswa (iThemba LABS and University of Oslo)
Prof. S. Triambak (University of the Western Cape)

February 2016

Nuclear level densities and gamma-ray strength functions in Ta isotopes and nucleo-synthesis of ^{180}Ta

Kgashane Leroy Malatji

UNIVERSITY of the
WESTERN CAPE

Keywords

Nuclear level density
γ-ray strength function
Astrophysical network calculations
Nucleosynthesis
(n, γ) cross sections

Abstract

Nuclear level densities and gamma-ray strength functions in Ta isotopes and nucleo-synthesis of ^{180}Ta

Kgashane Leroy Malatji

UNIVERSITY of the
WESTERN CAPE

Most stable and extremely low abundance neutron deficient nuclei with $Z \geq 34$ are referred to as p-nuclei. Nearly all p-nuclei with A < 110 are most likely produced in the rp-process while almost all A > 110 are thought to be produced by the photodisintegration of s- and r-process seed nuclei. However, for some nuclear systems, these processes are not sufficient to explain their observed solar abundance. Results from calculations in ^{180}Ta generally provoke debates since several processes are able, sometimes exclusively, to reproduce the observed ^{180}Ta abundance in the cosmos, making it a unique case study. Some of the main sources of errors in the predicted reaction rates of ^{180}Ta arise due to the absence of nuclear data or due to large uncertainties in the nuclear properties such as the nuclear level densities (NLD) and gamma-ray strength functions (γSF) of ^{180,181}Ta. The NLD and γSF are primary ingredients for astrophysical reaction rate calculations based on the Hauser-Feshbach approach. These parameters need to be well understood to improve our understanding of ^{180}Ta production in astrophysical environments. In this thesis, new experimental data for the low-energy part of the γSF and NLD in ^{180,181}Ta were extracted, using the so-called Oslo method. An experiment was performed and the NaI(Tl) gamma-ray array and silicon particle telescopes at the Oslo cyclotron laboratory were utilized to measure particle-γ coincidence events from which the NLDs and γSFs are extracted below the neutron separation energy threshold S_n. A beam of

^{3}He was used to populate excited states in ^{180,181}Ta through the inelastic scattering (^{3}He,^{3}He'γ) and the transfer reaction (^{3}He,$\alpha\gamma$). Based on results from this measurements, the Maxwellian-averaged (n,γ) cross sections for the ^{179}Ta(n,γ) and ^{180}Ta(n,γ) reactions, at the s-process thermal energy of $kT = 30$ keV (i.e. a temperature of T $= 3.5 \times 10^{8}$ K) and p-process thermal energy of 215 keV (T $= 2.5 \times 10^{9}$ K), respectively, were computed with the TALYS reaction code. These results can be used to place the nuclear physics aspects of the large network abundance calculations on a solid footing and have potential to improve our understanding of the astrophysical processes and sites involved in the production of nature's rarest isotope ^{180}Ta.

UNIVERSITY of the
WESTERN CAPE

Declaration

I declare that *Nuclear level densities and gamma-ray strength function in Ta isotopes and nucleo-synthesis of* ^{180}Ta is my own work, that it has not been submitted for any degree or examination in any other university, and that all the sources I have used or quoted have been indicated and acknowledged by complete references.

Full Name: Kgashane Leroy Malatji Date: February 2016

Signed:.....

Dedication

I dedicate this work to my late father Machete Mphaka Wilson Malatji (1965-1998) whose courage has inspired me so far, to my mother and my pillar of strength Joyce Mmabodimo Malatji (Mologadi), and finally to my supportive brothers Mpho Egnecious, Malemela Marcus and Thato Arnold Malatji.

UNIVERSITY of the
WESTERN CAPE

Acknowledgements

My deepest gratitude goes to the creator of all things, for his unconditional and unchanging grace upon my life.

I would like to express my appreciation to my main supervisors Dr. Mathis Wiedeking and Dr. Bonginkosi Vincent Kheswa from iThemba LABS for their encouragement and guidance throughout the course of the MANUS program.

I would like to thank the National Research Foundation (NRF) for financial support during my studies and also for funding my international trips during the second year of my studies.

I am deeply grateful for iThemba LABS physics staff, more especially the AFRODITE group for their support, motivation and encouragement during the hardship of this program.

Many thanks to Dr. Ann-Cecilie Larsen and Prof. Magne Sveen Guttormsen from the University of Oslo, for such constructive discussions and guidance during the data analysis.

I am very thankful to the University of the Western Cape (UWC) physics group for their support, more especially Prof. Nico Orce and Mr JM Mokgolobotho for their motivation and helpful discussions.

Special thanks go to my office mates at iThemba LABS, thanks for your support, resourceful discussions and the good times we had during the course of the year.

I would like to thank the MSc students Bonginkosi Richard Zikhali and Christiaan Petrus Brits, who were also working on the Oslo data. Thanks for all the discussions we had.

I would like to thank my girlfriend for her encouragement and understanding when I was working on weekends and when I was in Russia attending the SA-JINR student practice for a month. Many thanks to my friends Mokono Paul Mamabolo, Machel Mmola and Tiisetso Makheane Moimane for their support as well.

UNIVERSITY of the
WESTERN CAPE

Thanks to my co-supervisor Prof. Smarajit Triambak from UWC for helping out with university administration applications.

Dr. Bonginkosi Vincent Kheswa thank you for the advices and patience during data analysis, you made this work feel lighter and most of all thanks for the friendship we accomplished.

Dr. Mathis Wiedeking many thanks for the support and encouragement during the course of the thesis. Thank you for granting me the opportunity to work on such an interesting project and allowing me to attend the 3rd SA-China symposium on nuclear physics and also to attend the 2016 SA-JINR student practice.

Last but not least, I would like to thank my family for understanding and supporting me always. My mother Joyce Mmabodimo, and my brothers Mpho Egnecious, Malemela Marcus and Thato Arnold Malatji, for their love and prayers. Thanks for allowing me to study in the Western Cape province and to travel the world.

Contents

UNIVERSITY of the
WESTERN CAPE

UNIVERSITY of the WESTERN CAPE

UNIVERSITY of the
WESTERN CAPE

List of Figures

UNIVERSITY of the
WESTERN CAPE

UNIVERSITY of the WESTERN CAPE

UNIVERSITY of the WESTERN CAPE

UNIVERSITY of the
WESTERN CAPE

UNIVERSITY of the
WESTERN CAPE

List of Tables

UNIVERSITY of the
WESTERN CAPE

Chapter 1

Introduction

Nuclear physics is fundamental to understanding the astrophysical phenomenon such as nucleosynthesis of light elements, the creation of elements heavier than iron, and neutron stars. In particular nucleosynthesis of elements heavier than iron is one of the 11 most urgent topics in physics to be addressed, as reported in The National Academic Press [1]. Knowledge of elemental abundances is mainly obtained from observations within our solar system and, to a lesser extent, galaxy. Iron and nickel are the final products of stellar burning and are considered the seed nuclei for the production of heavier nuclei. Initially O/Ne-rich layers of core-collapse supernovae events were thought to provide the astrophysical environments necessary to synthesize heavy nuclei. However, new calculations suggest that suitable environments are found elsewhere, for example in the ejecta of neutron star mergers [2] and when the outer layer of a proto-neutron star is blown off in neutrino driven winds [3] following a supernova event. The main astrophysical processes that are invoked in the nucleosynthesis of heavier elements are (i) the rapid neutron-capture (r-process), (ii) rapid proton capture (rp-process) which occurs in high temperatures and proton-rich environments, (iii) slow neutron capture (s-process) which is responsible for almost half of the observed abundance of nuclei heavier than iron, (iv) neutrino capture (ν-process) and (v) photodisintegration (p-process). The paths of rp-, p- and r-processes are shown in figure 1.1.

For a full understanding of the evolution of abundances a wealth of nuclear data is necessary. The production rates do not only depend on beta-decay half-lives and nuclear masses but also sensitively on the γ-ray strength function, γSF, and nuclear level density, NLD, due to their central role in nuclear reactions. Often, when these statistical nuclear properties are known with low errors, the uncertainties in (n, γ) cross sections can potentially be reduced by more than an

UNIVERSITY of the WESTERN CAPE

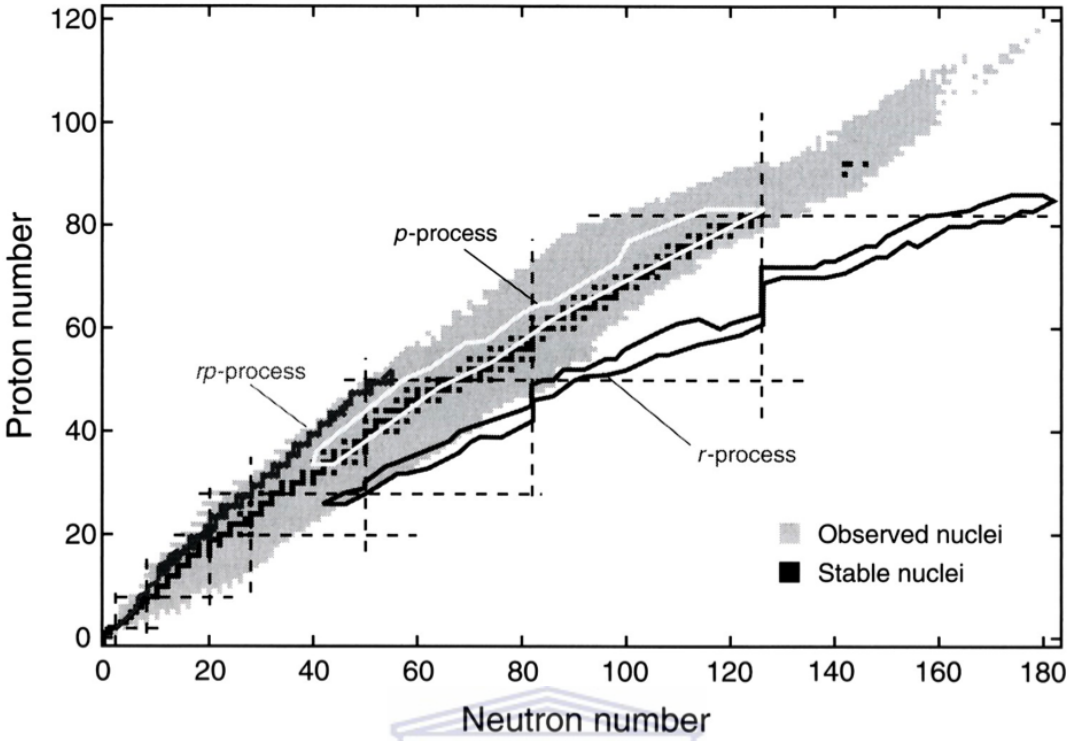

Figure 1.1. Illustration of the *rp*-, *p*- and *r*-process paths, across the nuclear chart [5].

order of magnitude [4]. As excitation energy increases in a nuclear system towards the particle separation energies, the NLD increases exponentially, creating the quasi-continuum. Nuclear properties in this excitation energy region are best characterized using statistical quantities, such as the γSF which is the ability of atomic nuclei to emit and absorb photons with energy E_γ. For example, NLDs and γSFs are important input parameters to Hauser-Feshbach calculations of cross sections which are widely used in both nuclear astrophysics [6] and reactor physics applications [7]. These cross sections in turn are input into large reaction network calculations to model the nucleosynthesis in astrophysical environments, and can be crucial to constrain the processes responsible for nucleosynthesis and the conditions of the astrophysical environments.

1.1 Physics motivation and objectives

The astrophysical origins of about 290 nuclides have been studied [8] but the nucleosynthesis of several nuclei, including ^{180}Ta, has remained a puzzle over the years. A unique feature of ^{180}Ta is that it is the rarest isotope in the solar system, which exists in a 9^- isomeric state at E_x = 77 keV ($t_{1/2,iso} > 10^{15}$ yr), with an isotopic abundance of about 0.012%. Over the years many processes, such as slow and rapid neutron capture reactions (s-process, r-process) in stars and

supernova explosions, photon- and neutrino-induced reactions in supernovae, have been proposed to be the production mechanism of ^{180}Ta. However, no consensus exists and it has been theoretically shown that ^{180}Ta could be exclusively explained with the (γ, n) p-process reaction [9] (see figure 1.2 for predicted p-process overabundances). The s-process alone can exclusively

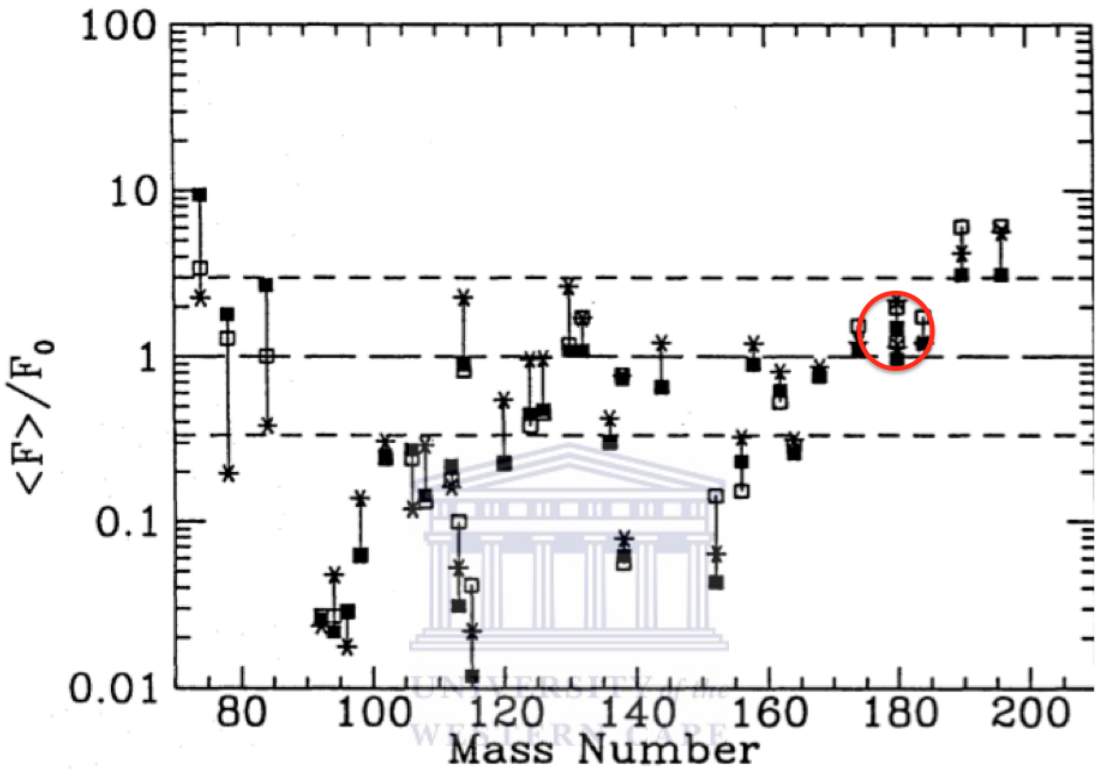

Figure 1.2. The p-abundance overproduction factor, $\langle F \rangle / F_0$, as function of mass number A, figure adapted from Ref. [9].

explain the production of ^{180}Ta, as well, mostly via branching in ^{179}Hf through the reactions ^{179}Hf$(\beta^-)^{179}$Ta(n,γ)^{180}Ta and/or ^{179}Hf(n,γ)$^{180^m}$Hf$(\beta^-)^{180}$Ta [10]. Furthermore, more exotic reactions such as neutrino (υ) processes, which include ^{180}Hf$(\upsilon_e, e)^{180}$Ta and ^{181}Ta$(\upsilon, \upsilon' n)^{180}$Ta, have been proposed to partly explain its synthesis [11, 12]. Since the astrophysical sites for the nucleosynthesis of ^{180}Ta remain unknown, a combination of the above processes may also be likely [11], see figure 1.3 for illustration. However, the significance of individual processes cannot be clearly determined, as a result of the uncertainties on the reaction rates for ^{180}Ta due to unavailability of experimental data, such as the NLD and γSF [14].

To our knowledge, these nuclear properties have never been measured below the neutron separation energy, S_n, for ^{180}Ta and below 6 MeV excitation energy for ^{181}Ta. The NLDs and γSFs are of utmost importance for the Hauser-Feshbach formalism [15] from which astrophysical re-

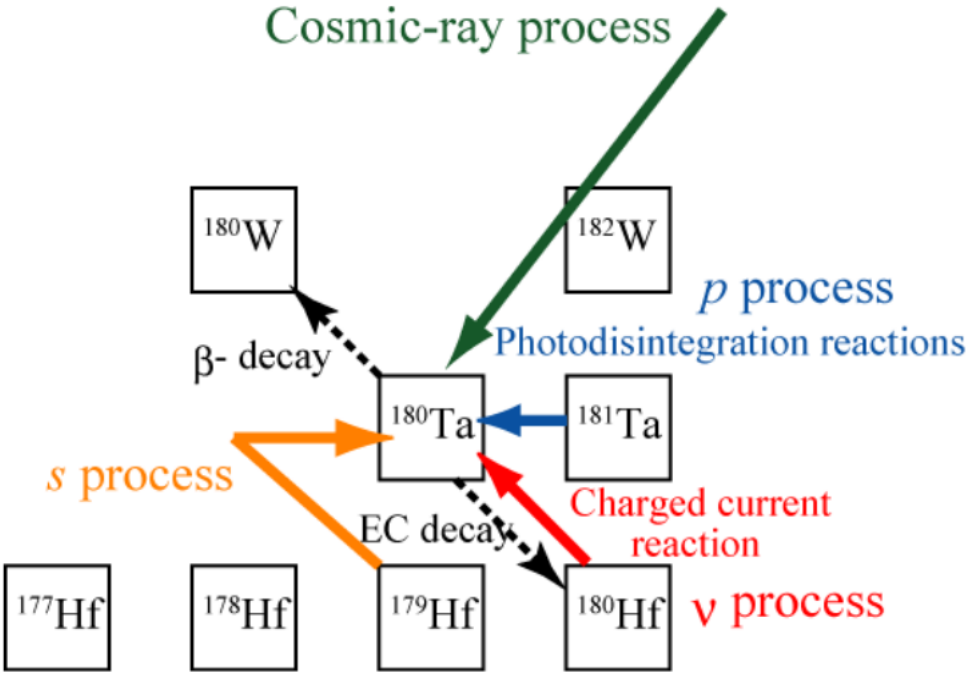

Figure 1.3. Illustration of s-, ν- and p-processes paths for synthesis of ^{180}Ta [13].

UNIVERSITY of the
WESTERN CAPE

action rates can be calculated. Clearly many different astrophysical processes can theoretically be used to explain nucleosynthesis of ^{180}Ta. Therefore nuclear properties (NLDs and γSFs) and their uncertainties must be accurately determined to place the nuclear physics aspects of the large network abundance calculations on a solid footing and to unambiguously probe the significance of various processes in the synthesis of ^{180}Ta.

The main objectives of this thesis are (i) to determine the NLDs and γSFs below the neutron separation energy threshold in ^{180,181}Ta isotopes using the ^{181}Ta(^{3}He,^{3}He'γ)^{181}Ta and ^{181}Ta(^{3}He,$\alpha\gamma$)^{180}Ta reactions with 34 MeV beam energy at the Oslo Cyclotron Laboratory, and (ii) to calculate the ^{179}Ta(n,γ) and ^{180}Ta(n,γ) cross sections from the experimental γSF and NLD calculated within the Constant Temperature (CT) model, that shows excellent agreement with experimental results, as input data in the TALYS reaction code. In addition, the calculated ^{179}Ta(n,γ) and ^{180}Ta(n,γ) cross sections will be used to determine the corresponding astrophysical Maxwellian-averaged (n,γ) cross sections at the s-process and p-process temperatures, which in turn can be utilized in astrophysical network calculations to investigate the galactic production mechanism of ^{180}Ta.

Chapter 2

Theory and experimental techniques

2.1 Nuclear level density and γ-ray strength function

The study of the average statistical nuclear properties such as the nuclear level density (NLD) and γ-ray strength function (γSF) provide the understanding of the underlying nuclear structure and consequently improve our knowledge of the astrophysical processes and reaction sites. The theory behind the NLD and γSF will be presented in the following sections, together with the models developed to interpret the behaviour of these two nuclear properties. In addition, calculations of the astrophysical reaction cross sections will be explained.

2.1.1 Nuclear level density

The atomic nucleus has discrete energy levels, usually at low excitation energies E_x, whose locations and properties (angular momentum, spin and parity) are governed by the rules of quantum mechanics. However, as the excitation energy increases, the number of levels increases exponentially. The spacings and widths of these levels increase tremendously and eventually overlap in energy, creating a quasi-continuum[1], as illustrated in figure 2.1. In the quasi-continuum region the nuclear levels are described using average statistical quantities such as the NLD and the γSF with the aid of statistical nuclear models. These models define the NLD as an exponential function of E_x, taking into account the average spin J and parity π distribution. However,

[1]The quasi-continuum region is located in between the discrete region where levels are easily resolved with present spectroscopic techniques, and the continuum region, where the levels overlap in energy and are currently impossible to resolve with present experimental methods.

there are various models that are widely used in the literature to define the level density of the atomic nuclei. Only models applicable to the thesis will be discussed below.

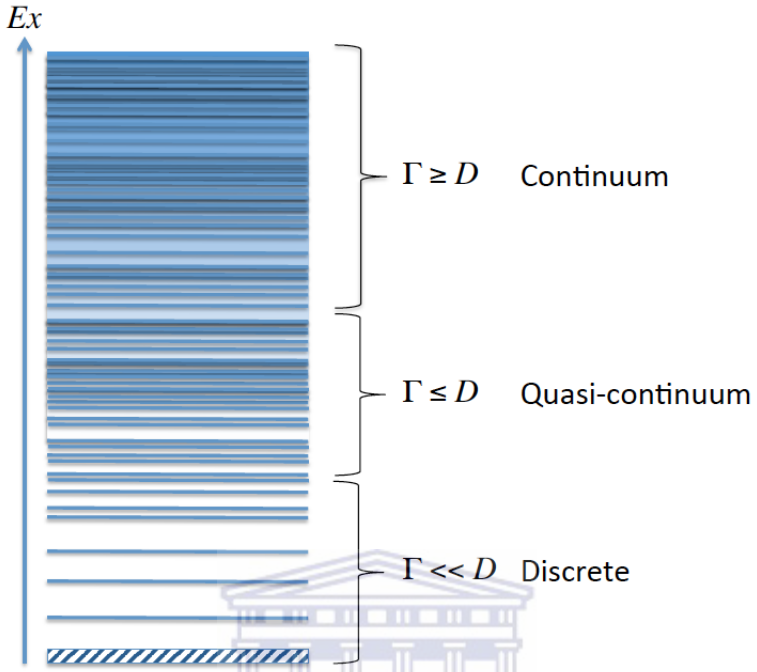

Figure 2.1. The density of the states as a function of excitation energy [16].

UNIVERSITY of the
WESTERN CAPE

2.1.1.1 Back-shifted Fermi gas model

The back-shifted fermi gas (BSFG) model, proposed by Gilbert and Cameron in 1965, for the NLD is based on the Fermi-gas approximation[2], see Ref. [17] for detailed discussion. The NLD of the BSFG model, which is integrated over all possible J^{π}, is expressed as:

$$\rho(U) = \frac{\sqrt{\pi}}{12} \frac{e^{(2\sqrt{aU})}}{a^{\frac{1}{4}} U^{\frac{5}{4}}} \frac{1}{\sqrt{2\pi}\sigma} \tag{2.1}$$

where $U{=}E_x - E_1$ and σ are back-shifted excitation energy and spin cut-off parameter. The parameters a and E_1 are the level density parameter and the Fermi-gas energy shift parameter. The spin cuofft-off parameter σ is given by

$$\sigma^2 = 0.0888 A^{\frac{2}{3}} \sqrt{a(S_n - E_1)} \tag{2.2}$$

[2]The Fermi-gas model assumes that a nucleus is made up of non-interacting Fermi-particles moving freely in single particle states which are equally spaced.

where a and E_1 are treated as free parameters that are adjusted to fit experimental data and can be obtained from Ref. [18], and A denotes the nuclear mass. Furthermore, the level density parameter a can be calculated from total shell correction as follows for spherical nuclides:

$$\frac{a}{A} = 0.00917S + 0.142 \tag{2.3}$$

and for deformed nuclides

$$\frac{a}{A} = 0.00917S + 0.120 \tag{2.4}$$

where S is the total shell corrections and can be obtained from Ref. [17]. The total shell correction S accounts for the shell effects from odd-even mass systems for the semi-empirical atomic mass formula. Most recent spin cut-off parameters σ^2 proposed by von Egidy and Bucurescu [18], as a function of E_x are given as

$$\sigma^2 = 0.391A^{0.675}(E_x - 0.5Pa')^{0.312} \tag{2.5}$$

where Pa' is the deuteron pairing energy.

UNIVERSITY of the
WESTERN CAPE

2.1.1.2 Constant temperature model

For $2\Delta_0 < E_x < 10$ MeV, where Δ_0 is the pair gap parameter [19], the NLD can accurately be obtained from the widely used constant-temperature (CT) model [17]. The model is based on the constant-temperature approximation of the level density of all J^π in the $E_x < 10$ MeV region, and is given by

$$\rho(E_x) = \frac{1}{T} e^{\left(\frac{E_x - E_0}{T}\right)} \tag{2.6}$$

where E_0 and T are the energy-shift and constant nuclear temperature parameters, respectively. These free parameters, E_0 and T, can be calculated from the total shell corrections according to Ref. [18]:

$$E_0 = -1.004 + 0.5Pa' \tag{2.7}$$

and

$$T = \frac{1}{A^{\frac{2}{3}}(0.0597 + 0.00198S')} \tag{2.8}$$

where

$$S' = S + 0.5Pa'. \tag{2.9}$$

The deuteron pairing energy Pa' and shell correction, S, are obtained from Ref [18].

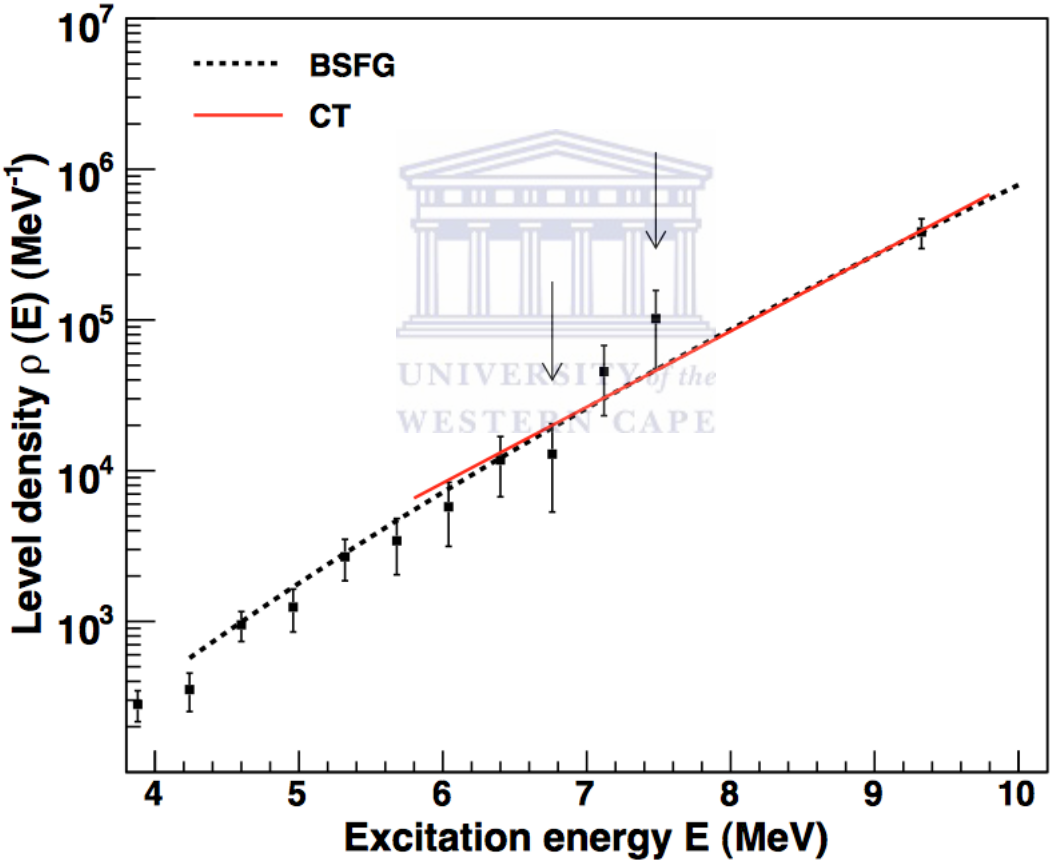

Figure 2.2. Comparison of the BSFG model (dashed line) and the CT model (solid line) as level density interpolation methods in ^{118}Sn [20].

Comparison of the BSFG model (dashed line) and the CT model (solid line) as interpolation methods for the NLD of ^{118}Sn, are shown in figure 2.2 . The arrows indicate the region where the level density is normalized. The small difference in the region of interpolation is negligible for the normalization procedure.

2.1.2 The γ-ray strength function

The γSF, $f_{XL}(E_\gamma)$, is a measure of the average electromagnetic property of excited nuclei. The $f_{XL}(E_\gamma)$ is described as the average transition strength for a γ ray decay with γ-ray energy E_γ, electromagnetic character X and multipolarity L, decaying from an initial state E_i to a final state E_f [21]. The $f_{XL}(E_\gamma)$ can be discriminated as the "downward" γSF, $\overleftarrow{f}^{J}_{ifXL}(E_\gamma)$, and "upward" γSF, $\overrightarrow{f}^{J}_{ifXL}(E_\gamma)$, see figure 2.3, where [22]:

(i) The "downward" γSF, $\overleftarrow{f}^{J}_{ifXL}(E_\gamma)$, is related to the average radiative width of γ-ray decay.

(ii) The "upward" γSF , $\overrightarrow{f}^{J}_{ifXL}(E_\gamma)$, is related to photoabsorption cross-section.

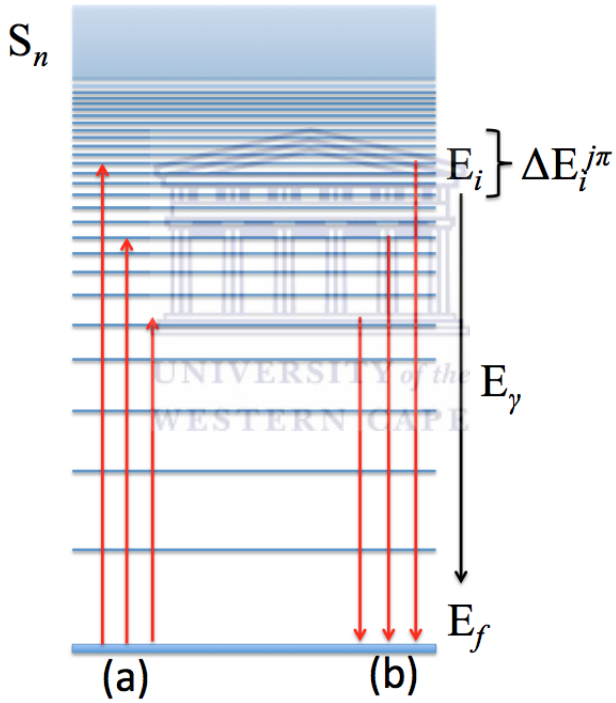

Figure 2.3. Average transition strength (a) for photoabsorption to higher excited states E_i, and (b) for γ-ray decay from a group of states of the same J^π to a range of lower states E_f.

Only the "downward" γSF, $\overleftarrow{f}^{J}_{ifXL}(E_\gamma)$, which is of interest in this thesis, will be discussed. Hence, the notation $f_{XL}(E_\gamma)$ will be used instead of $\overleftarrow{f}^{J}_{ifXL}(E_\gamma)$, to denote the γ-ray decay strength function. According to Ref. [21], the γSF for a transition between an excited state E_i, with spin and parity J^π, and a lower energy state E_f, is given by

$$f_{XL}(E_\gamma) = \frac{\rho(E_f)\langle\bar{\Gamma}_{\gamma XL}\rangle}{E_\gamma^{(2\ell+1)}} \tag{2.10}$$

where $\langle \bar{\Gamma}_{\gamma XL} \rangle$ is the average radiative width, which is usually determined from the s- or p-wave resonances obtained from neutron capture experiments and $\rho(E_f)$ is the level density of the final states E_f.

However, there are different theoretical models that are widely used to interpret the γSF for different modes of excitations and multipole types. A summary of these theoretical models, referred to as resonance models will be given below, together with their respective resonances that are observed as part of the total γSF and are relevant to this work.

2.1.2.1 Resonances of the γ-ray strength function

The simple single-particle model of Blatt and Weisskopf [23], which results in energy-independent γSFs, does not account for collective modes of nuclear excitation. It has been found that the total γSF, for all nuclei studied [22, 24], in the excitation energy region $\approx$ 8 - 20 MeV displays a resonance like structure, called the giant electric dipole resonance (GEDR), see figure 2.4. The GEDR arises from the isovector, $\Delta T = 1$, collective excitation mode of the nucleus and is due to oscillations of protons against neutrons in the nucleus, as shown in figure 2.5. It is located at high excitation energy in the range of $\approx$ 14 - 22 MeV with typical width of $\approx$ 2 - 7 MeV, depending on the mass of the nucleus [26].

UNIVERSITY of the
WESTERN CAPE

Other giant dipole resonances have been observed as well, such as the magnetic spin-flip resonance, which is also known as the giant magnetic dipole resonance (GMDR) which results from spin flip collective excitations [27]. It is built on the isoscalar mode of excitation, where nucleons with spin $\uparrow$ oscillate against those with spin $\downarrow$. In addition, GMDR can originate from the isovector excitation mode, in which protons with spin $\uparrow$ oscillate against neutrons with spin $\downarrow$ and vice versa. Furthermore, there has been experimental evidence for other types of nuclear excitation modes, such as the E1 pygmy resonance and the scissors resonance. The E1 pygmy resonance is energetically located below the GEDR [28] and has been observed only in nuclei with excess number of neutrons. It is believed to be caused by collective vibrations of excess neutrons against an isospin ($T = 0$) symmetric proton-neutron core (see figure 2.6 left panel). Moreover, experimental evidence for this low energy dipole resonance is reviewed in Ref. [29]. Additionally, another low resonance, namely the scissors resonance which is located at fairly low energies $\approx$ 3 MeV is believed to be present only in deformed nuclei [30]. This type of resonance is due to M1 collective excitations, where neutron and proton clouds oscillate against each other, clipping like a pair of scissors. See figure 2.6 right panel, for illustration.

An additional feature has been observed on the γSF of light- to medium-mass nuclei such as

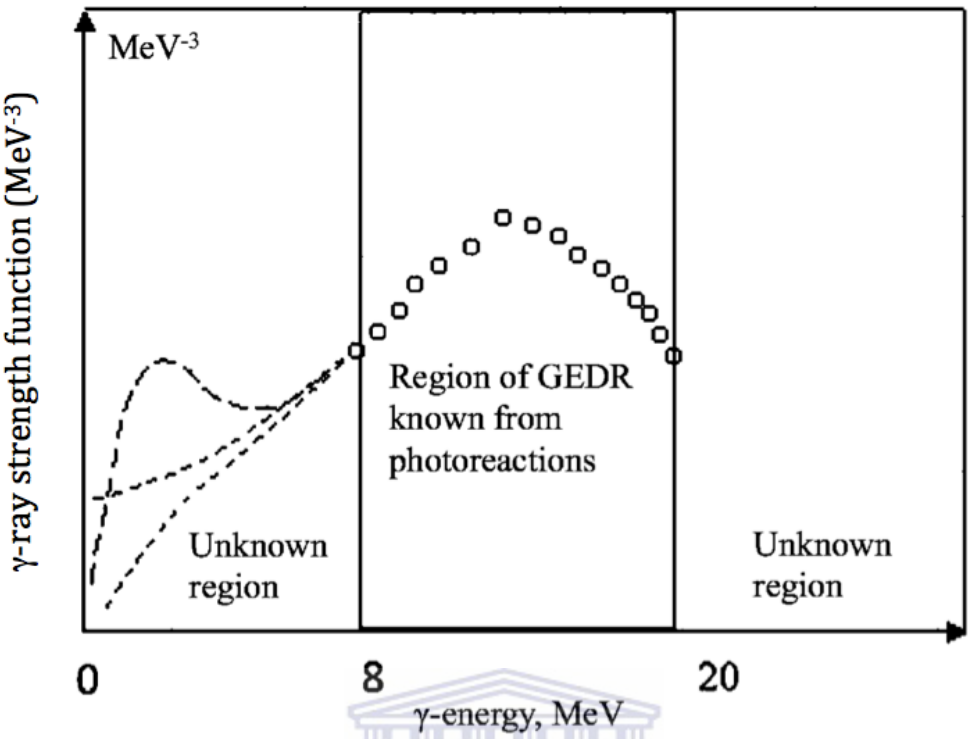

Figure 2.4. GEDR observed in the region ≈ 8 - 20 MeV typical for all nuclei studied, figure adapted from Ref. [25].

UNIVERSITY of the
WESTERN CAPE

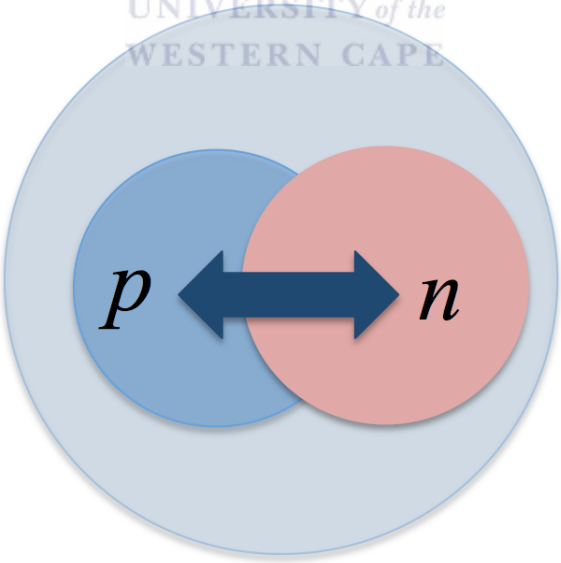

Figure 2.5. The GEDR collective mode of nuclear excitation.

(^{44,45}Sc [31], ^{50,51}V [32], ^{44,45,46}Ti [33, 34, 35], ^{56,57}Fe [36, 37], $^{93-98}$Mo [38], and ^{105,106}Cd [39] isotopes), using the Oslo Method and independently confirmed using a different measurement and method in ^{95}Mo [40]. The existence of this feature has been recently shown in the heavy

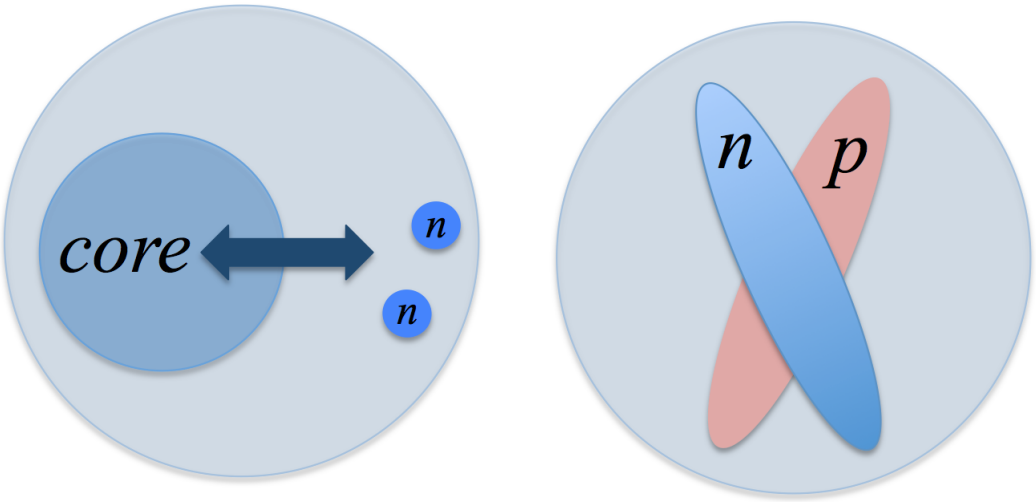

Figure 2.6. Pygmy dipole collective mode of nuclear excitation (left), and the M1 scissors mode (right).

mass nucleus ^{138}La [4]. This feature has been observed at a typical energy range of $E_\gamma \leq 3$ MeV (See example in figure 2.7), and is termed the low-energy enhancement also known as the up-bend. However, the physical origin of this enhancement remains unknown and is currently a topic of great interest in both theoretical and experimental nuclear physics. This low-energy enhancement has been predicted to be of $M1$ strength [41, 42], in contrast to Ref. [43] which predicts that the up-bend results from $E1$ transitions. In spite of the differences between approaches, they all suggest that the enhancement is of dipole type. Recently, it has been experimentally verified that it is indeed primarily dipole in nature [37].

UNIVERSITY of the WESTERN CAPE

2.1.2.2 Models for γ-ray strength function

With the assumption that the Brink hypothesis[3] [44] holds, the GEDR can be described using the Standard Lorentzian function (SLO) given as [45]

$$f_{E1}^{SLO} = \frac{1}{3\pi^2\hbar^2c^2}\frac{\sigma_0 E_\gamma \Gamma_0^2}{(E_\gamma^2 - E_0^2)^2 + E_\gamma^2\Gamma_0^2}[\text{MeV}^{-3}], \tag{2.11}$$

where σ_0 (in mb), Γ_0^2 (in MeV) and E_0^2 (in MeV) are the peak cross-section, GEDR width and centroid energy of the resonance, respectively. The constant $1/(3\pi^2\hbar^2c^2) = 8.67410^{-8}\text{mb}^{-1}\text{MeV}^{-2}$. Although SLO accurately describes the GEDR close to the resonance centroid for medium-

[3]The Brink Hypothesis states that the collective modes of nuclear excitation built on excited states have the same properties as those built on the ground state.

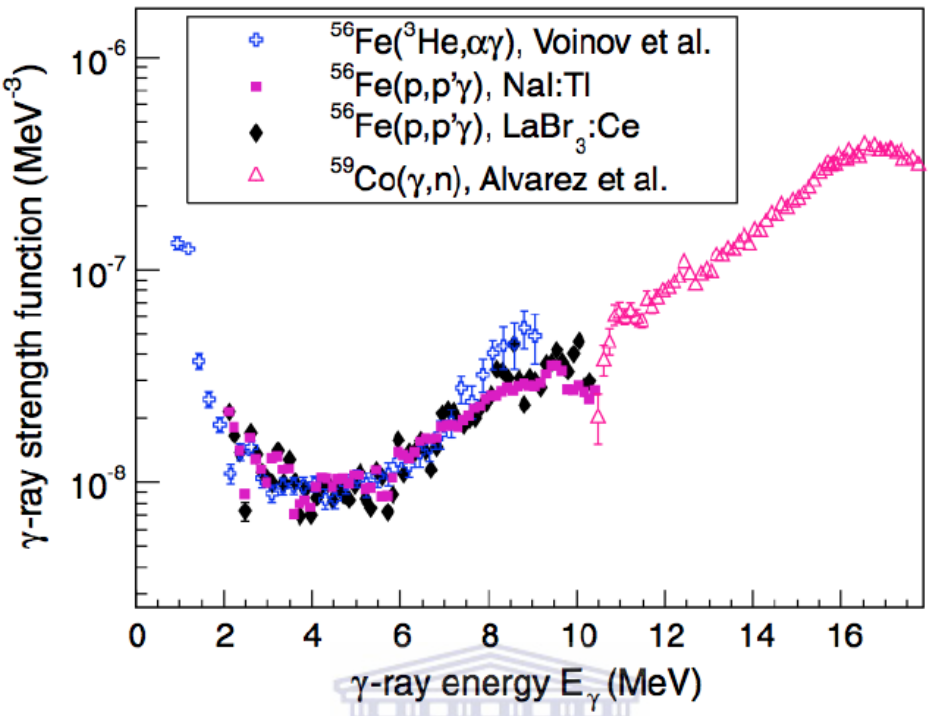

Figure 2.7. The γSFs of ^{55,56}Fe from ^{56}Fe(^{3}He, $\alpha\gamma$) and ^{56}Fe(p, $p\gamma$) experiments, compared with ^{59}Co(γ, n) GEDR data [37].

UNIVERSITY of the WESTERN CAPE

and heavy-mass nuclei, it often underestimates the γSF at and below S_n. The Generalized Lorentzian function (GLO), proposed by J. Kopecky and R. E. Chrien [46], which has energy- and temperature-dependent width included in the description of the GEDR, is given by

$$f_{E1}^{GLO} = \frac{1}{3\pi^2\hbar^2c^2}\sigma_0\Gamma_0\left[\frac{E_\gamma\Gamma(E_\gamma,T_f)}{(E_\gamma^2-E_0^2)^2+E_\gamma^2\Gamma_0^2}+0.7\frac{\Gamma(E_\gamma=0,T_f)}{E_0^3}\right][\mathrm{MeV}^{-3}], \tag{2.12}$$

where the energy- and temperature-dependent width of the GEDR is given by [45]:

$$\Gamma(E_\gamma,T_f) = \frac{\Gamma_0(E_\gamma^2+4\pi^2T_f^2)}{E_0^2}, \tag{2.13}$$

and the nuclear temperature T_f of the final states on which the GEDR is built, is defined by

$$T_f = \sqrt{\left(\frac{S_n-E_\gamma}{a}\right)}. \tag{2.14}$$

The parameters S_n and a are the neutron separation energy and the BSFG level density parameter, respectively. The GLO model reproduces the low-energy region well and gives a non-zero strength for $E_\gamma \to 0$. Furthermore, the GLO model gives a reasonable agreement with observed $f(E_\gamma)$, at least for spherical nuclei but underestimates the observed $f(E_\gamma)$ for highly deformed nuclei in the mass range $A \sim 150$ - 175 by up to a factor of 4 [47]. For that reason, an Enhanced Generalized Lorentzian (EGLO) function has been proposed to account for the GEDR of deformed nuclei in the mass region $A \sim 150$ - 175. The temperature dependent width of the EGLO has been generalized, as defined below [47]:

$$\Gamma(E_\gamma, T_f) = k_0 + (1 - k_0)\left(\frac{E_\gamma - \epsilon_0}{E_0 - \epsilon_0}\right)\frac{\Gamma_0}{E_0^2}(E_\gamma^2 + 4\pi^2 T_f^2), \tag{2.15}$$

where the enhancement factor k_0 depends on the mass of the target nucleus. Both constants $k_0 > 1$ and ϵ_0 can be adjusted to reproduce the average resonance capture data [22]. To describe the magnetic spin-flip giant resonance, the SLO f_{M1}^{SLO} (see equation (2.11)) with a temperature and energy independent width, is recommended to be used in Ref. [22] for such M1 strengths. The M1 resonance parameters are deduced from systematics, where $E_0 = 41A^{-\frac{1}{3}}$, $\Gamma_0 = 4$ MeV, and the peak cross section σ_0 is adjusted using the relationship below

$$\frac{f_{E1}}{f_{M1}} = 0.0588A^{0.878}. \tag{2.16}$$

UNIVERSITY of the WESTERN CAPE

2.1.3 Impact of the low-energy enhancement on astrophysical reaction rates

The low-energy enhancement in the γSF has been shown to have significant impact on the astrophysical reaction rates, more specifically for the production of neutron-rich nuclides. This has been indicated by Maxwellian-averaged neutron capture, (n, γ), rates $\langle \sigma \mathrm{v} \rangle$, calculated at the r-process temperature $T = 10^9$ K, for the entire isotopic chains of Mo, Fe and Cd up to the neutron drip line [48]. As the number of neutrons increases towards the neutron dripline, the impact of the low-energy enhancement on the r-process reaction rates can amount up to 2 orders of magnitude (see figures 2.8 and 2.9).

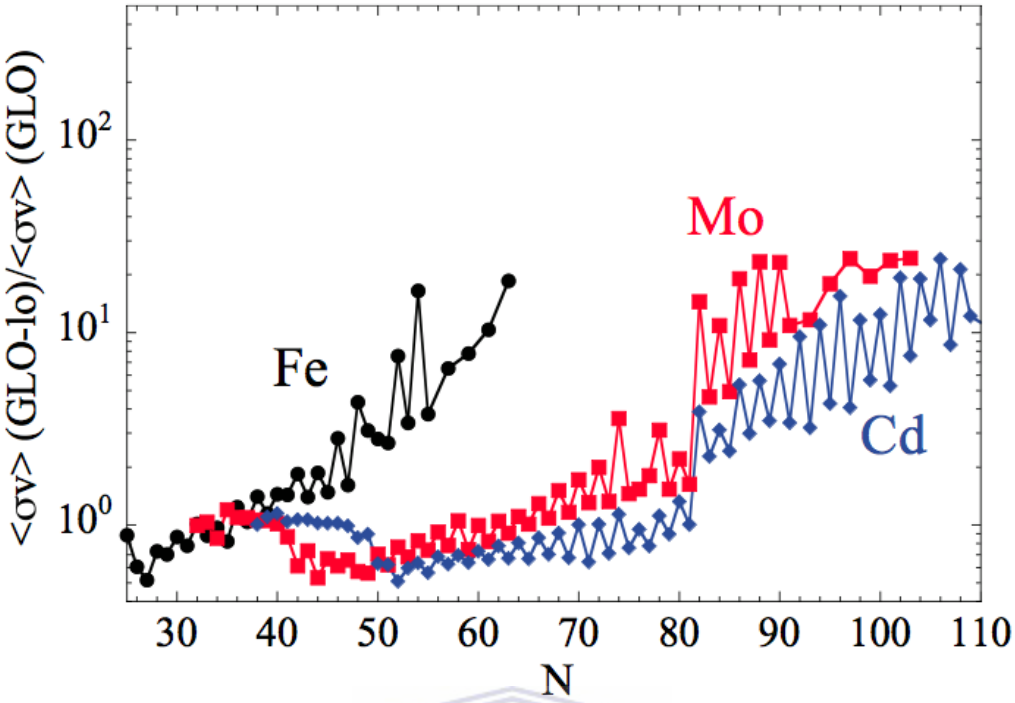

Figure 2.8. Maxwellian-averaged reaction rates when the low-energy enhancement is excluded [48].

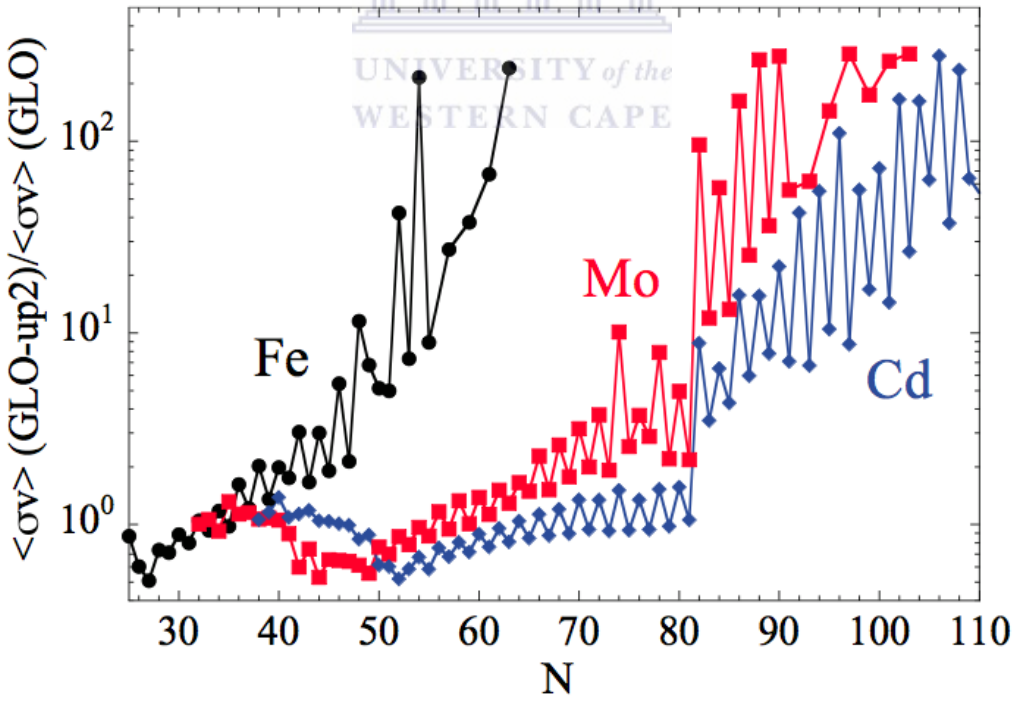

Figure 2.9. Maxwellian-averaged reaction rates with the low-energy enhancement included [48].

2.1.4 Impact of the E1 pygmy resonance on nucleosynthesis

The impact of the E1 pygmy resonance (PR) on r-process nucleosynthesis has been evaluated [49], using the non-equilibrium canonical model [50] in which a full reaction network is solved for a given set of parameters. The set of parameters include the neutron density in an astrophysical site, N_n, its temperature, T, and the period of the neutron irradiation, τ_{irr}. The calculated r-abundance with and without the E1 pygmy resonance at $T = 10^9$ K, $N_n = 10^{20}$ cm^{-3} and $\tau_{irr} = 2.4$ s, are shown in figure 2.10. The r-abundance calculations are performed using 3 different estimates of the neutron capture rates, this include (i) the standard Hauser-Feshbach (HF) predictions in which the γSF is described by the GEDR, (ii) when the PR strength is added to the GEDR, and (iii) the final compound nucleus (CN) contribution corresponding to the GEDR+PR predictions damped for resonance-deficient nuclei and to which the radiative direct capture (DC) of neutrons contribution is added [49]. Most nuclei in the mass region $A \approx$ 90 - 110 are produced when only the giant electric dipole resonance (open squares) is taken into account, as shown in figure 2.10. When the E1 pygmy resonance is included in the calculations, the predicted r-abundance reduces by up to 2 orders of magnitude in the same mass region, and is increased by up to the same order of magnitude in the $A \approx 130$ mass region (open triangles down). Clearly the E1 pygmy resonance has a significant impact on r-process nucleosynthesis.

UNIVERSITY of the
WESTERN CAPE

2.1.5 Astrophysical reaction rates and nucleosynthesis

The astrophysical reaction (such as (n, γ)) rates for medium or heavy nuclei, of particular relevance to astrophysics, are calculated using the HF statistical emission model which is implemented in the TALYS reaction code [15, 51]. TALYS is a user-friendly reaction code which is used to simulate nuclear reactions that include photons, neutrons, protons, deuterons, tritons, ^{3}He, and α-particles as both projectiles and ejectiles. It is optimized for incident projectiles, with an energy range of 1 keV $\leqslant E_{proj} \leqslant$ 200 MeV, on target nuclei with mass range of $12 \leqslant A_{tar} \leqslant 339$. The HF model is based on the assumption (Bohr hypothesis) that the capture process in the stellar interior occurs by means of production of a compound nuclear system that has reached thermodynamic equilibrium state with different J^π. The formation of the CN can take place only if the CN level density, at the E_x corresponding to the projectile incident energy, is sufficiently high. Therefore the corresponding reaction capture cross-section, σ^{E_x}, are estimated in TALYS from the compound nucleus formula as follows

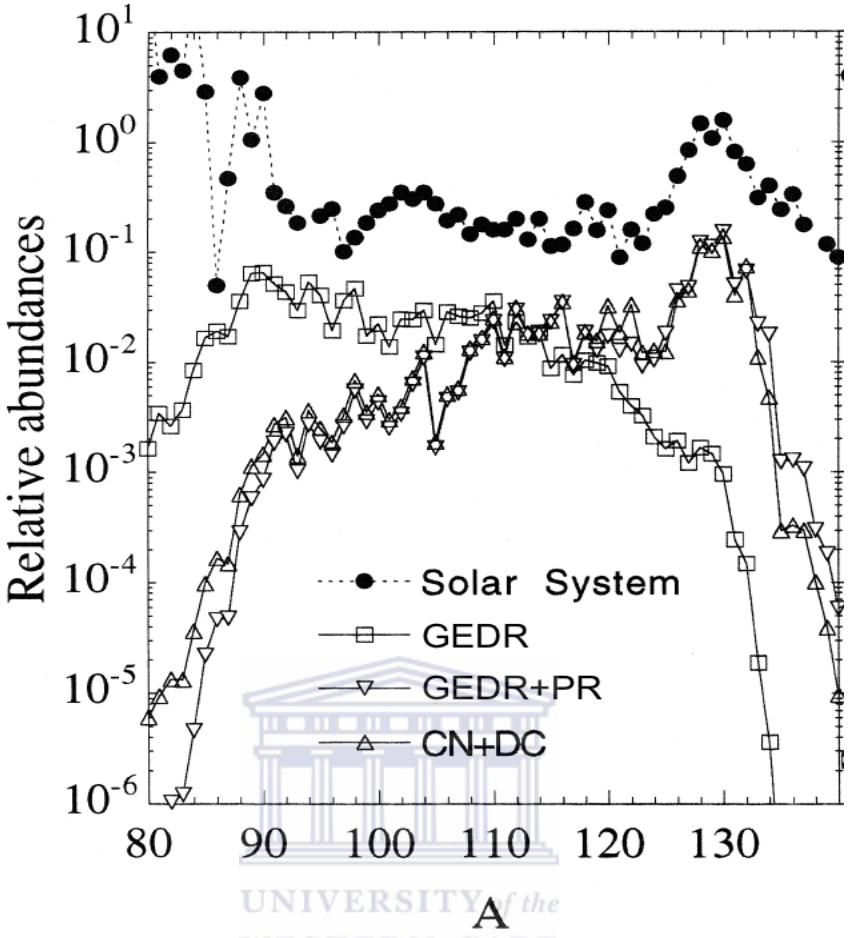

UNIVERSITY of the
WESTERN CAPE

Figure 2.10. The r-abundance distributions with (open triangles down) and without (open squares) the contribution of a $E1$ pygmy resonance. The top curve (black circles) is the solar abundance distribution, figure adapted from Ref. [49].

$$\sigma^{E_x} = D^{comp}\pi\lambda^2 \sum_{J,\Pi} \frac{2J+1}{(2s+1)(2I^{\mu}+1)} \times \sum_{j,l,j',l'} \delta(\alpha)\delta(\alpha') \times \frac{\langle T^J_{\alpha l j}(E_a)\rangle \langle T^J_{\alpha' l' j'}(E_{a'})\rangle}{\sum_{\alpha'',l'',j''} \delta_{\pi}(\alpha'')\langle T^J_{\alpha'' l'' j''}(E_{a''})\rangle} W^J_{\alpha l j \alpha' l' j'} \tag{2.17}$$

where j, l, s, π, E_a represent the total angular and orbital momentum, spin, parity and energy of the projectile, respectively. The same symbols but with a prime correspond to the ejectile. All the parameters with double prime correspond to the decay of residual nucleus to lower energy states. In Eq. (2.17), λ is the relative motion wavelength, T the transmission coefficient, W the width fluctuation correction factor and D^{comp} the depletion factor as calculated according to Ref. [51]. The function $\delta(\alpha)$ is unity, if $(-1)^l\pi\Pi^{\mu}$=Π, and 0 otherwise. The quantities J

and Π represent the spin and parity of the compound system, while I^{μ} and Π^{μ} correspond to the spin and parity of the target nucleus.

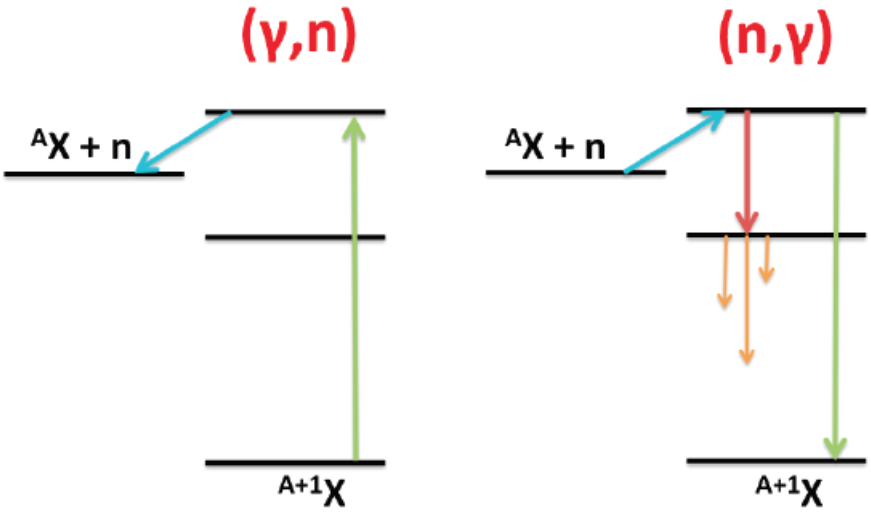

Figure 2.11. An illustration of the (γ, n) (left) and (n, γ) (right) reactions [53].

UNIVERSITY of the WESTERN CAPE

In Eq. (2.17), the reaction capture cross-section, σ^{E_x}, is defined as a function of the γ-ray transmission coefficients. The transmission coefficient is calculated from the following parameters which are key ingredients for the HF approach: the ground- and excited-state properties (masses, deformation, matter densities, excited state E_x and J^{π}), NLD, γSF, optical model potentials and fission properties. Furthermore, the thermodynamic equilibrium holds locally to a good approximation inside stellar interiors. As a result, the respective energies of target nuclei and projectiles, as well as their relative energies, obey a Maxwell-Boltzmann distribution of energies corresponding to a temperature, T, at that location. Hence, the astrophysical reaction rates are obtained by integrating the cross section, σ^{E_x}, over the Maxwell-Boltzmann distribution at a given T, according to Ref. [51]. Using the principle of detailed balance, the (n, γ) cross-sections will be equal to the (γ, n) cross-sections [54], see figure 2.11 for illustration. The rates of all possible reactions such as (n, γ), (p, γ), (α, γ) and their respective photodisintegration processes, can be obtained from the TALYS reaction code using the HF approach as discussed above.

2.2 The Oslo method

The Oslo method is an analytical procedure, which allows for the simultaneous extraction of the NLD and the γ-ray transmission coefficient, up to the neutron (proton) separation energy, from particle-γ coincidence measurements through several iterative methods. The main steps of the Oslo method include: 1) unfolding the continuum γ-ray spectrum based on the known detector response functions, 2) extraction of primary γ rays from the unfolded γ-ray spectra using the iterative procedure called the first generation method, 3) extracting simultaneously the NLD and the γ-ray transmission coefficient from the primary γ-ray matrix, 4) and finally the normalization of the NLD and the γ-ray transmission coefficient using the s- or p-wave neutron resonance data. An outline of these main steps is given below and a detailed discussion of the method is given in Refs. [55, 56].

2.2.1 Unfolding continuum γ-ray spectra

UNIVERSITY of the WESTERN CAPE

The continuum γ-ray spectra display a broad energy distribution without outstanding individual full energy γ-ray peaks. The response functions of the γ-ray detector depend on the various processes photons interact with matter. These processes include the photo-electric effect, Compton scattering and pair production, and each process contributes to the measured γ-ray spectrum with different energy dependences. From the response functions of the NaI(Tl) detector (referred to as CACTUS array, see section 3.2) for all incident γ-ray energies, a full energy γ-ray spectrum can be constructed through the folding iterative procedure called the Compton subtraction method, explained in Ref. [57]. This is obtained by interpolating between the measured response functions of well known γ-ray lines, recorded from radioactive sources of γ rays and from in-beam measurements, to determine the response functions, $R(E, E_\gamma)$, of all possible γ-ray energies E_γ. $R(E, E_\gamma)$ denotes the response of the CACTUS array, where E is the actual amount of energy deposited in the detector by an incident photon of energy E_γ. Altogether, ten (10) $R(E, E_\gamma)$ response functions have been measured for monoenergetic γ rays in the range of 122 - 15110 keV, see Ref. [57]. To obtain a new response function for an intermediate full energy γ-ray peaks, the interpolation between these peak structures can easily be performed by adding a Gaussian distribution at the interpolated peak position with proper intensity and energy resolution. With the $R(E, E_\gamma)$ eventually determined for all known γ-ray energies, the full energy, the single- and double escape peaks, and the annihilation peaks have been removed from this spectra, due to reasons mentioned in Ref. [57]. However, the interpolation of the Compton background, which is now the remaining part of the observed $R(E, E_\gamma)$

(response spectrum), is performed between channels having the same γ-ray scattering angle θ, (see illustration in figure 2.12).

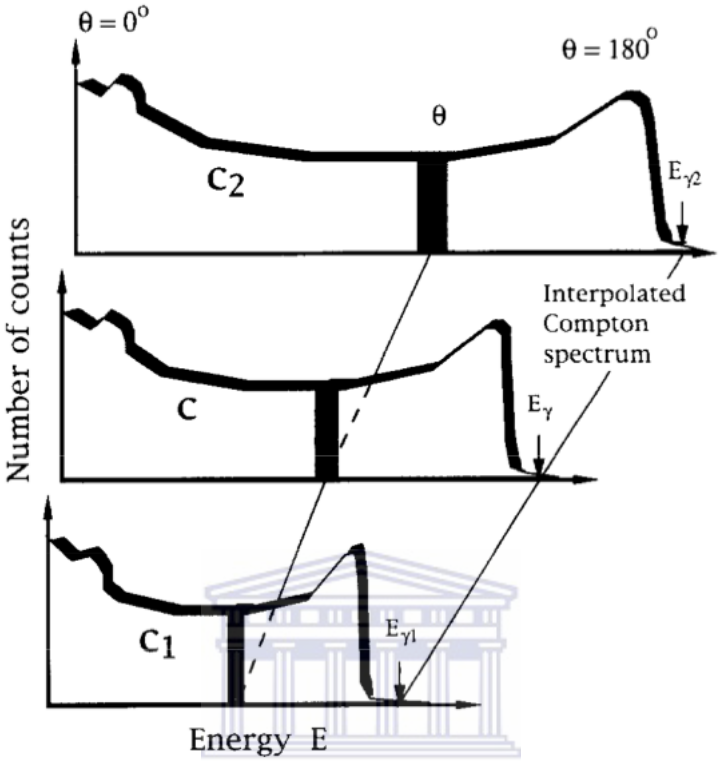

UNIVERSITY of the
WESTERN CAPE

Figure 2.12. Illustration of the interpolation of the Compton part from measured response functions c_1 and c_2 [57].

The matrix element, R_{ij}, of the response matrix $\boldsymbol{R}$ is described as the response in energy channel i when the detector is hit by γ rays with an energy, E_γ, corresponding to a decay to energy channel j. The response function is normalized so that $\sum_i R_{i,j}$=1, for each incident γ-ray channel j. The unfolded γ-ray spectrum, u, forms the basis of the folding iterative procedure which is expressed as [57]

$$f = \boldsymbol{R}u, \tag{2.18}$$

where f and $\boldsymbol{R}$ represent the folded γ-ray spectrum and response matrix of the CACTUS array, respectively. The folding iterative procedure is then performed as follows:

1. As the first trial function for the unfolded γ-ray spectrum u_0, the observed (raw) γ-ray spectrum r is used, setting

$$u_0 = r. \tag{2.19}$$

2. The first folded spectrum is now calculated as

$$f_0 = \boldsymbol{R}u_0. \tag{2.20}$$

3. The next trial function is obtained by adding the difference spectrum $r - f_0$ to the original trial function u_0, as

$$u_1 = u_0 + (r - f_0). \tag{2.21}$$

4. The new trial function u_1 is folded again to obtain the next folded spectrum f_1, which is used again to obtain the next trial function u_2, as

$$u_2 = u_1 + (r - f_1). \tag{2.22}$$

UNIVERSITY of the WESTERN CAPE

5. Steps 2-4 are repeated until $f_n \approx r$ where n is the iteration index (typically $n \approx 10$ - 30).

Once the unfolded γ-ray spectrum u_n is obtained from the folding iteration method, the Compton subtraction method [57] can be used to produce a much less fluctuating unfolded γ-ray spectrum u.

2.2.2 The Compton subtraction method

The final unfolded γ-ray spectrum $u_n = u$ from the folding iteration method reveals strong oscillations and fine structures, which artificially yield a better resolution of u as compared to the experimental resolution. The Compton subtraction method [57] is then applied to the unfolded γ-ray spectrum u, now denoted u_0, to produce a much less fluctuating unfolded γ-ray spectrum. This method starts out by defining a new spectrum, representing the observed spectrum, u_0, minus the Compton contributions, given by

$$v(i) = u_f(i) + w(i) \tag{2.23}$$

where $u_f(i) = p_f(i)u_0(i)$ is the full-energy contribution and $w(i) = u_s + u_d + u_a$ is the contribution from structures as a result of single escape u_s, double escape u_d, and annihilation processes u_a. Contributions from the second term $w(i)$ are calculated as

$$u_s(i - i_{511}) = p_s(i)u(i), \tag{2.24}$$

$$u_d(i - i_{1022}) = p_d(i)u(i) \tag{2.25}$$

and

$$u_a(i_{511}) = \sum_i p_a(i)u(i) \tag{2.26}$$

where i_{511} and i_{1022} represent channels having γ-ray energies 511 and 1022 keV, respectively. The probabilities $p_f(i)$, $p_s(i)$, $p_d(i)$, and $p_a(i)$, for an event in channel i categorized to be a photo peak, single escape, double escape or annihilation process are taken from Table 1 in Ref. [57]. The u_a spectrum, initially with all its counts in channel i_{511}, has to be smoothed out with the measured experimental resolution (FWHM) of 1.0 FWHM to obtain the energy resolution of the observed spectrum. The u_f, u_s and u_d spectra have their energy resolutions determined by the resolution of the observed spectrum (1.0 FWHM) and the response matrix (0.5 FWHM) yielding $\sqrt{1.0^2 - 0.5^2}$ FWHM = 0.87 FWHM. Furthermore, these spectra are smoothed with an additional 0.5 FWHM in order to obtain a spectrum with the observed experimental resolution of 1.0 FWHM: $\sqrt{0.87^2 + 0.5^2}$ FWHM $\approx$ 1.0 FWHM. Thus, a Compton background spectrum, $c(i)$, can then be extracted by subtracting contributions of u_f, u_s, u_d and u_a from the observed spectrum $r(i)$, as follows

UNIVERSITY of the WESTERN CAPE

$$c(i) = r(i) - v(i) \tag{2.27}$$

where

$$v(i) = u_f + u_s + u_d + u_a. \tag{2.28}$$

The smoothed part of the Compton background spectrum, $c_{smoothed}(i)$, in addition to structures, $w(i)$, are now subtracted from the observed spectrum, $r(i)$, to obtain the unfolded γ-ray spectrum, $u_{unf}(i)$, as follows

$$u_{unf}(i) = r(i) - c_{smoothed}(i) - w(i). \tag{2.29}$$

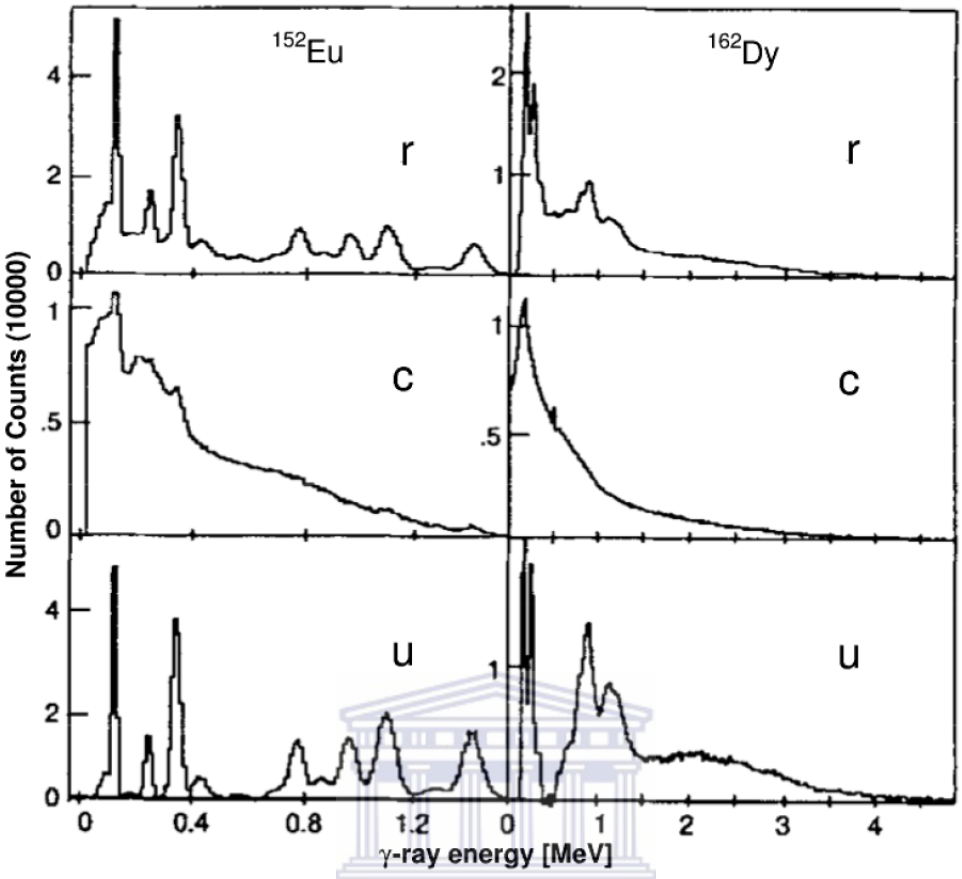

UNIVERSITY of the WESTERN CAPE

Figure 2.13. The raw γ-ray spectra (r), Compton background spectra (c), and unfolded γ-ray spectra (u) of ^{152}Eu and ^{162}Dy [57].

As the final step, the true γ-ray energy distribution $U_{true}(i)$ is calculated by correcting $u(i)$ for the full energy probability $p_f(i)$ and the γ-ray efficiency $\epsilon_{tot}(i)$,

$$U_{true}(i) = \frac{u_{unf}(i)}{p_f(i)\epsilon_{tot}(i)} \tag{2.30}$$

where the γ-ray total detection efficiency ϵ_{tot} is taken from Table 1 in Ref. [57]. From the true γ-ray energy distribution spectrum $U_{true}(i)$, a matrix of excitation energy, E_x, vs unfolded primary γ-rays can be constructed. An example of the differences in raw γ-ray spectra, r, Compton background spectra, c, and the corresponding unfolded γ-ray spectra, $u_{unf} = r - c_{smoothed} - w$ discussed above can be clearly seen in figure 2.13.

2.2.3 The first generation γ rays

The first-generation (primary) γ rays are emitted from highly excited states and represent the first decay step of all possible decay routes. Generally, γ rays from highly excited states involve an avalanche of transitions. Therefore, an iterative procedure referred to as the *first-generation method* is used to extract the primary γ-rays, from the γ rays that emerge from the later steps in the decay cascades at each excitation-energy bin of the continuum γ-ray spectra. This method is based on the assumption that states populated by γ-ray decays from higher-lying states (as a consequence of the first γ-ray transitions) have the same decay properties as the states populated directly in the particle nuclear reaction at that specific excitation energy. Details of the method are found in Ref. [58], and only its main features are discussed below.

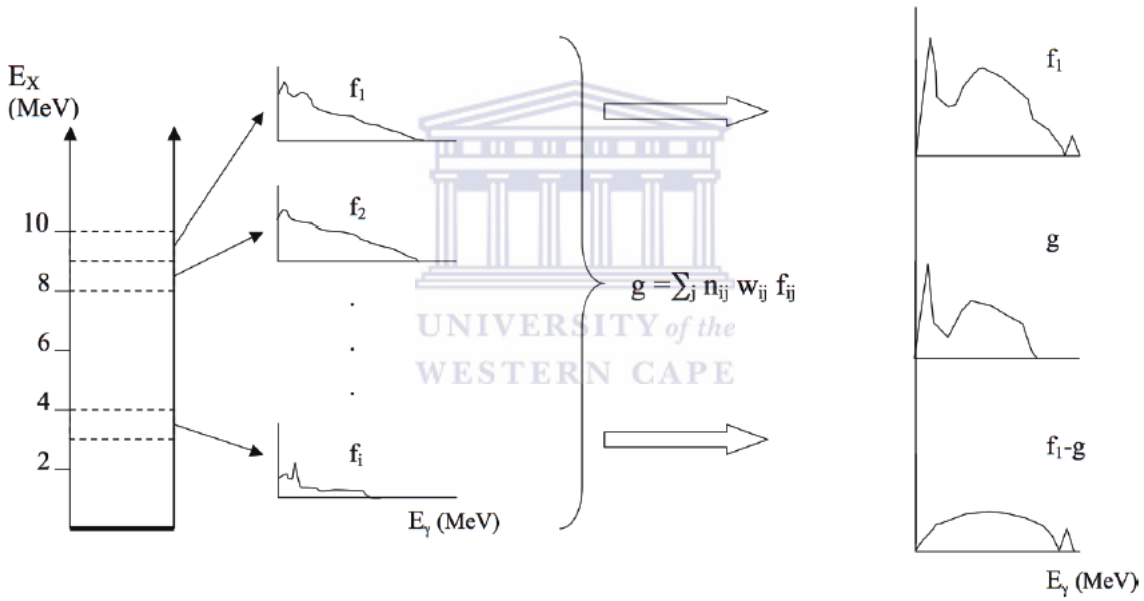

Figure 2.14. A demonstration of principles of the first-generation method [59].

A matrix of excitation energy, E_x, vs unfolded γ-rays is divided into excitation energy bins i (typically width of 120 - 240 keV), depending on the experimental energy resolution and statistics, in order to extract the E_x, vs unfolded primary γ-ray matrix. A demonstration of the principle of the first-generation method is shown in figure 2.14. The first-generation γ-ray spectrum, h_i, of each excitation energy bin i is approximated by [59]

$$h_i = f_i - g_i \tag{2.31}$$

where f_i is a γ-ray spectrum of excitation energy bin i, and g_i is a weighted sum of all spectra of the excitation bins $j < i$ such that

$$g_i = \sum_{j<i} n_{ij} w_{ij} f_j. \tag{2.32}$$

The unknown coefficients w_{ij} represent the probability of the decay from bin i to bin j with $\sum_j w_{ij} = 1$. The weighting coefficients w_{ij} contains the distribution of branching ratios as a function of γ-ray energy and correspond directly to the unfolded first-generation γ-ray spectrum, h_i, for bin i. This close relationship allows simultaneous determination of w_{ij} and h_i using the fast converging iterative procedure as described in Ref. [58]. The coefficients n_{ij} are correction factors for the different cross sections of populating levels in bin i and lower-lying levels in bin j, and are determined in such a way that the total area of each spectrum f_i, multiplied by n_{ij}, gives the same number of cascades. This is achieved by using the multiplicity normalization method [58], where the normalization coefficients n_{ij} applied to bin i when subtracting bin j is given by

$$n_{ij} = \frac{A(f_i)/\langle M_i \rangle}{A(f_j)/\langle M_j \rangle} = \frac{\langle M_j \rangle A(f_i)}{\langle M_i \rangle A(f_j)}. \tag{2.33}$$

UNIVERSITY of the
WESTERN CAPE

The parameters $\langle M_i \rangle$ and $A(f_i)$ are the average γ-ray multiplicity in bin i and the area (or total number of counts) of spectrum f_i, respectively. The average γ-ray multiplicity can be expressed as:

$$\langle M_i \rangle = \frac{E_x^i}{\langle E_{\gamma,i} \rangle} \tag{2.34}$$

where E_x^i is the excitation energy of bin i, and $\langle E_{\gamma,i} \rangle$ the average γ-ray energy carried by a γ ray decaying from energy bin i. In cases where $\langle M_i \rangle$ is well determined, an area consistency check can be applied to Eq. (2.31) (more details in Ref. [56]). The additional benefit to this *first-generation method* is that the obtained first-generation γ-ray spectrum can be compared to the exact solution (simulated spectra). An example of the first-generation γ-ray matrix, extracted using the first-generation method, is shown in figure 2.15 alongside with the respective unfolded matrix obtained using the unfolding procedure as discussed in the previous section.

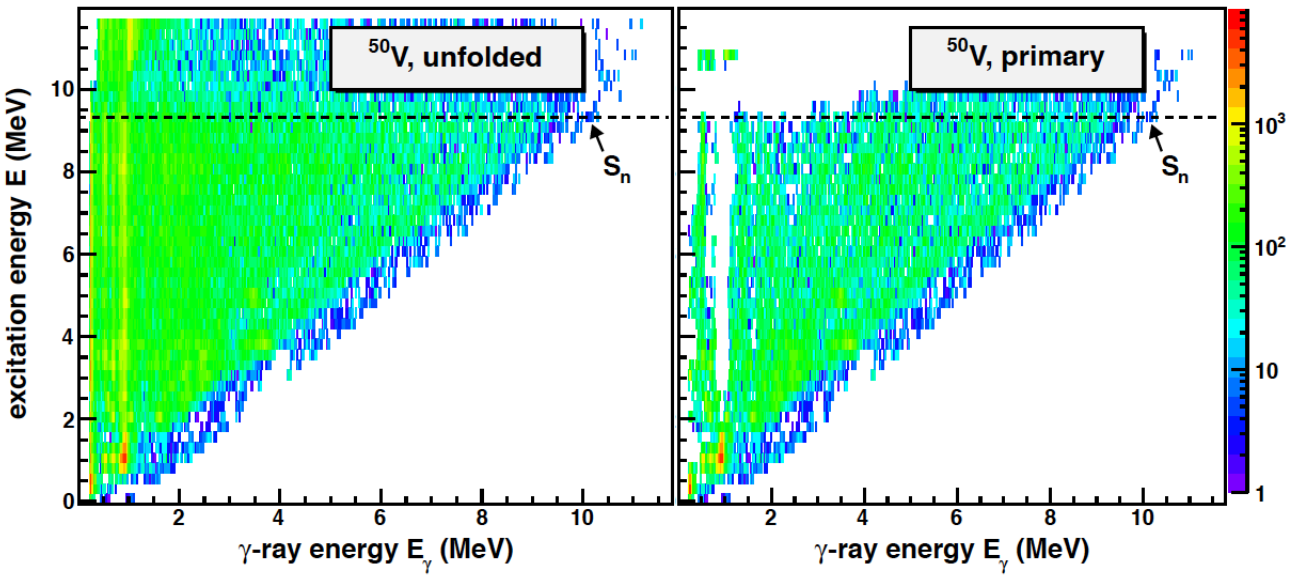

Figure 2.15. The E_x vs. E_γ matrix (left) and first-generation γ-ray matrix (right) for ^{50}V [56].

2.2.4 Extraction of nuclear level density and γ-ray strength function in the quasi-continuum

UNIVERSITY of the

The NLD and γSF can be extracted from the distribution of primary γ-rays, given by $P(E_x, E_\gamma)$ which is proportional to the transition probability of emitting a γ ray of energy E_γ. The transition probability, λ_{if}, between the initial state i and the final state f depends on the matrix element $|M_{if}|^2$ and the density of the final states, $\rho(E_f)$, according to Fermi's Golden Rule: $\lambda_{if} = \frac{2\pi}{\hbar}|M_{if}|^2\rho(E_f)$ [60]. Furthermore, the transition probability for a decay into any specific combination of final states is independent of how the compound nucleus [19, 61] was formed[4]. The subsequent decay of the compound states will mainly be restrained by statistical rules. Hence, the decay probability, $P(E_x, E_\gamma)$, of a γ ray with energy E_γ to be emitted from a specific initial excited state, with energy E_x, is proportional to the level density $\rho(E_f)$ of the final state, with energy $E_f = E_x - E_\gamma$, and the γ-ray transmission coefficient $\mathcal{T}(E_\gamma)$ [55, 56]:

$$P(E_x, E_\gamma) \propto \rho(E_f)\mathcal{T}(E_\gamma) \tag{2.35}$$

[4]The assumption holds for compound reactions, where a nuclear reaction exists as a two-stage process comprising the formation of a relatively long-lived intermediate state (10^{-18} s – 10^{-16} s) of the particle-target composite system and its subsequent decay.

where $\mathcal{T}(E_\gamma)$ is independent of the excitation energy and only depends on the γ-ray energy. This is true, assuming that the Brink Hypothesis [44] holds for all types of collective decay modes, which states that the collective modes of nuclear excitation built on excited states have the same properties as those built on the ground states. The relationship in Eq. (2.35) is only appropriate at high level densities. Henceforth, $\rho(E_f)$ and $\mathcal{T}(E_\gamma)$ can be extracted using an iterative procedure [55], where the theoretical first-generation γ-ray matrices $P_{th}(E_x, E_\gamma)$ are continuously fitted to the experimental first-generation γ-ray matrices $P(E_x, E_\gamma)$ by performing a global χ^2 minimization

$$\chi^2 = \frac{1}{N_{free}} \sum_{E_x=E_x^{min}}^{E_x^{max}} \sum_{E_\gamma=E_\gamma^{min}}^{E_x^{max}} \left(\frac{P_{th}(E_x, E_\gamma) - P(E_x, E_\gamma)}{\Delta P(E_x, E_\gamma)} \right)^2 \tag{2.36}$$

where N_{free} and $\Delta P(E_x, E_\gamma)$ are the number of degrees of freedom and the uncertainty in the experimental first-generation γ-ray matrix $P(E_x, E_\gamma)$, respectively. $P(E_x, E_\gamma)$ is normalized [55] such that $\sum_{E_\gamma=E_\gamma^{min}}^{E_x} P(E_x, E_\gamma) = 1$. The theoretical first-generation γ-ray matrix is given by

$$P_{th}(E_x, E_\gamma) = \frac{\rho(E_f)\mathcal{T}(E_\gamma)}{\sum_{E_\gamma=E_\gamma^{min}}^{E_x} \rho(E_f)\mathcal{T}(E_\gamma)}. \tag{2.37}$$

UNIVERSITY of the WESTERN CAPE

An example of a normalized $P(E_x, E_\gamma)$ is displayed in figure 2.16, together with the corresponding $P_{th}(E_x, E_\gamma)$, showing the limits with which the $P(E_x, E_\gamma)$ was extracted.

Once the $\rho(E_f)$ and $\mathcal{T}(E_\gamma)$ have been simultaneously extracted, there exist infinitely many solutions of the experimental first-generation γ-ray matrix $P(E_x, E_\gamma)$ of the form:

$$\tilde{\rho}(E_f) = A\rho(E_f)e^{\alpha E_x} \tag{2.38}$$

and

$$\tilde{\mathcal{T}}(E_\gamma) = B\mathcal{T}(E_\gamma)e^{\alpha E_\gamma} \tag{2.39}$$

where α, A and B are transformation parameters, which correspond to physical solutions, and are determined from external data. The slope correction parameter α and the absolute value A of the level density $\rho(E_f)$ in Eq. (2.38) are determined by adjusting the function $\rho(E_f)$ to fit the known discrete levels at low excitation energies, and it is further interpolated to fit $\rho(S_n)$ in the high excitation energy region. The normalization procedure for the level density of ^{164}Dy

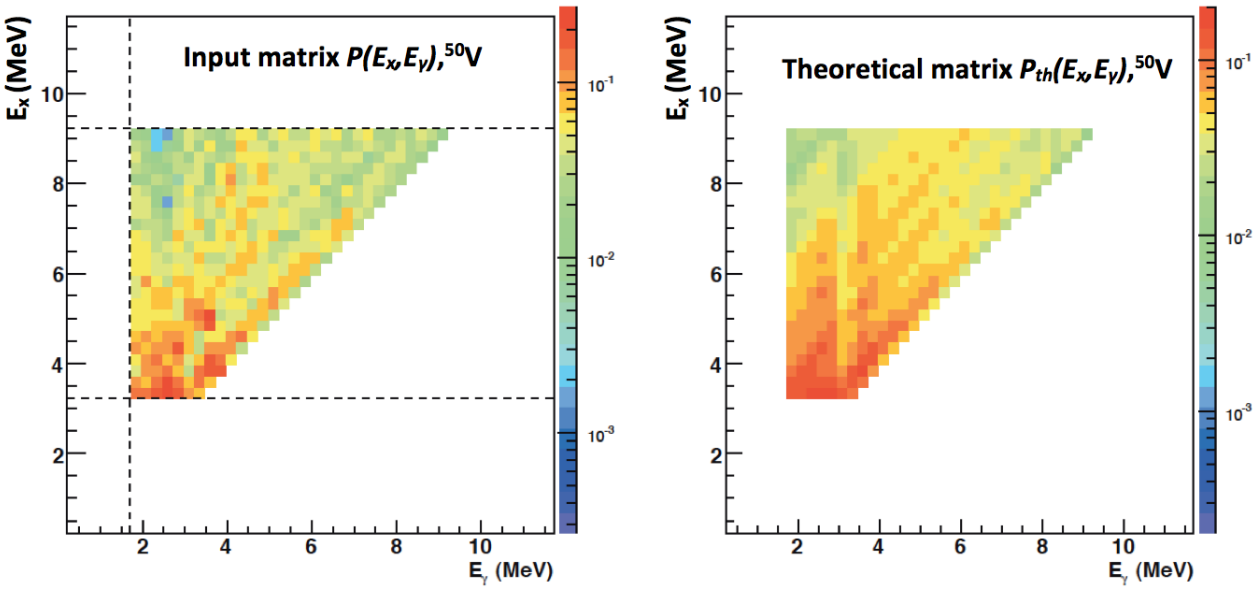

Figure 2.16. The $P(E_x, E_\gamma)$ (left) and corresponding $P_{th}(E_x, E_\gamma)$ (right) of ^{50}V, the limits (E_x^{min}, E_x^{max}, and E_γ^{min}) set in the $P(E_x, E_\gamma)$ for extraction are also shown (dashed lines) [56].

is shown in figure 2.17.

UNIVERSITY of the WESTERN CAPE

The $\rho(S_n)$ is calculated according to Ref. [56], as shown below

$$\rho(S_n) = \frac{2\sigma^2}{D_0(J_T+1)e^{[-(J_T+1)^2/2\sigma^2]} + e^{\left(-J_T^2/2\sigma^2\right)}J_T} \tag{2.40}$$

where σ^2, D_0, J_T are the spin cut-off parameter, average neutron resonance spacing as determined from (n,γ) reactions and target spin in (n,γ) or (p,γ) reactions (for the A-1 nucleus), respectively. The average neutron resonance spacing D_0 and spin of the target nucleus J_T, are usually taken from Refs. [22, 63], respectively. The spin cut-off parameter σ^2 is calculated from the back-shifted fermi gas formula (see section 2.1.1.1 for BSFG).

At this point, the slope of the $\mathcal{T}(E_\gamma)$ has already been determined through normalization of $\rho(E_f)$, as discussed previously. The absolute normalization of $\mathcal{T}(E_\gamma)$ is achieved through determination of the constant B, which is calculated from the average total radiative width $\langle\Gamma_\gamma\rangle$ of neutron s-wave capture resonances at S_n, according to [56]

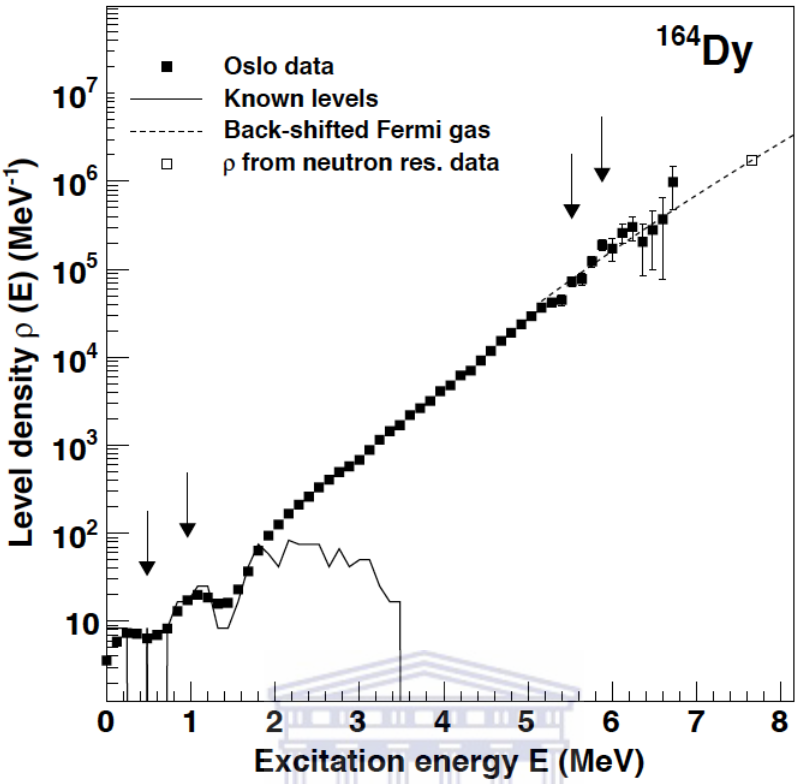

Figure 2.17. Normalization procedure of the level density (black squares) of ^{164}Dy [62]. The sets of vertical arrows at low and high E_x, indicate regions where $\rho(E_x)$ was normalized.

UNIVERSITY of the
WESTERN CAPE

$$\langle \Gamma_\gamma(S_n, J_T \pm \frac{1}{2}, \pi_T)\rangle = \frac{D_0}{4\pi}\int_0^{S_n} dE_\gamma \tilde{\mathcal{T}}(E_\gamma)\rho(S_n - E_\gamma) \times \sum_{J=-1}^{1} g(S_n - E_\gamma, J_T \pm \frac{1}{2} + J) \tag{2.41}$$

where J_T and π_T are the spin and parity of the target nucleus, and $\rho(S_n - E_\gamma)$ represents the experimental level density. The spin distribution of the level density is defined as [56]:

$$g(E_x, J) = \frac{2J+1}{2\sigma^2} e^{(-(J_T+1)^2/2\sigma^2)} \tag{2.42}$$

and $g(E_x, J)$ is normalized to unity. Assuming that the statistical decay is dominated by electric and magnetic dipole transitions, then Eq. (2.39) can be expressed as follows

$$B\mathcal{T}(E_\gamma) = B\sum_{XL}\mathcal{T}_{XL}(E_\gamma) \approx B[\mathcal{T}_{E1}(E_\gamma) + \mathcal{T}_{M1}(E_\gamma)] \tag{2.43}$$

where X and L are the electromagnetic character and multipolarity of the radiation, respectively. Furthermore, the γ-ray transmission coefficient is related to γSF by

$$\mathcal{T}_{XL}(E_\gamma) = 2\pi E_\gamma^{(2\ell+1)} f_{XL}(E_\gamma) \tag{2.44}$$

where $\ell = 1$, and so the experimental γSF, $f(E_\gamma)$, is given by

$$f(E_\gamma) = f_{E1}(E_\gamma) + f_{M1}(E_\gamma) = \frac{B\mathcal{T}(E_\gamma)}{2\pi E_\gamma^3}. \tag{2.45}$$

The typical nuclear level densities, γ-ray transmission coefficients and γSFs that have been obtained from previous experiments using the Oslo method, are shown in figure 2.18 and 2.19.

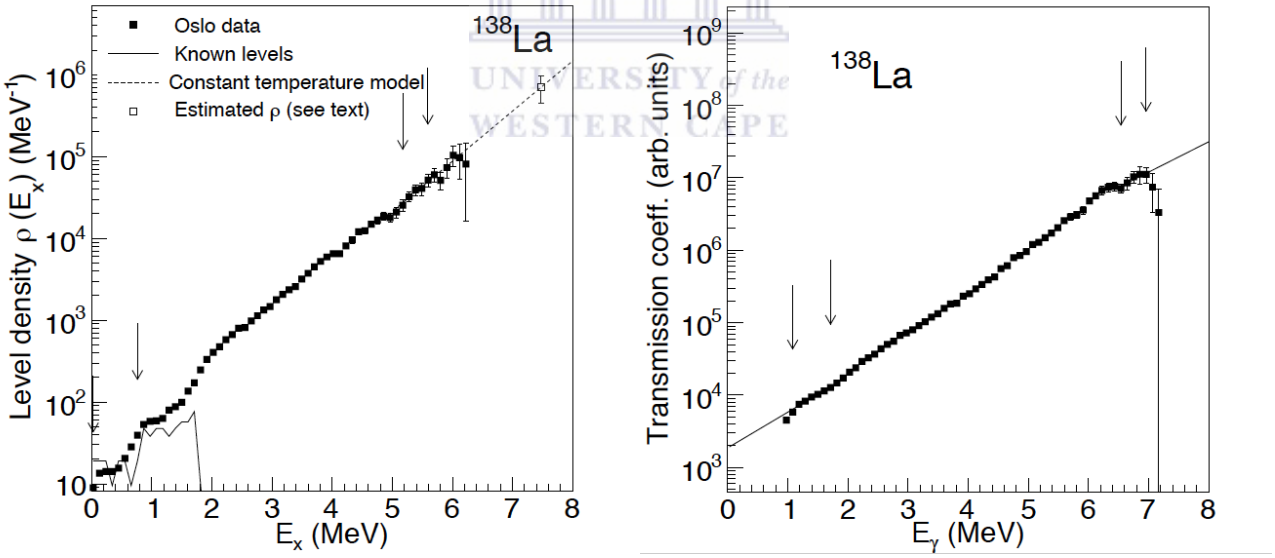

Figure 2.18. The NLD and transmission coefficient of ^{138}La [64]. The normalization of the level density was performed using the constant temperature model [17] (left panel). The vertical arrows show the two regions where the χ^2 minimization has been performed, between the experimental data and the extrapolation. The right panel shows the $\mathcal{T}(E_\gamma)$.

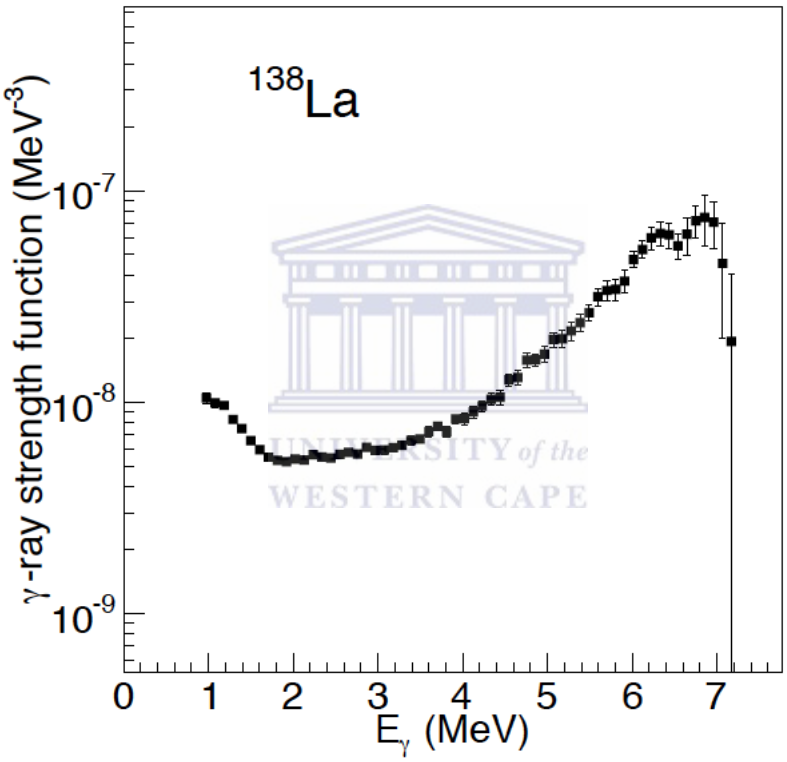

Figure 2.19. The γSF of ^{138}La [64].

Chapter 3

Experimental details

An experiment was performed using the inelastic scattering (^{3}He,^{3}He'γ) and the transfer reaction (^{3}He,$\alpha\gamma$) at the Oslo cyclotron laboratory, with 34 MeV ^{3}He beam energy and an average intensity of $\approx$ 2 enA[1]. The charged ejectiles in coincidence with γ rays were recorded using the silicon ring particle telescope array (SiRi) [65] and the γ rays were recorded using the multi-detector NaI(Tl) array (CACTUS) [59]. A self-supporting ^{181}Ta natural target of 0.8 mg/cm^2 thickness was positioned at the center of the CACTUS array. The Oslo cyclotron, SiRi and CACTUS arrays are briefly described in this chapter. Another reaction of particular interest, ^{28}Si(d,p), with 12.5 MeV deuteron beam on a 3.5 mg/cm^2 natural ^{28}Si target was performed for calibration purposes. The details of this reaction are also explained in this chapter.

UNIVERSITY of the
WESTERN CAPE

3.1 The Oslo cyclotron laboratory

The Oslo Cyclotron Laboratory (OCL) houses an MC-35 scanditronix cyclotron which delivers pulsed light-ion beams. A 34 MeV pulsed beam with typical RF frequency of $\approx$ 14.47 MHz for ^{3}He ions was used. Figure 3.1 shows an outline of the experimental setup at the OCL. After extraction of the beam from the cyclotron, the slit, S1, and quadrupole magnet, Q1, allow for collimation and further focusing of the beam, respectively. The beam is then deflected by 90° using the analyzing magnet into the experimental hall. The 34 MeV ^{3}He beam has a typical energy resolution of $\approx$ 50-80 keV, when the 2 mm slits are used in front of the analyzing magnet. The so-called doubly focusing analyzing magnet focuses the beam in both the horizontal and vertical direction. The beam is further collimated and focused using the adjustable slits (S2,

[1]The Q-values of nuclear reactions ^{181}Ta(^{3}He,^{3}He'γ) and ^{181}Ta(^{3}He,$\alpha\gamma$) are 0 keV and 13 MeV.

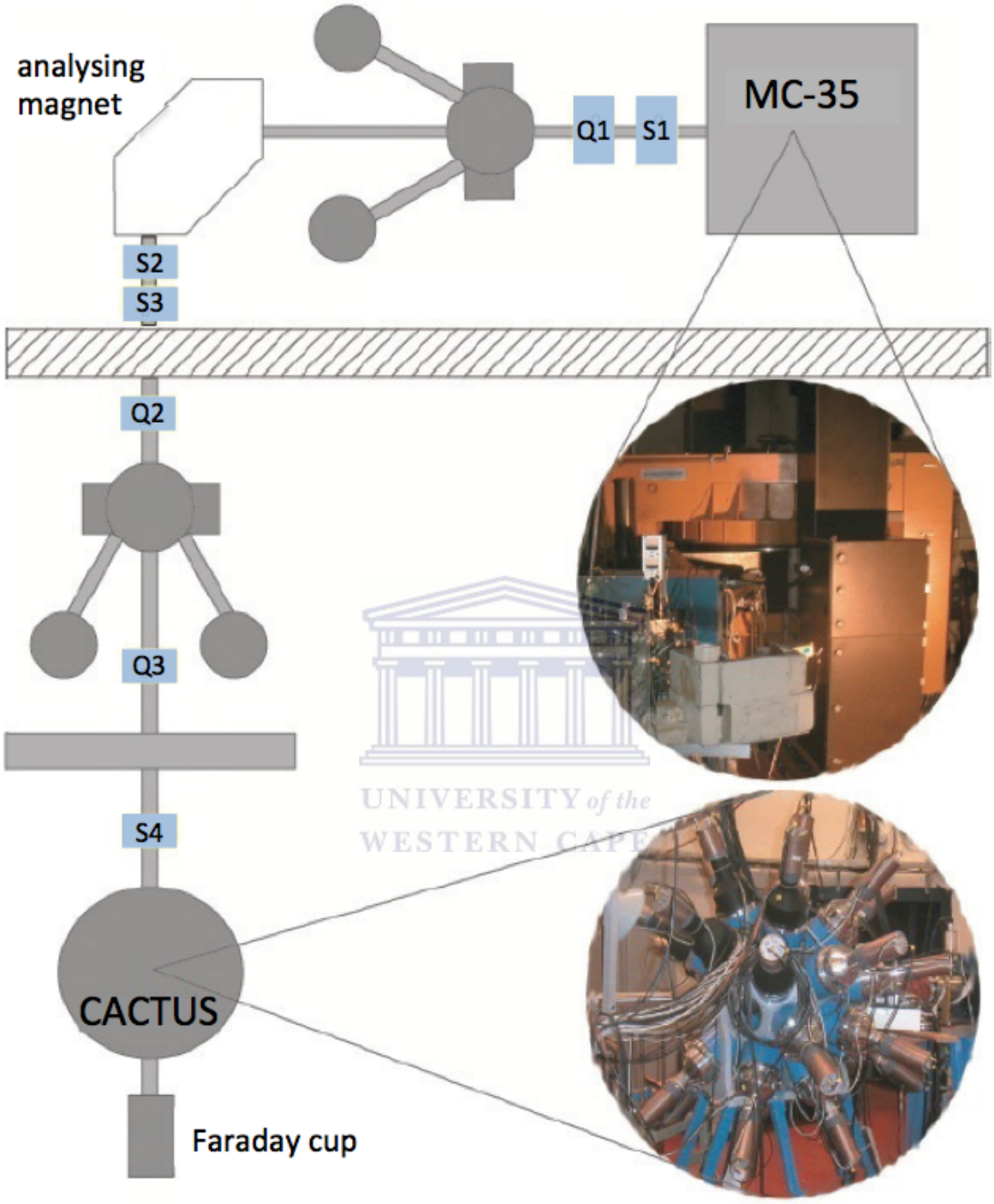

Figure 3.1. Experimental setup at the OCL, figure adapted from [66].

S3 and S4) and quadrupole magnets (Q2 and Q3), respectively. The beam spot on target has a typical diameter of ≈ 1-2 mm, after passing slit S4. The beam reaches the target chamber, where the target is located at the center of the multi-detector array CACTUS. Inside the target chamber, the silicon ring (SiRi) particle detector system was mounted for detecting charged

particles from the reaction in coincidence with the γ rays.

3.2 CACTUS

The multi-detector array CACTUS is used to detect γ radiation. The name CACTUS arises from the similarity of the detector setup with a cactus plant. γ rays from the reaction are recorded with 26 NaI(Tl) collimated detectors which have crystal dimensions of 5"×5" each [67]. The crystals are mounted on a spherical frame, enclosing the target chamber containing the particle telescopes (see figure 3.2). The crystals are positioned 22 cm away from the target. In addition, on the front surface of each NaI(Tl) crystal, a 10 cm thick lead collimator with 7 cm diameter was mounted. CACTUS covers a solid angle of 16% of 4π sr from $\Omega = \mathrm{NA}/4\pi R^2$, where N = 26 is the number of detectors in the array, $\mathrm{A} = \pi r^2$ is the collimated front area of each crystal with a radius of 3.5 cm, and R = 22 cm is the distance between the detector and the target. The total efficiency was measured to be $\approx$ 14.1% for a 1332 keV γ-ray transition, with a relative energy resolution of $\approx$ 7% FWHM. In front of the each NaI(Tl) detector, a 2 mm thick copper absorber is fixed to suppress X-rays. Each NaI(Tl) crystal is surrounded by a 3 mm thick lead shield to reduce crosstalk between neighboring detectors as shown in figure 3.3.(a). The plastic ring is used to hold the NaI(Tl) detector in place.

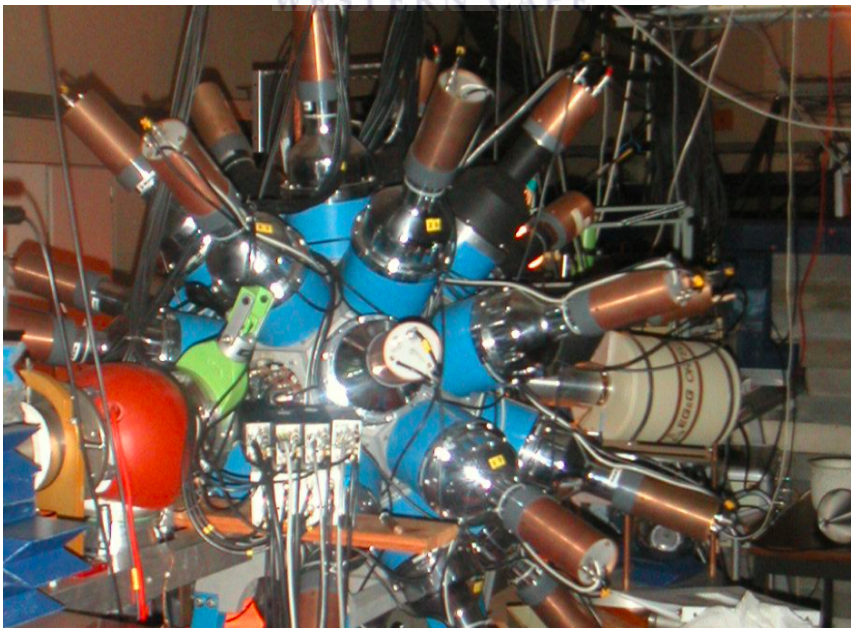

Figure 3.2. The multi-detector NaI(Tl) array, CACTUS [59].

3.3 SIRI array

The emitted charged particles from the nuclear reactions were detected using eight collimated $\Delta E - E$ Si particle telescopes, mounted inside the target chamber, surrounded by the multi detector-array CACTUS (see figure 3.3.(b)). The ejectiles include p, d, t, ^{3}He, and ^{4}He, which are identified in the $\Delta E - E$ telescopes. The front (ΔE) and back (E) detectors have thicknesses of ≈ 130 μm and 1550 μm, respectively [65]. Each ΔE detector is segmented into 8 strips, giving a total of 64 $\Delta E - E$ channels. The telescopes are positioned a few mm apart as shown in figure 3.4. An aluminium foil with a thickness of 10.5 μm is placed in front of the $\Delta E - E$ telescopes, to shield them from δ-electrons that are emitted from target atoms when bombarded by the beam particles. The $\Delta E - E$ Si particle telescopes are placed 5 cm away from the target and were installed at backward angles, covering an angular range of $\theta \approx 126°$ to 140°, with respect to the beam axis (see figure 3.4). The average energy resolution[2] of the SiRi array is ≈ 350 keV.

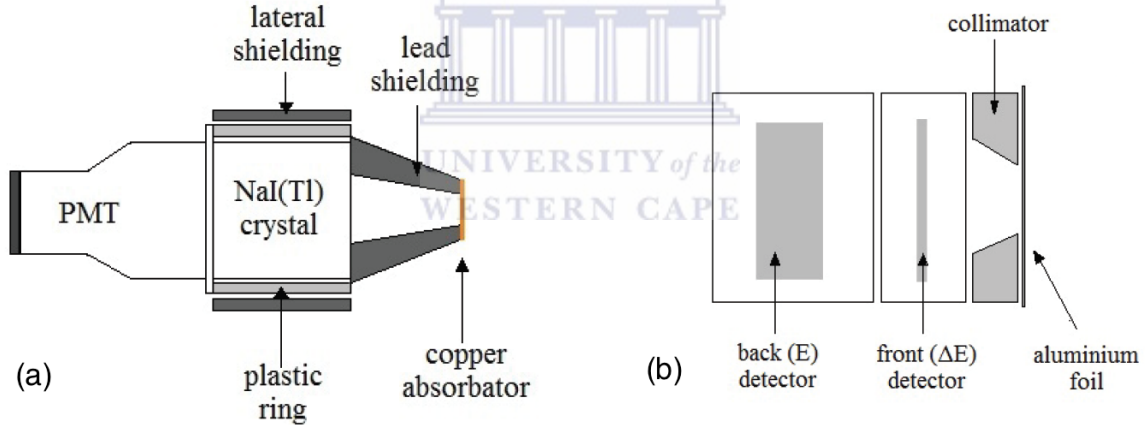

Figure 3.3. The multi-detector array CACTUS (a) and $\Delta E - E$ Si particle telescopes (b) used in the experiment [66].

3.4 Electronics and data acquisition

The electronics setup at the OCL is placed in two different locations. The first location, in the experimental hall, include a multichannel power supply system connected to photo-multiplier tubes of the NaI(Tl) detectors of the CACTUS array, and it also consists of several pre-amplifiers

[2]The energy resolution of the particle telescope is determined by measuring the full width half maximum (FWHM) of the ^{3}He beam elastically scattering off the ^{181}Ta target.

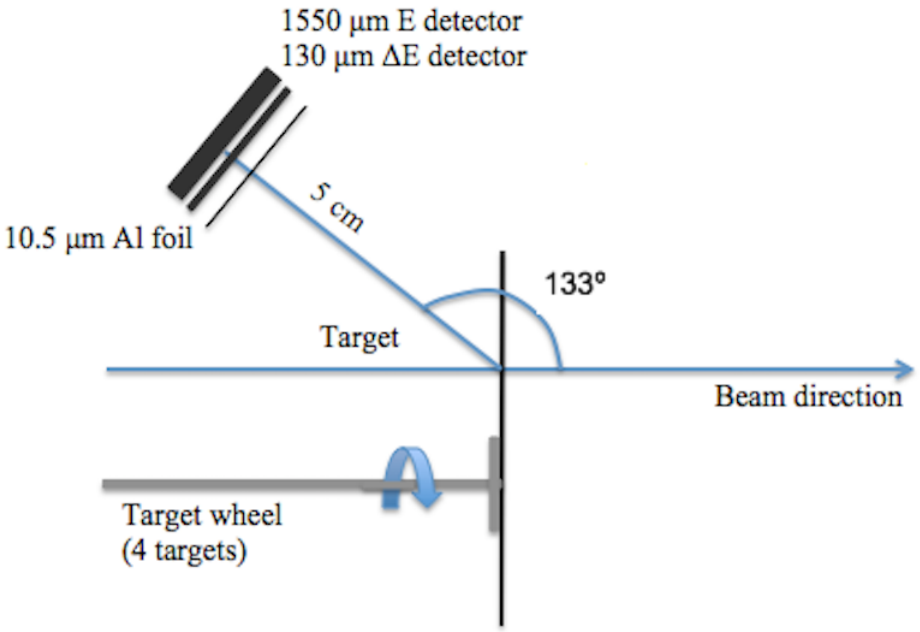

Figure 3.4. The $\Delta E - E$ Si particle telescopes are located at backward angles with respect to the beam axis and 5 cm away from the target, figure adapted from Ref. [65].

collecting energy signals from the $\Delta E - E$ Si particle telescopes. The pre-amplifiers are utilized to enhance the signal strength from the front and back detectors, and are placed close to the target chamber to reduce effects of electronics noise and interference. The $\Delta E - E$ signals are transported to the data acquisition electronics setup in an adjacent room, as differential pair of signals to the high-quality multichannel spectroscopic amplifiers and timing-filter amplifiers (TFA) with integrated leading edge discriminators. Signals from the particle detectors are used as start signals and the respective signals from CACTUS array are used as stop signals in the time-to-digital converters (TDC). A valid trigger is constructed when a $\Delta E - E$ Si event is in coincidence with a NaI(Tl) event within a 200 ns time window. The TDC measures the time difference between the $\Delta E - E$ and NaI(Tl) signals overlapping within the desired time window. A schematic diagram of the electronics setup is shown in figure 3.5. This diagram is a representation of the electronic setup for each of the 64 individual ΔE and E Si channels and 26 NaI(Tl) detectors. Each signal from a detector, which is connected to a preamplifier is then transported to the spectroscopic amplifier (slow signals) and TFA (fast signals) for further processing. The leading edge discriminator (LED) is used to filter out signals of interest from the TFA by use of an adjustable threshold. The signals are then send to the coincidence unit as logic pulses. Once a NaI(Tl) event and $\Delta E - E$ Si event overlap in the coincidence unit, a "gate" signal triggers the analog-to-digital converter (ADC) and TDC to send out energy and

timing information to the data acquisition system.

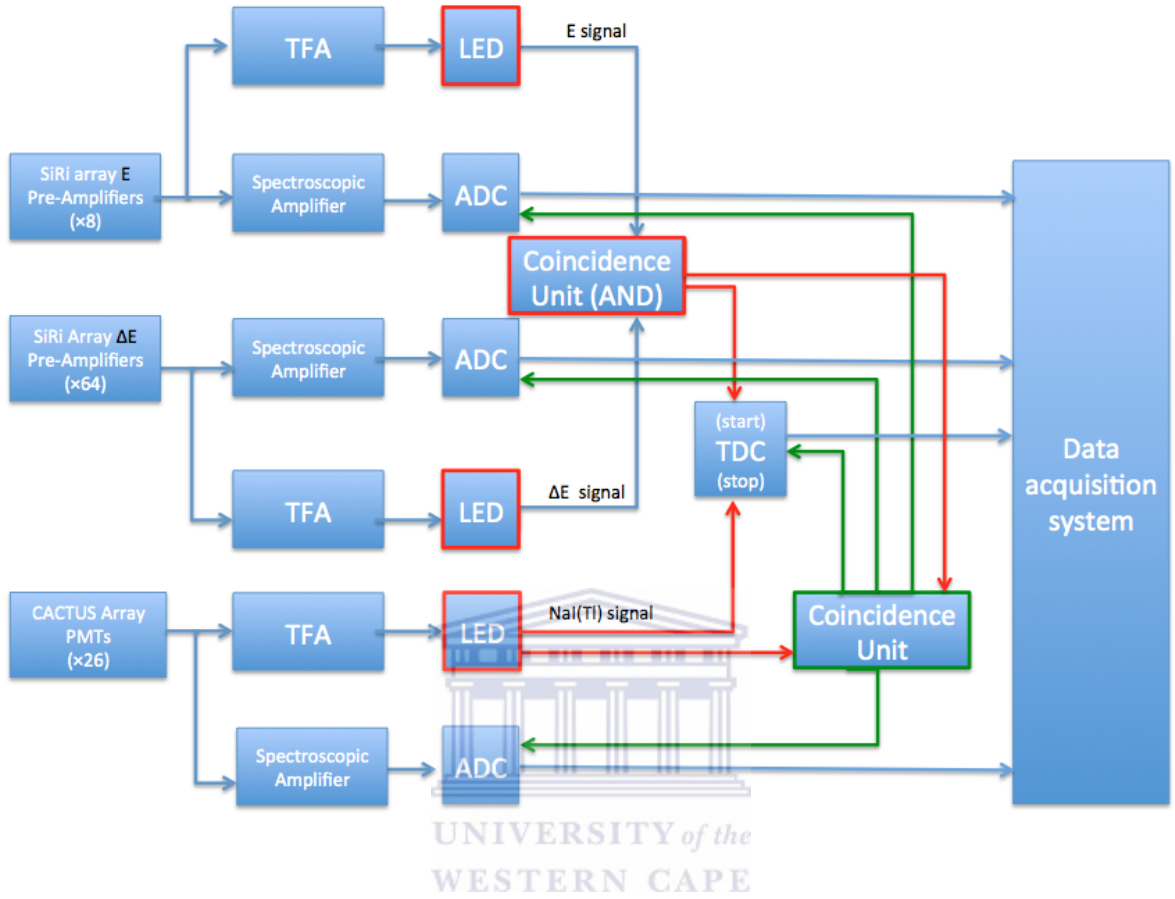

UNIVERSITY of the
WESTERN CAPE

Figure 3.5. A schematic diagram of the electronics setup, located in the data room at the OCL. Each individual NaI(Tl), ΔE and E signal is processed by a separate spectroscopic amplifier, TFA, LED, and ADC. Additionally, each NaI(Tl) time signal is asigned its own TDC channel.

Chapter 4

Data analysis and results

4.1 Calibration of the SIRI array

UNIVERSITY of the
WESTERN CAPE

The $\Delta E - E$ Si particle detectors were calibrated using the SiRi kinematic calculator [68] with a linear calibration, where the measured particle energies E are related to the detector energy offset a_0 and the slope a_1 multiplied by the channel number ch of the spectrum,

$$E = a_0 + a_1 \times ch \tag{4.1}$$

where energy E is the measured particle energies expected to be deposited by the charged ejectiles in the SiRi array at different scattering angles. These particle energies are obtained using the SiRi kinematic calculator which is based on the Bethe-Bloch formula [69]. The Bethe-Bloch formula describes the energy loss of a particle traveling a distance x into a material as shown below:

$$-\left\langle \frac{dE}{dx} \right\rangle = Kz^2 \frac{Z}{A} \frac{1}{\beta^2} \left[\frac{1}{2} ln \frac{2m_e c^2 \beta^2 \gamma^2 T_{max}}{I^2} - \beta^2 - \frac{\delta(\beta\gamma)}{2} \right] \tag{4.2}$$

where z, Z and A are the atomic number of incident particle, atomic number of material and atomic mass of material, respectively. The parameters I, T_{max} and $\delta(\beta\gamma)$ are the mean excitation energy of the material, maximum kinetic energy transferred in a single collision and density effect correction to ionization energy loss[1]. The particle energy loss is relatively

[1]The constant $K{=}4\pi N_A r_e^2 m_e c^2{=}0.307$ MeV g^{-1}cm^2 for A=1 g mol^{-1} and $T_{max}{=}2m_e c^2\beta^2\gamma^2/(1{+}2\gamma m_e/M{+}(m_e/M)^2)$ where the velocity $\beta = v/c$ and the Lorentz factor $\gamma = (1-\beta^2)^{-2}$. The parameters N_A, c, r_e and m_e are the Avogadro's number, speed of light, classical electron radius and electron mass, respectively.

independent of the target material and the incident particle mass. Therefore a given incident particle with atomic number z will primarily lose a different amount of its energy in the ΔE and E detectors as a function of its total kinetic energy. The kinematic calculator also accounts for the energy loss corrections of the charged particles traveling through the aluminium foil placed in front of the particle telescopes.

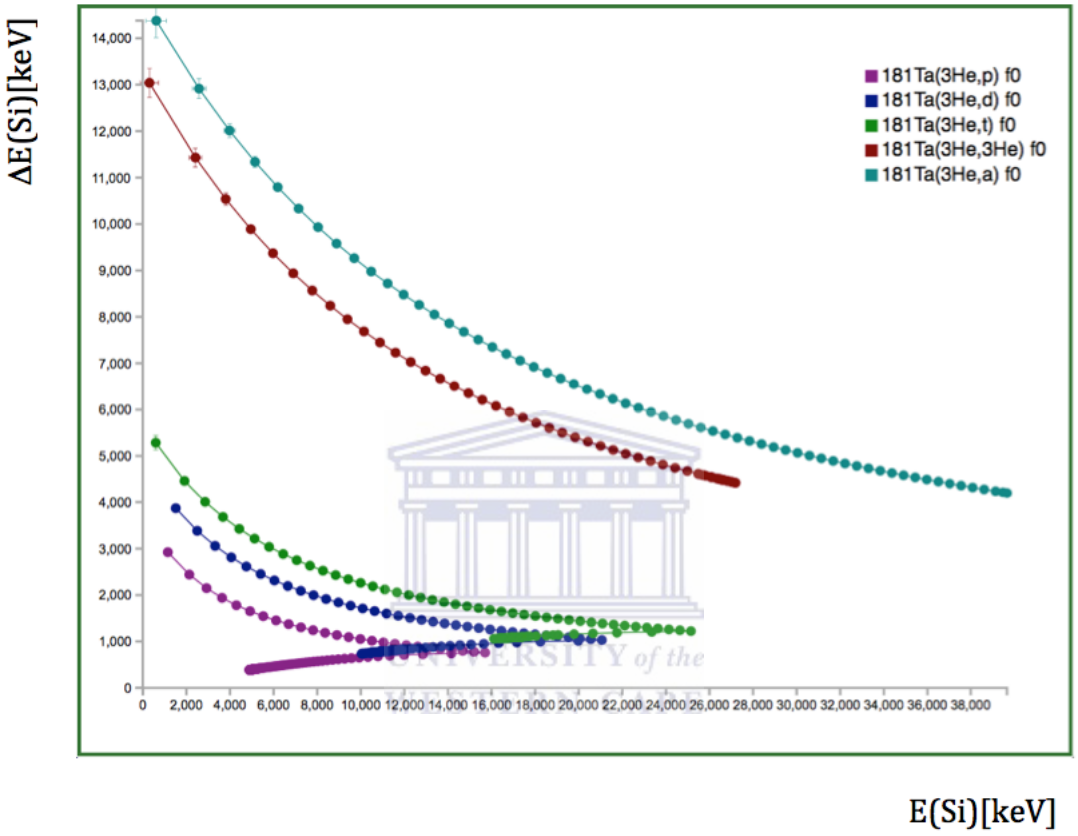

Figure 4.1. Calculated $\Delta E - E$ energy deposition of the innermost ring obtained using the SiRi kinematic calculator [68].

Figure 4.1 shows calculated particle energies deposited in the $\Delta E - E$ Si detectors for the ^{181}Ta(^{3}He,X) reaction, at 34 MeV beam energy, where X represents protons, deuterons, tritons, ^{3}He or ^{4}He. The corresponding experimental $\Delta E - E$ data with data from all rings combined before calibration is shown in figure 4.2, with "banana-shaped" curves for each particle type. This figure shows particle energies deposited in all the $\Delta E - E$ rings, covering an angular range of $\theta \approx 126°$ to $140°$ with respect to the beam axis. When all particle telescopes are properly calibrated, the data of all the rings can be added together, and this allow for a clear identification of the energy distribution for all different charged particles. Such a plot of the calibrated $\Delta E - E$ detectors added together after calibration is shown in figure 4.3.

The particle-identification technique makes it possible to gate on a specific particle type utilizing

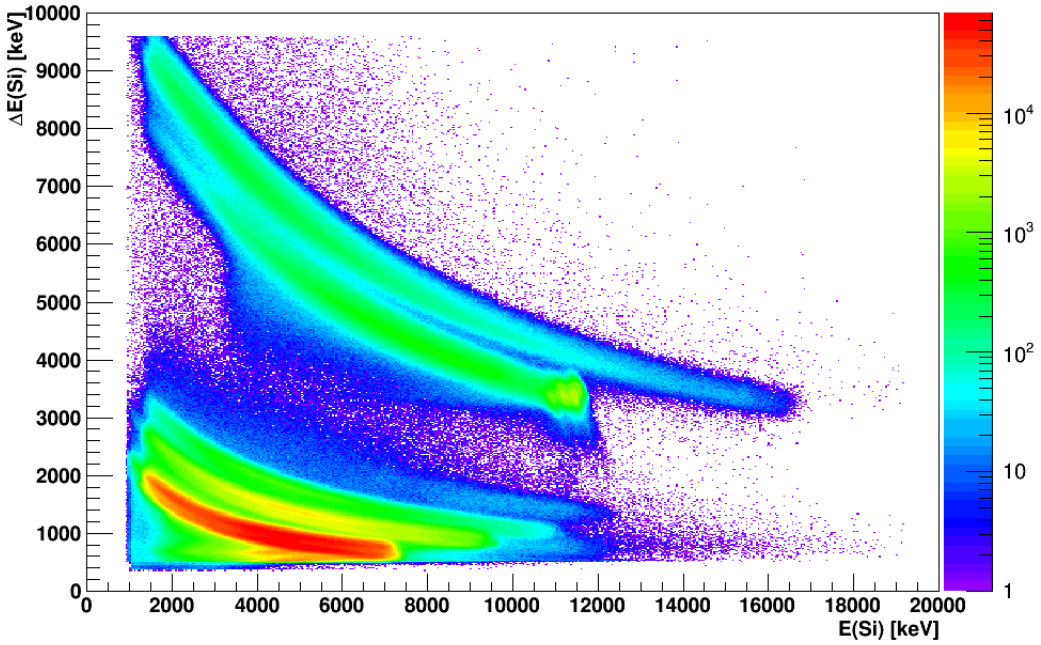

Figure 4.2. $\Delta E - E$ signals for the ^{181}Ta(^{3}He,X) reaction, showing the reaction channels before calibration.

UNIVERSITY of the
WESTERN CAPE

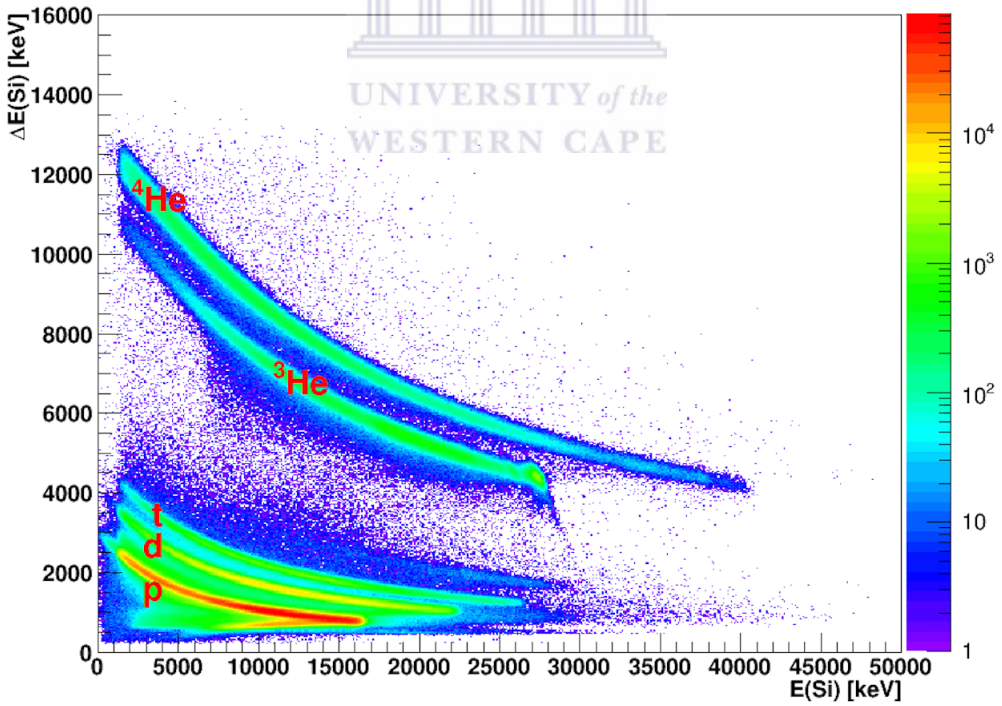

Figure 4.3. $\Delta E - E$ plots for the ^{181}Ta(^{3}He,X) reaction after calibration. Various reaction channels are well identified.

its unique energy range curve in the Si particle telescopes. Upon reactions of the target nucleus ^{181}Ta with the ^{3}He beam, various reaction channels are opened (see figure 4.3). Gating on the

particles of interest, which in the present case are ^{3}He and ^{4}He from the ^{181}Ta(^{3}He,^{3}He'γ)^{181}Ta and ^{181}Ta(^{3}He,$\alpha\gamma$)^{180}Ta reactions, allows for a significant reduction of unwanted channels and some background events. A plot of such a gate for ^{181}Ta(^{3}He,^{3}He'γ)^{181}Ta is shown in figure 4.4. A gate was set on the α particles for ^{181}Ta(^{3}He,$\alpha\gamma$)^{180}Ta reaction as well (see figure 6.1 in appendix A).

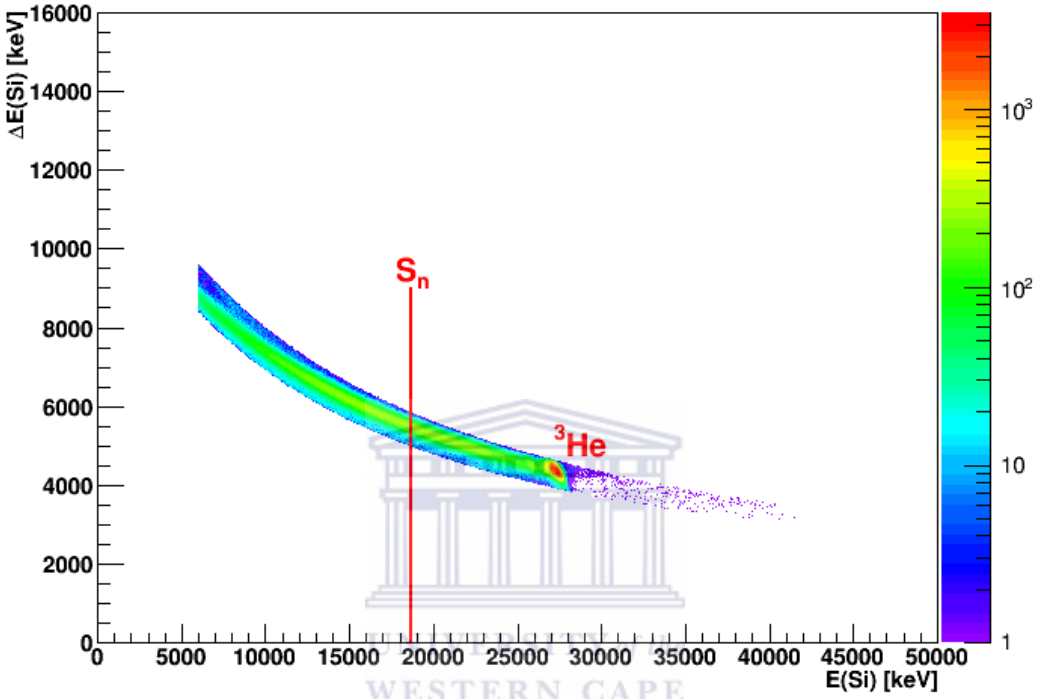

Figure 4.4. $\Delta E - E$ plots for the ^{181}Ta(^{3}He,X) experiment gated on ^{3}He particles. S_n indicates the location of neutron separation energy.

The $\Delta E - E$ particle telescopes were calibrated using the ^{28}Si(d,p) reaction, following the same procedure used for calibrating the particle telescopes in the ^{181}Ta(^{3}He,X) experiment. The corresponding ^{28}Si(d,X) $\Delta E - E$ plot after calibration is shown in figure 4.5, which clearly demonstrates the particle energy distribution of different charged ejectiles detected in the SiRi array.

4.2 The excitation energy spectra

The measured ^{3}He and α particle energies were transformed to excitation energy E_x of the residual nucleus ^{181}Ta and ^{180}Ta, from the reaction Q-values and kinematics, as shown below

$$E_x = KE_{beam} - KE_{ejectile} - KE_{recoil} - E_{loss} + Q_{value}, \tag{4.3}$$

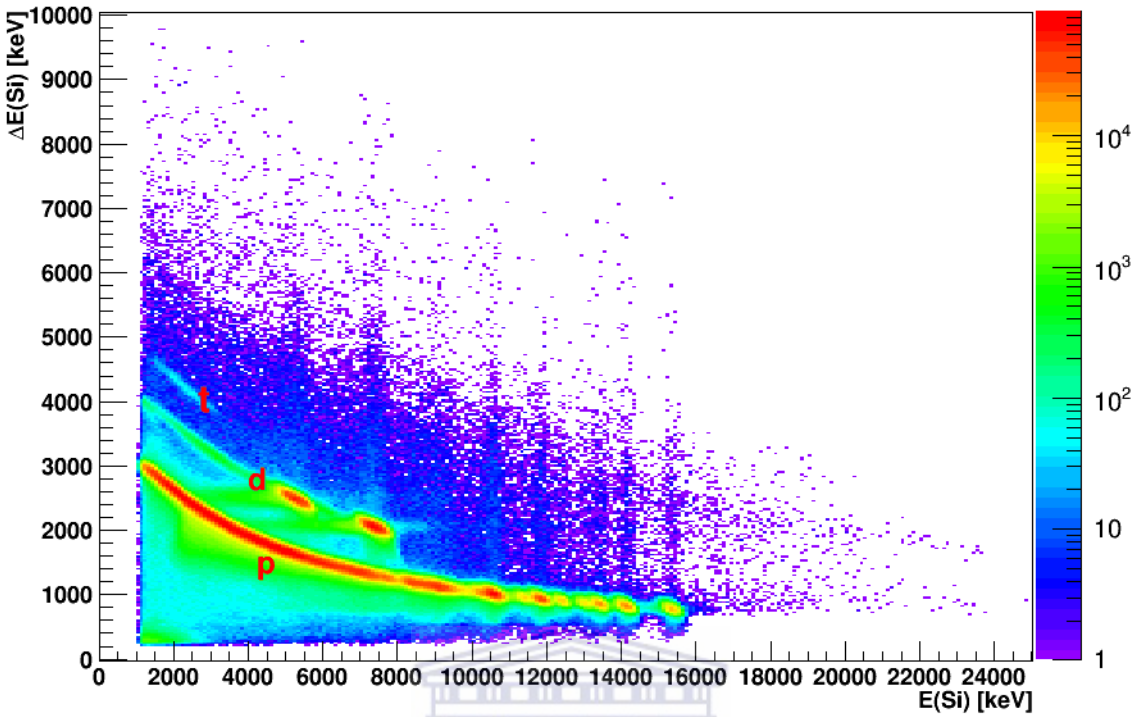

Figure 4.5. The calibrated $\Delta E - E$ plot for the ^{28}Si(d,X) data.

where KE_{beam}, $KE_{ejectile}$ and KE_{recoil} are the total kinetic energy of the beam, ejectile and recoil nucleus, respectively. The parameter E_{loss} represents the energy lost by the particle through the detector (and/or the aluminium foil) and Q_{value} is the Q-value of the nuclear reaction. Such a plot, where particle energies have been transformed to excitation energies of the residual nucleus ^{181}Ta, is shown in figure 4.6.

4.3 Calibration of the CACTUS array

By gating on the proton banana shaped curve, unwanted reactions together with some background events were eliminated and mostly events from the ^{28}Si(d,p)^{29}Si reaction were isolated. Following the same procedure in section 4.2, the measured proton energies were transformed into excitation energy of ^{29}Si to construct an excitation energy spectrum of ^{29}Si (see figure 4.7).

The proton excitation spectra of ^{29}Si were used to gate on the $E_x = 4934$ keV state (see figure 4.7), and the corresponding γ-ray spectra were extracted for all 26 NaI(Tl) detectors. Two well distinguished γ-ray peaks corresponding to the 1273 keV and 4934 keV γ-ray transitions in

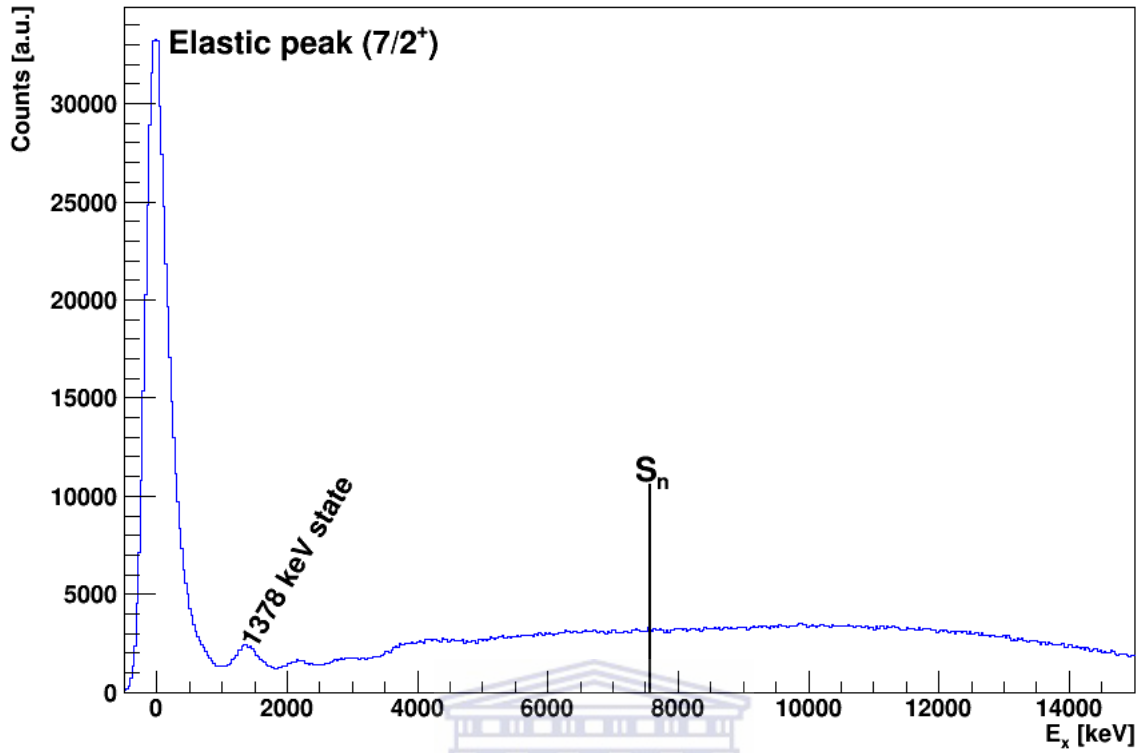

Figure 4.6. The ^{3}He excitation energy spectrum, without γ-ray coincidence requirement, for ^{181}Ta. S_n indicates the location of neutron separation energy.

UNIVERSITY of the
WESTERN CAPE

^{29}Si are visible. These γ-ray transitions were then used to linearly calibrate the γ-ray spectra for each NaI(Tl) detector. The deuteron gate from ^{28}Si(d,d')^{28}Si reaction does not yield well distinguished γ-ray transitions. Figure 4.8 shows the calibrated γ-ray spectrum of one NaI(Tl) detector. In addition, a resulting single escape peak at 4422 keV from pair production is also observed in the γ-ray spectra.

4.4 Time calibration

The detection of coincident events between particles and γ rays is accomplished through the SiRi array, which provide the TDC start signal, and the CACTUS array which provide the TDC stop signal. The rise times of the recorded signals cross the LED threshold at different times depending on the signal amplitude. High-energy events have higher signal amplitude compared to low-energy events. As a result high-energy signals will cross the discriminator threshold before the low-energy signals. This leads to the *"walk"* effect, which is the timing difference that depends on the amplitude of the signal, with the implication that high- and low-

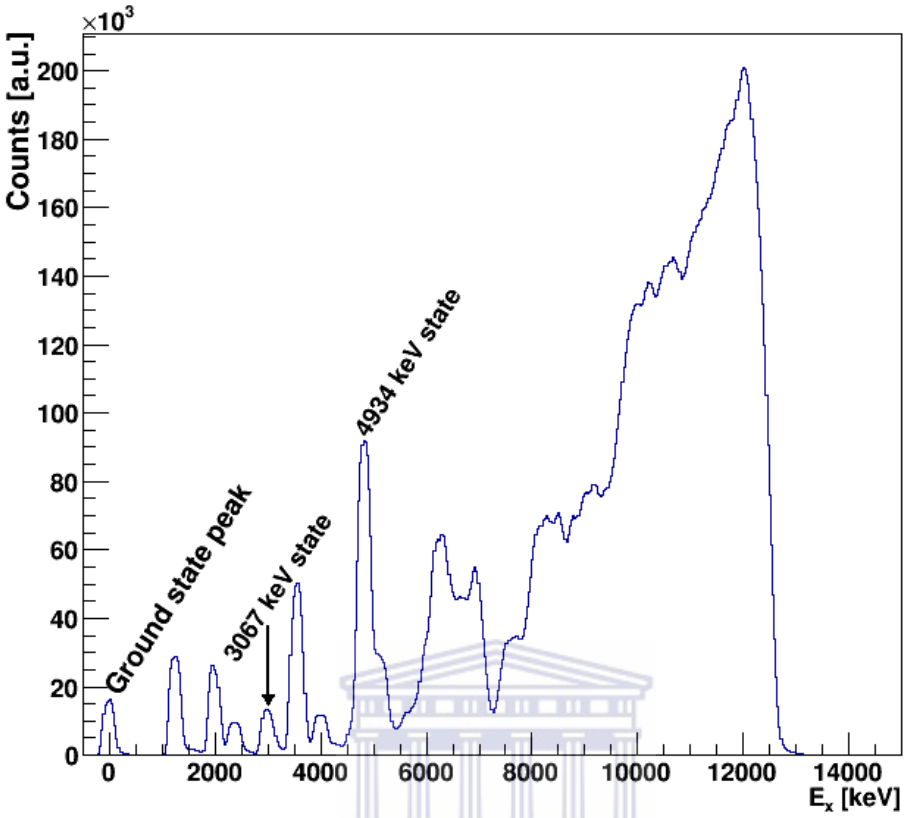

UNIVERSITY of the WESTERN CAPE

Figure 4.7. The proton excitation energy spectrum, without γ-ray coincidence requirement, for ^{29}Si.

energy events with identical time of occurrence will be effectively detected at different times. The *walk* effect makes it difficult to obtain accurate timing information. A clear illustration is given by the energy-time matrix gated on the ^{181}Ta(^{3}He,^{3}He'γ)^{181}Ta reaction channel in figure 4.9, where the signals exhibits a curvature which increases with decreasing γ-ray energies. A similar energy-time matrix was obtained for ^{181}Ta(^{3}He,$\alpha\gamma$)^{180}Ta reaction (see figure 6.2 in the appendix).

The *walk* effect can be counterbalanced by fitting a function of the form

$$t(x) = a + \frac{b}{x + c} + dx + 200 \tag{4.4}$$

to the energy-time matrix to obtain the coefficients a, b, c and d, where $t(x)$ and x are channels corresponding to the detected time signal and γ-ray energy, respectively. These coefficients are then used to correct for the timing difference due to *walk*. The time peaks of all individual channels are aligned, and the prompt peaks fixed at channel $\approx$ 200 which is represented by the

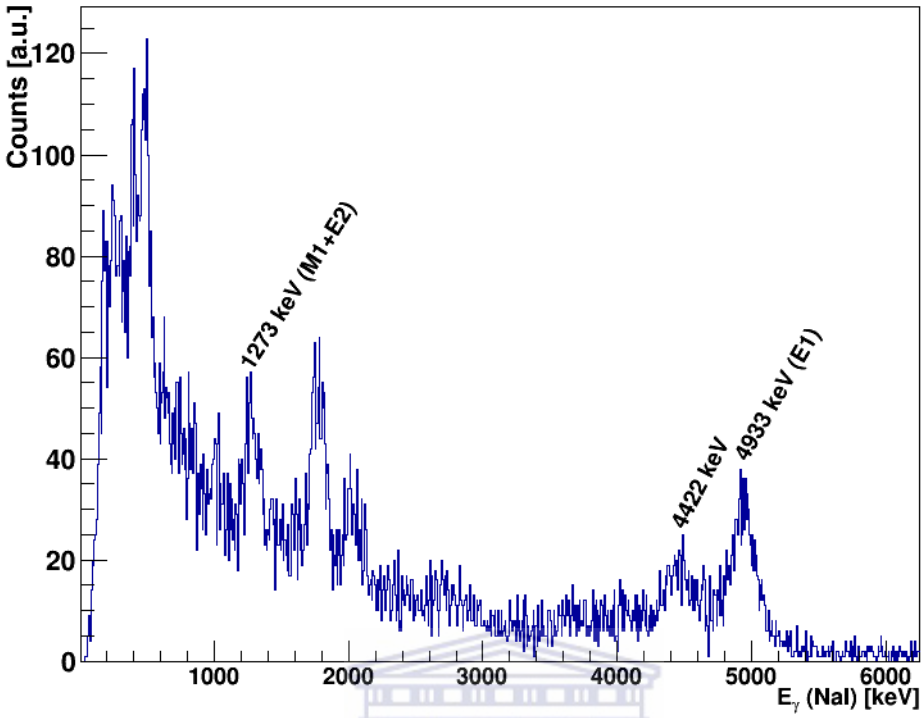

Figure 4.8. The calibrated γ-ray energy spectrum of ^{29}Si obtained with the E_x gate on the 4934 keV state for one NaI(TI) detector in the CACTUS array.

UNIVERSITY of the
WESTERN CAPE

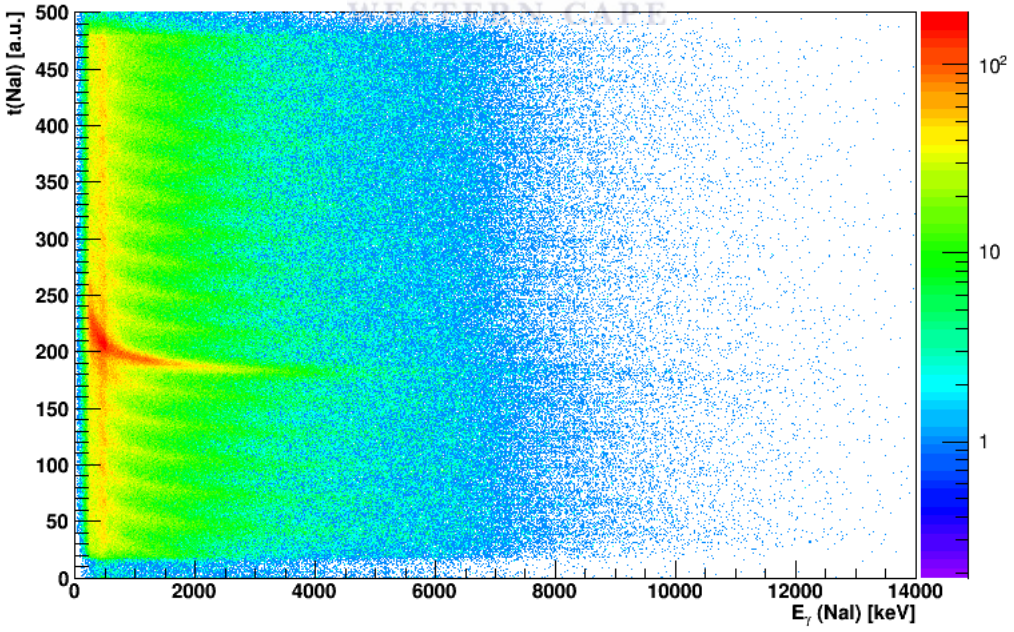

Figure 4.9. The energy-time matrix for the ^{181}Ta(^{3}He,^{3}He'γ)^{181}Ta reaction of the CACTUS array.

offset value of equation (4.4). The true coincidence events are detected within a narrow time window t_2 - $t_1 \approx 40$ ns.

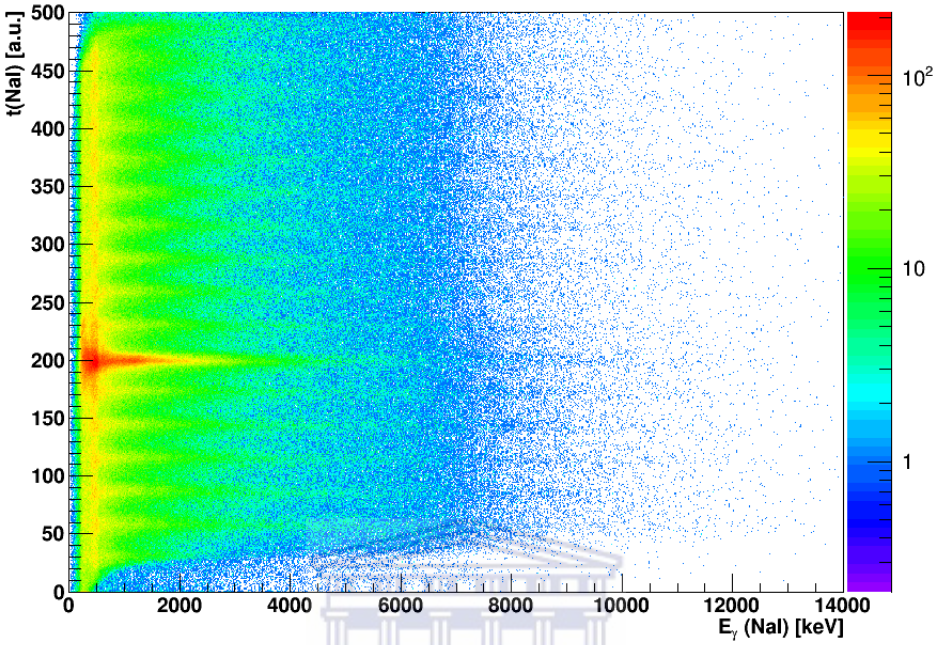

Figure 4.10. The energy-time matrix from the ^{180}Ta(^{3}He,^{3}He'γ)^{181}Ta reaction after *walk* correction for the CACTUS array.

UNIVERSITY of the
WESTERN CAPE

Figure 4.10 shows the energy-time matrix for ^{181}Ta(^{3}He,^{3}He'γ)^{181}Ta reaction, after the *walk* correction. The corresponding projected time spectrum for ^{181}Ta is shown in figure 4.11, with gates on the prompt time peak (t_1,t_2) and the background random events (t_3,t_4). Random events were subtracted from the prompt events, to obtain the true number of coincidences. A similar *walk* corrected energy-time matrix and its corresponding time spectrum were also obtained for the ^{181}Ta(^{3}He,$\alpha\gamma$)^{180}Ta reaction (see figure 6.3 and 6.4 in the appendix A). The energy-time matrices for the silicon particle telescopes were obtained using the same *walk* correction method as discussed above.

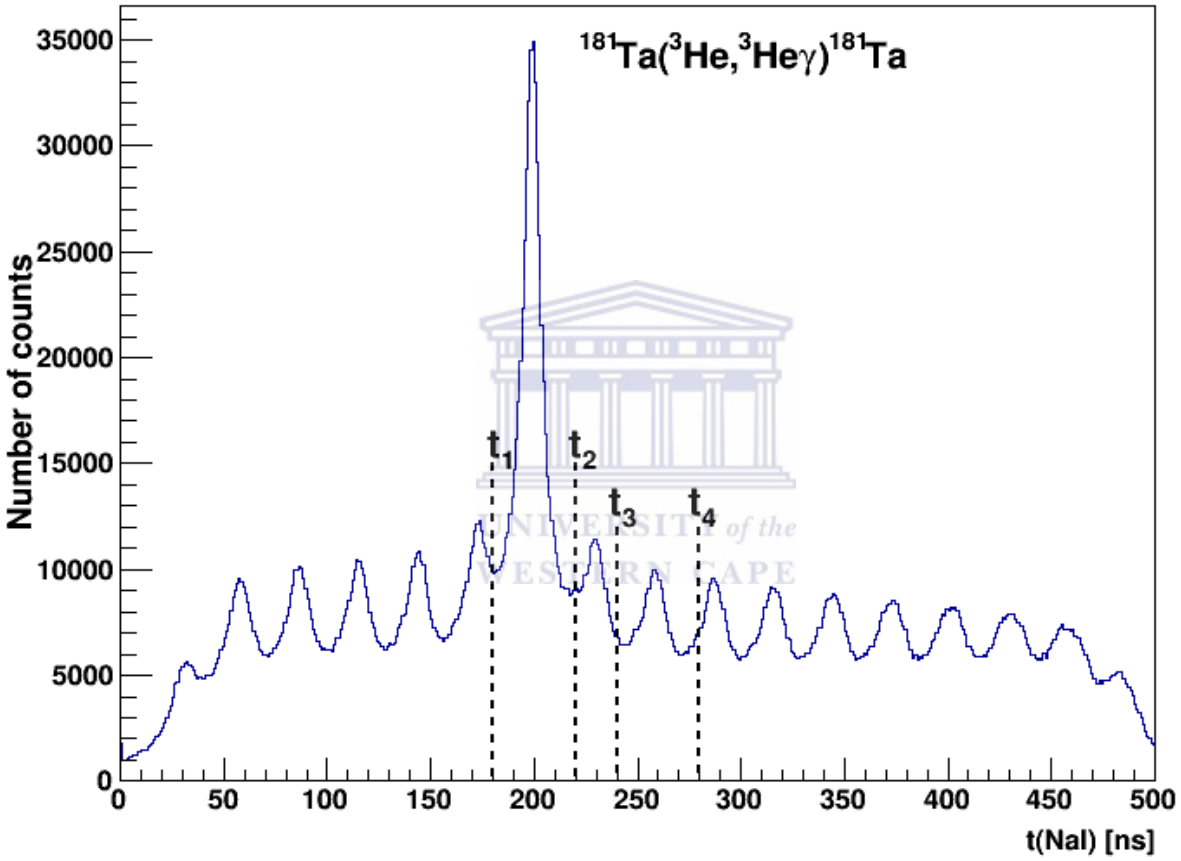

Figure 4.11. The projection of figure 4.10 on the time-axis after signals were time calibrated from CACTUS. The dashed lines (t_1,t_2) and (t_3,t_4) are gates on the prompt and random events, respectively, with same width.

4.5 Particle γ-ray coincidence matrices

From the particle-identification technique, which makes it possible to gate on either ^{3}He or α particles, together with the corresponding gates on the time spectra (see figure 4.11 for ^{181}Ta), the ^{3}He-γ or α-γ coincidence events were extracted. From these coincidence events, matrices were constructed where the excitation energy E_x of the isotope of interest is plotted against the energy of γ ray E_γ. A plot of such a matrix for ^{181}Ta(^{3}He,^{3}He'γ)^{181}Ta is displayed in figure 4.12, with characteristic features such as the E_x=E_γ diagonal and a drop in counts at $\approx S_n$. The 45° diagonal border, where the particle excitation energy E_x equals the γ-ray energy E_γ, shows that only γ rays with energy equal to or less than that of a specific state can be emitted from that state. A drastic drop of counts in excitation energy is observed at $E_x \approx S_n$ (see figure 4.13), this is the region where there is a high probability for a nucleus to emit a particle rather than a γ ray. When a particle is emitted the nucleus A-1 is populated, assuming p or n emission. These obvious features in the matrices further confirm good calibration of both the SiRi and CACTUS arrays.

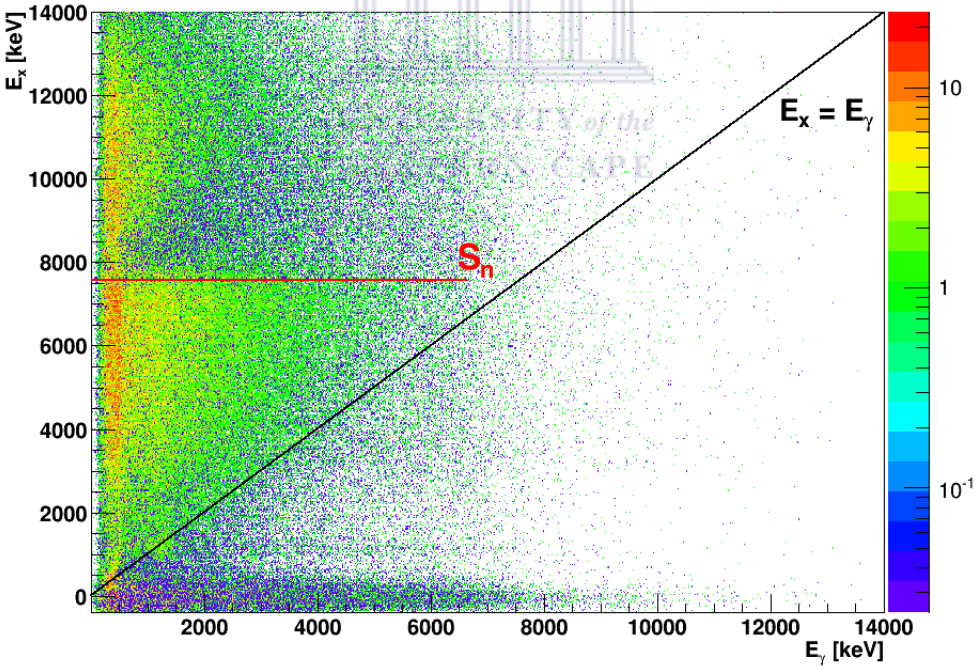

Figure 4.12. The E_x vs E_γ matrix of ^{181}Ta. The horizontal line indicates the neutron separation energy, S_n.

The two visible energy levels in figure 4.13 could not be clearly identified due to the resolution of the SiRi array. Since there is no ^{181}Ta(^{3}He,^{3}He'γ) measurements available in the National Nuclear Data Center (NNDC) [63], the two observed states can be associated with the 482 and

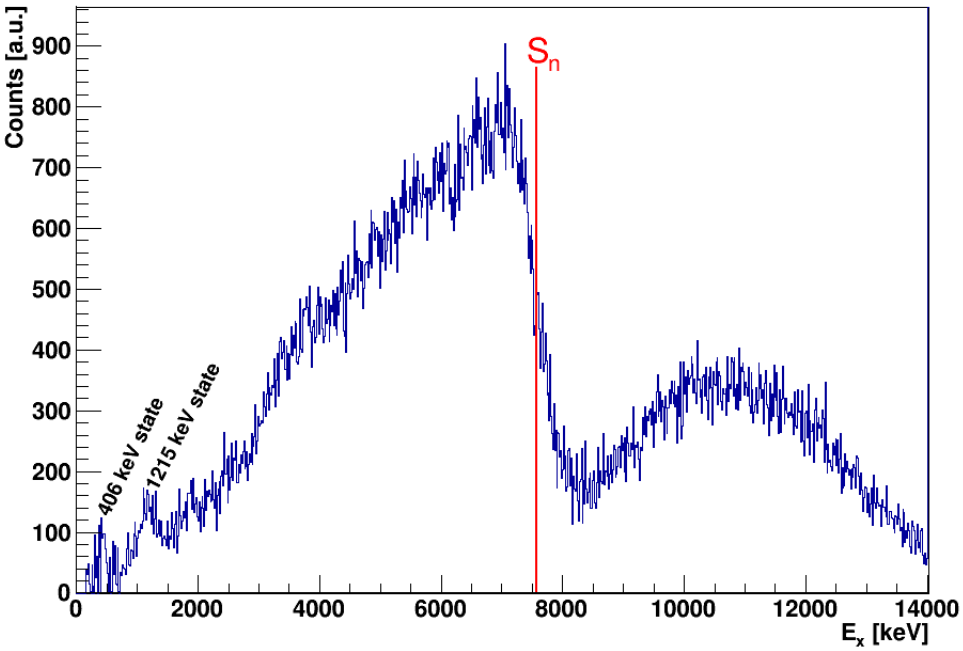

Figure 4.13. The projection of E_x vs E_γ matrix on E_x, the vertical line indicates S_n.

1230 keV states observed in (n,n') [70] and (d,d') [71] measurements respectively.

UNIVERSITY of the
WESTERN CAPE

4.6 Primary γ-ray matrices

The primary γ-ray matrix can be extracted from the full-energy γ-ray spectra for each excitation energy bin. To obtain full-energy γ-ray spectra, the raw γ-ray spectra were unfolded using the unfolding iterative procedure and then corrected for the known response functions of the CACTUS array [57], see section 2.2.1. Thus these γ-ray spectra for each excitation energy bin are corrected for the single- and double-escape peak, the annihilation peak, the Compton contributions, and the detector efficiency. Figure 4.14 shows the unfolded γ-ray spectra for ^{181}Ta. The primary γ-ray matrices were constructed from the unfolded γ-ray spectra, using the first-generation method [58], see section 2.2.3. The resulting experimental first generation γ-ray matrix of ^{181}Ta is shown in figure 4.15. The two regions that correspond to E_γ=400 and 1300 keV are dominated by low statistics due to over-subtraction of discrete and strong γ-ray transitions during the generation of primary γ-ray matrix. Both nuclei under study had low statistics[2]. The NLD and γSF of ^{181}Ta and ^{180}Ta were extracted simultaneously from these

[2]The events that were considered for extraction of the experimental first generation γ-ray matrix for ^{181}Ta and ^{180}Ta are $2.00\times10^{+05}$ and $3.89\times10^{+03}$, respectively.

matrices through the iterative procedure.

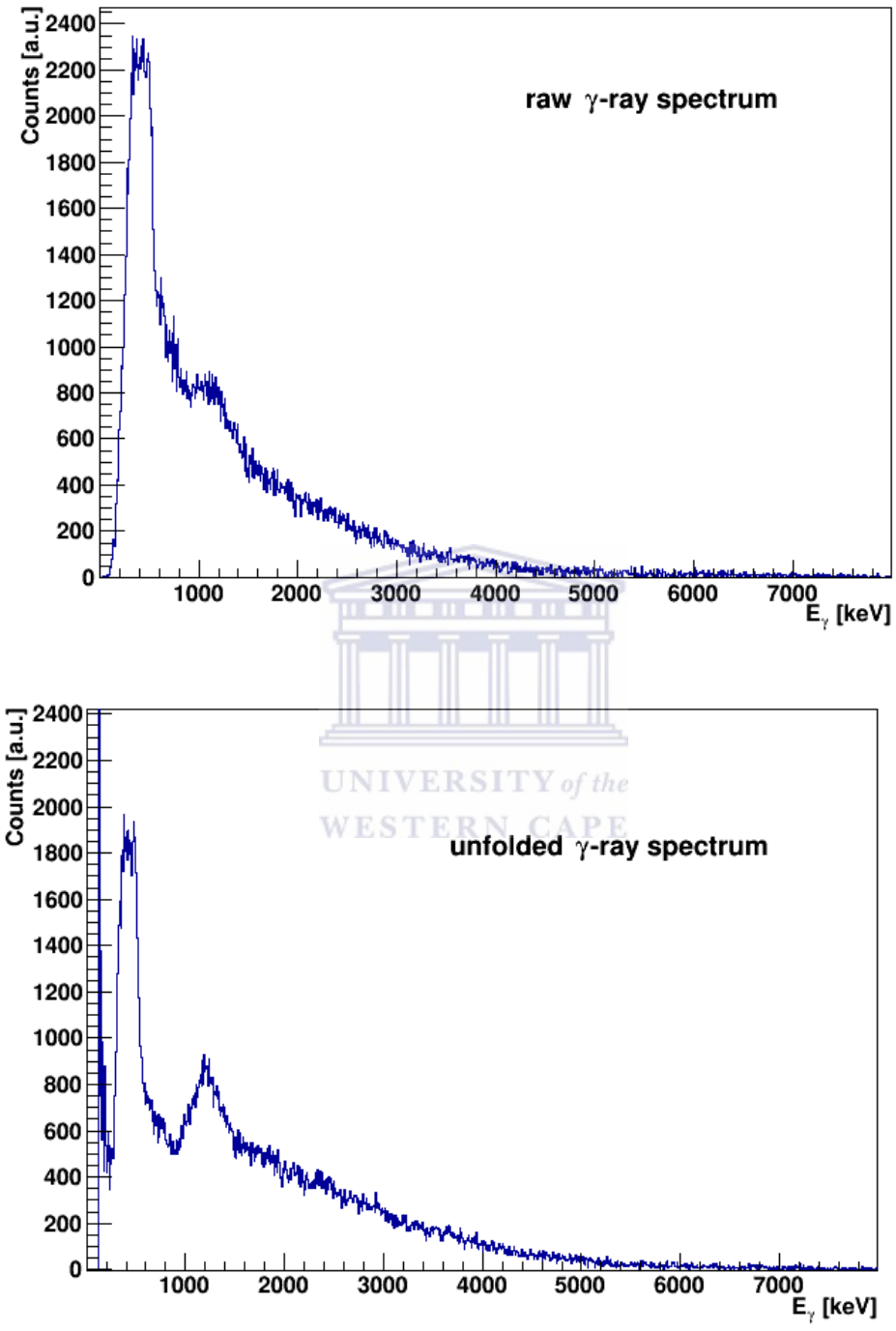

UNIVERSITY of the
WESTERN CAPE

Figure 4.14. The raw (top panel) and unfolded (bottom panel) γ-ray spectra for ^{181}Ta corresponding to $E_x \leq 7.6$ MeV.

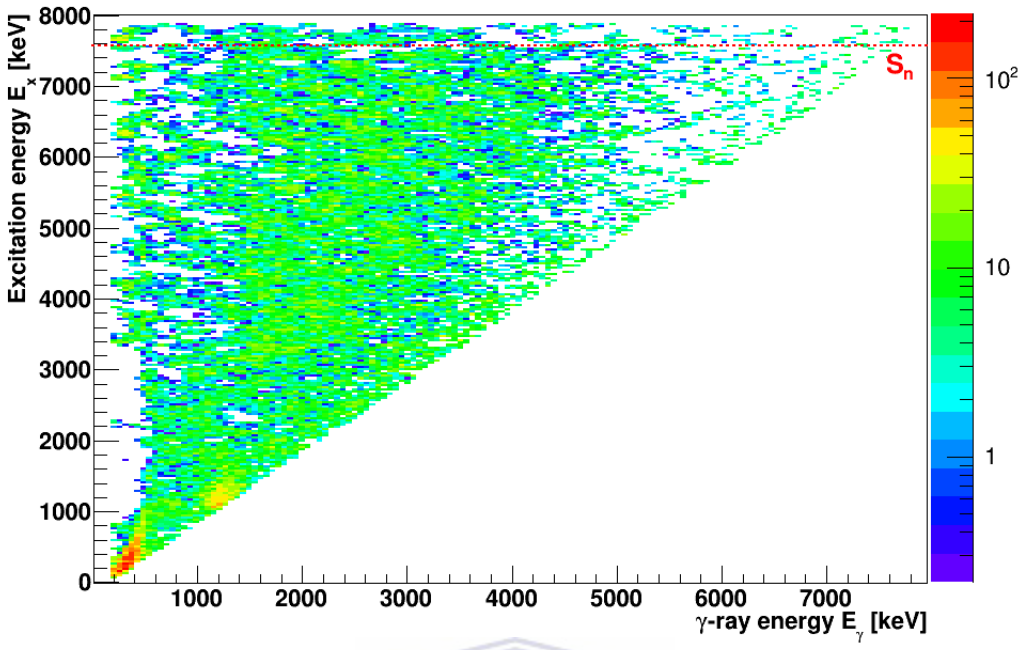

Figure 4.15. The experimental first generation γ-ray matrix for ^{181}Ta.

UNIVERSITY of the
WESTERN CAPE

4.7 Extraction of nuclear level density and γ-ray strength function

From the first generation γ-ray spectra, the NLD and the γSF were determined using the iterative procedure [55] on the first-generation matrix. The theoretical calculated first generation γ-ray matrix $P_{th}(E_x, E_\gamma)$ was fitted to the experimental first generation γ-ray matrix $P(E_x, E_\gamma)$ by performing a χ^2 minimization. A global χ^2 minimum was achieved through the iterative procedure in the energy regions of $E_\gamma > 1634$ keV and 2569 keV $\leq E_x \leq$ 7376 keV for ^{181}Ta, and $E_\gamma > 1734$ keV and 2969 keV $\leq E_x \leq$ 6348 keV for ^{180}Ta.

The limits (E_x^{min}, E_x^{max}, and E_γ^{min}) are chosen to ensure that the spectra are dominated by transitions from compound states E_x^{min}, that the statistics is not too low E_x^{max}, and to exclude possible contributions of e.g. yrast transitions which might have not been correctly subtracted in the first-generation method E_γ^{min} (see Refs. [55, 56]). Figure 4.16 shows the experimental matrix $P(E_x, E_\gamma)$ and fitted matrix $P_{th}(E_x, E_\gamma)$, displaying a chosen set of limits (E_x^{min}, E_x^{max}, and E_γ^{min}) for ^{181}Ta. Note that both the $P(E_x, E_\gamma)$ and $P_{th}(E_x, E_\gamma)$ look very similar confirming the quality of the procedures as applied to both nuclei.

From the E_x vs E_γ matrix (e.g. see figure 4.16 for ^{181}Ta), the γSF $f(E_\gamma)$ and the NLD $\rho(E_x)$

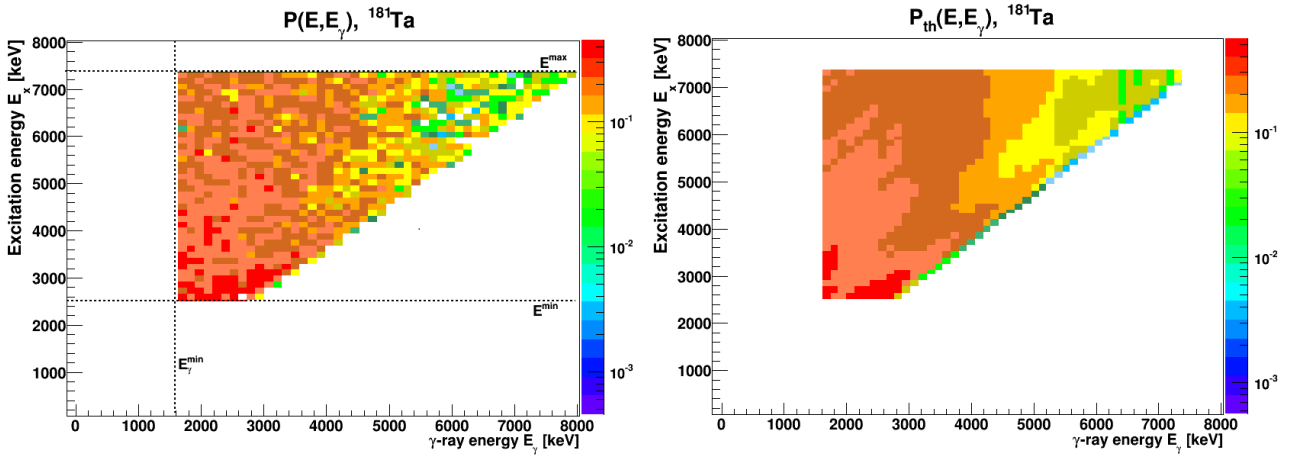

Figure 4.16. The fitted region of the experimental first-generation matrix $P(E_x, E_\gamma)$ (left) and the corresponding theoretical first-generation matrix $P_{th}(E_x, E_\gamma)$ (right) of ^{181}Ta, showing good agreement.

were extracted for both Ta isotopes and are shown in figures 4.17 and 4.18, respectively. The experimental $\rho(E_x)$s (black solid squares) are normalized to known discrete states taken from Ref [63] (black solid line) at low excitation energies at the location of the vertical arrows. At high energies, the $\rho(E_x)$s were interpolated to the total level density at the neutron separation energy $\rho(S_n)$ (black open square) using the Constant Temperature (CT) model [17] (black dotted line) (see section 2.1.1.2).

UNIVERSITY of the
WESTERN CAPE

The total level density at S_n was estimated from the s-wave average neutron resonance spacing $D_{l=0}$ and the spin cut-off parameter σ^2 calculated from the back-shifted Fermi gas (BSFG) model (see Table 4.1). The D_0 used in the case of ^{181}Ta was an average of the level spacings taken from Refs. [22, 72]. The propagation of the uncertainties was also carefully considered. The normalization of the γ-ray transmission coefficient $\mathcal{T}(E_\gamma)$ was performed, by determining the absolute parameter B (see Eq. 2.41), using the experimental values of the average radiative width $\langle\Gamma_\gamma\rangle$ at S_n taken from Refs [22, 72], and the s-wave average neutron resonance spacing. For ^{181}Ta experimental level density, the normalization value $\rho(S_n) = 1.46 \pm 0.28 \times 10^7$ MeV^{-1} was used (see Table 4.1).

In the extreme case of ^{180}Ta, neither D_0 nor $\langle\Gamma_\gamma\rangle$ experimental values are not known in the literature, because the target nuclei for neutron capture reactions (n, γ) is unstable. Therefore, using the spline fit, as implemented in the TALYS reaction code [15], the value of $\langle\Gamma_\gamma\rangle$ was estimated. Consequently, the value of $\rho(S_n)$ was estimated also by normalizing both $\rho(E_x)$ and $\mathcal{T}(E_\gamma)$ of ^{180}Ta on the basis of having the same slope as $\rho(E_x)$ and $\mathcal{T}(E_\gamma)$ of ^{181}Ta. It

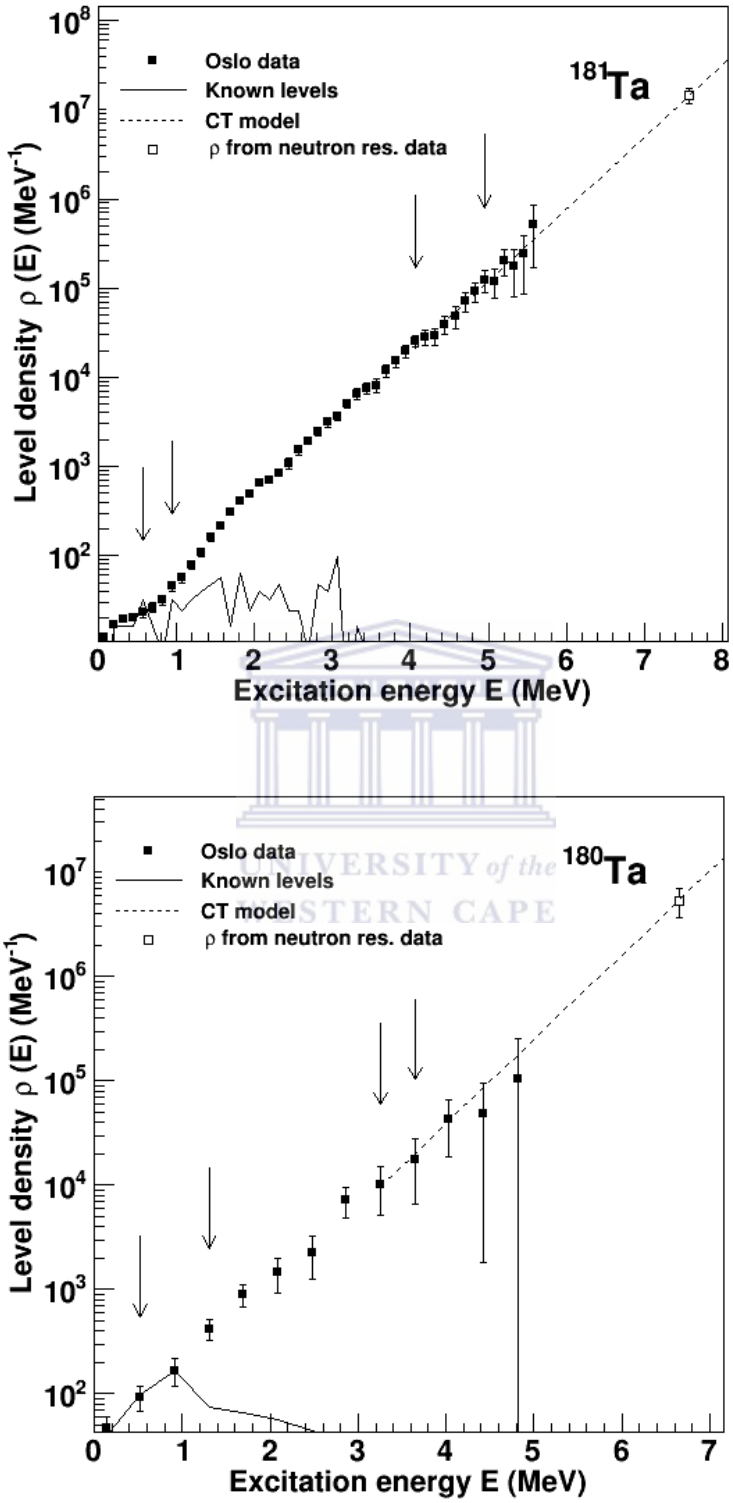

Figure 4.17. The normalized experimental NLDs for ^{181}Ta and ^{180}Ta, respectively. The set of arrows indicates the locations were the normalization of $\rho(E_x)$ was performed.

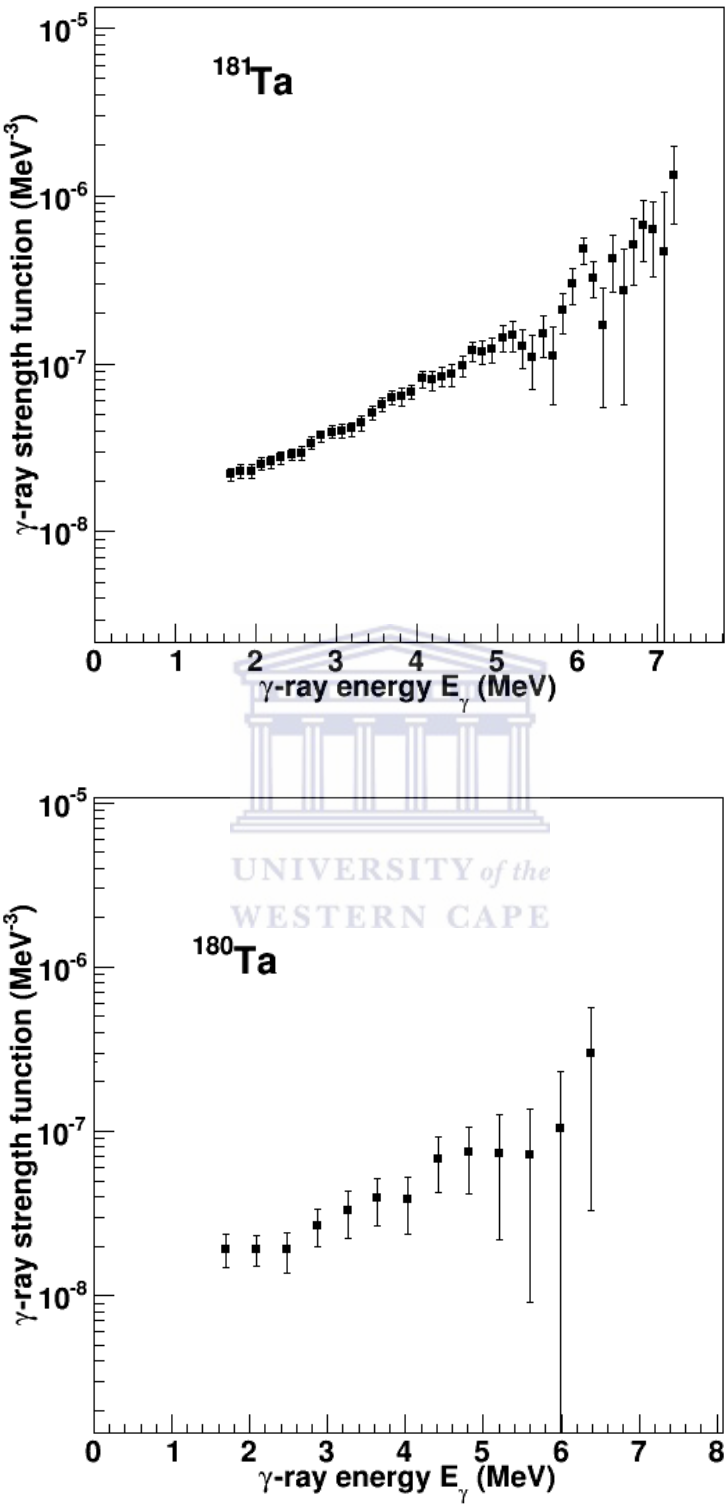

UNIVERSITY of the
WESTERN CAPE

Figure 4.18. The normalized γSF as a function of γ-ray energy, showing ^{181}Ta and ^{180}Ta strengths, respectively.

has been shown that $\rho(E_x)$ and $\mathcal{T}(E_\gamma)$ of neighboring isotopes have the same slope in various nuclei that have been studied with the Oslo method [39, 73, 74]. This is clearly demonstrated in 4.19 for ^{180,181}Ta keeping in mind that the uncertainties become very large for ^{180}Ta at $E_x > 3$ MeV, and hence the estimated value for $\rho(S_n)$ was then used to calculated D_0 for ^{180}Ta. Furthermore, the ^{180}Ta experimental data were re-binned due to limited statistics and to reduce statistical uncertainties. All parameters are summarized in Table 4.1. The extracted ^{181}Ta(^{3}He,^{3}He'γ)^{181}Ta and ^{181}Ta(^{3}He,$\alpha\gamma$)^{180}Ta γSF and NLD data, are tabulated and displayed in appendix B (see Table 6.1 and 6.2).

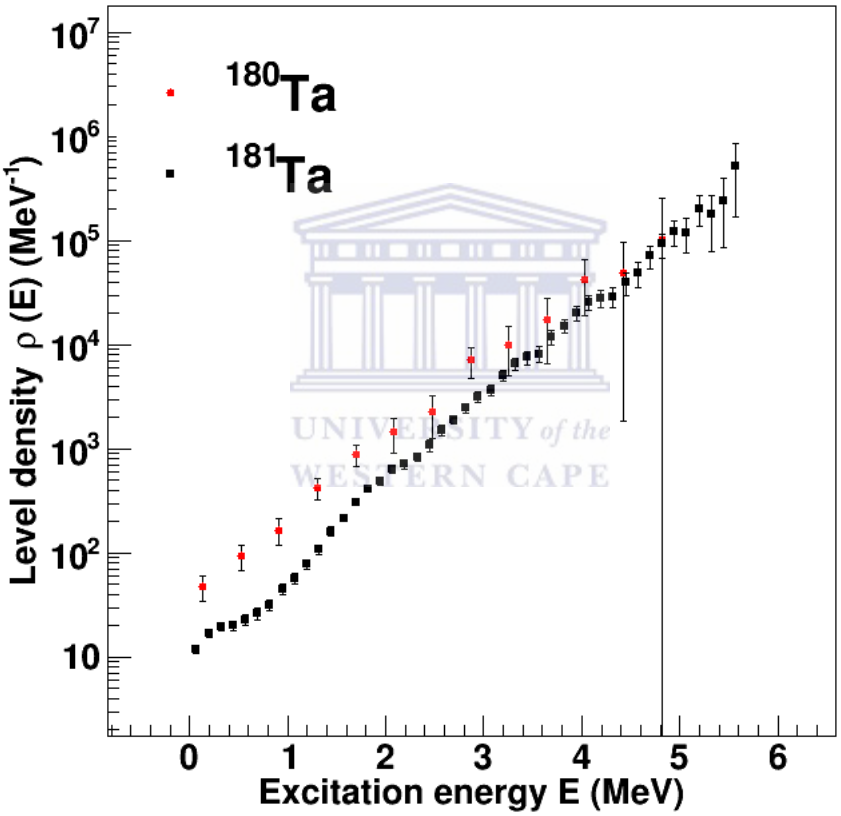

Figure 4.19. The extracted ^{180}Ta and ^{181}Ta NLDs as a function of excitation energy.

The extracted experimental γSF is compared to both the photo-neutron cross-section reactions ^{181}Ta(γ,n) from Utsunomiya *et al.* [75] and photo-absorption reactions ^{181}Ta(γ,xn) from Bergère *et al.* [76], see figure 4.20. Well understood models were applied to fit the predicted total γSF to experimental data. The enhanced generalized Lorentzian functions (EGLO), $f_{gedr1}(E_\gamma)$ and $f_{gedr2}(E_\gamma)$, are used to fit the two component of the giant electric dipole resonances, (GEDR) at $E_\gamma \approx 15.9$ MeV and $E_\gamma \approx 12.6$ MeV, respectively. The EGLO model is temperature dependent from the incorporated temperature dependence width $\langle\Gamma_\gamma\rangle$, with a constant temperature of

Table. 4.1. Input parameters for the calculation of the normalization of $\rho(E_x)$ and $\mathcal{T}(E_\gamma)$ in ^{180,181}Ta. $E1$ and T_{ct} are the Fermi-gas shift and constant temperature parameters, respectively.

Nucleus	S_n (MeV)	E1 (MeV)	T_{ct} (MeV)	σ	D_0 (eV)	$\rho(S_n)$ (10^6MeV^{-1})	$\langle\Gamma_\gamma(S_n)\rangle$ (meV)
^{180}Ta	6.65	-1.086[a]	0.537[b]	4.93±0.49[a]	1.60±0.47[c]	5.34±1.70[c]	62.0±5.77[c]
^{181}Ta	7.58	-0.370[a]	0.538[b]	4.96±0.50[a]	1.11±0.11[d]	14.58±2.76[a]	51.0±1.58[d]

[a]Calculated with the back-shifted Fermi gas model.
[b]Calculated with the constant temperature model.
[c]Estimated values (see text for details).
[d]Average value from Refs. [22, 72].

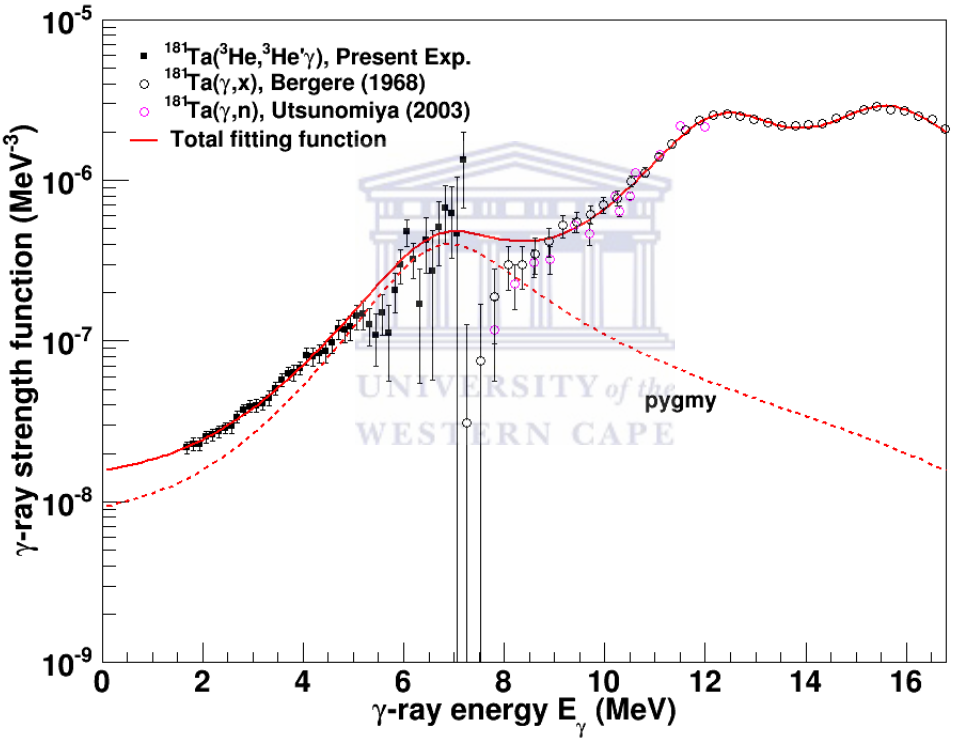

Figure 4.20. Comparison of data obtained from photonuclear cross sections with experimental γSF of ^{181}Ta.

$T_f = 0.37$ MeV. T_f is treated as a free parameter in order to allow for the best possible fit of the theoretical strength prediction at low energies. This is consistent with the Brink hypothesis assumed in the Oslo method, since T_f is constant with E_x. In addition to the GEDR, a weaker resonance was fitted using the EGLO function, f_{pyg}, (E_γ) at $E_\gamma \approx 7.0$ MeV. This resonance was recently observed [77] and associated with the E1 pygmy resonance. Therefore, total model prediction of the γSF is given by $f_{total}(E_\gamma) = f_{pyg}(E_\gamma) + f_{gedr1}(E_\gamma) + f_{gedr2}(E_\gamma)$. The fitted EGLO functions clearly reproduce the (γ,x) data together with the measured low energy data.

The parameter used to fit the total strength function to the experimental data are given in Table 4.2. For completion, the γSF for ^{180}Ta is included in figure 4.21.

Table. 4.2. Lorentzian parameters used for fitting the theoretical γSF to the experimental data, where E_0, σ_0 and Γ_0 are the energy centroid, cross-sections and widths of the resonances.

Resonance	E_0 (MeV)	Γ_0 (MeV)	σ_0 (mb)	T_f (MeV)
pygmy	7.0	3.2	34	0.37
GEDR1	12.6	3.0	330	0.37
GEDR2	15.9	3.2	440	0.37

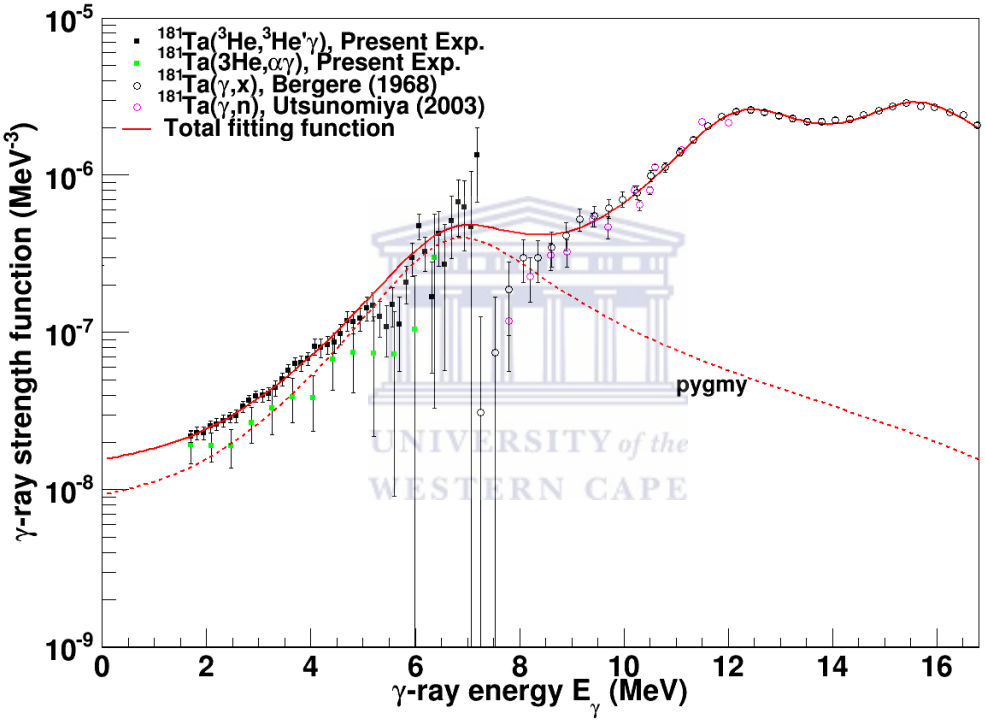

Figure 4.21. Comparison of data obtained from photonuclear cross sections with experimental γSF of ^{180,181}Ta.

Chapter 5

Discussion

5.1 γ-ray strength function and nuclear level density

The ^{180}Ta and ^{181}Ta γ-ray strength functions show no pronounced features, such as resonances, except for the observed enhancement in the strength function from 6 MeV termed "pygmy" resonance (see figure 4.20). This enhancement is positioned in a range characterized by low statistics, but from previous measurements [77] a resonance was observed in the energy range of 5 to 8 MeV and identified as the E1 pygmy resonance. The experimental photo-absorption cross section measurements (red solid circles) of ^{181}Ta(γ, γ') up to $E_x = S_n$ (and beyond from the (n, γ) reactions), are shown in figure 5.1, with the E1 pygmy resonance clearly observed. Besides the E1 pygmy resonance the ^{181}Ta γ-ray strength function is relatively featureless with no pronounced scissors resonance, and certainly no low-energy enhancement. The inclusion of only the E1 pygmy resonance predicts a good fitting function for the total γ-ray strength function (see figure 4.20).

The nuclear level density for odd-odd ^{180}Ta is higher than that of the even-odd ^{181}Ta (see figure 5.2). This is expected, due to one extra unpaired neutron in ^{180}Ta which increases the number of degrees of freedom (more details in Ref. [78]). On the other hand the experimental ^{180}Ta and ^{182}Ta [79] nuclear level densities are comparable and are equal within the uncertainties as expected. In the region around 2 MeV of the nuclear level density for ^{181}Ta, a small change in the slope is observed which can be explained as Cooper pair breaking. The excitation energy at which a nucleon pair is expected to be broken is calculated to be 1.78 MeV using the formula $\mathrm{E} = 2\Delta_0$, where $\Delta_0 = 12\mathrm{A}^{-1/2}$ is the first-order pairing phase transition, also known as pair gap parameter [19], and A is the mass of the nucleus. The discontinuity of the level densities

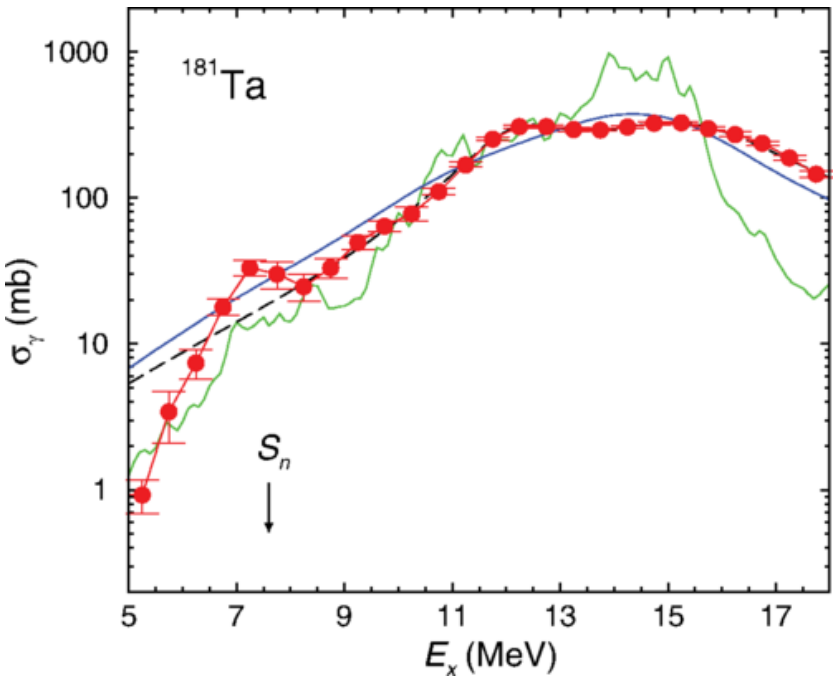

Figure 5.1. The experimental total photoabsorption cross sections (red data points) of ^{181}Ta obtained by combining (γ, γ') and (γ, n) data (see Ref. [77]).

UNIVERSITY of the WESTERN CAPE

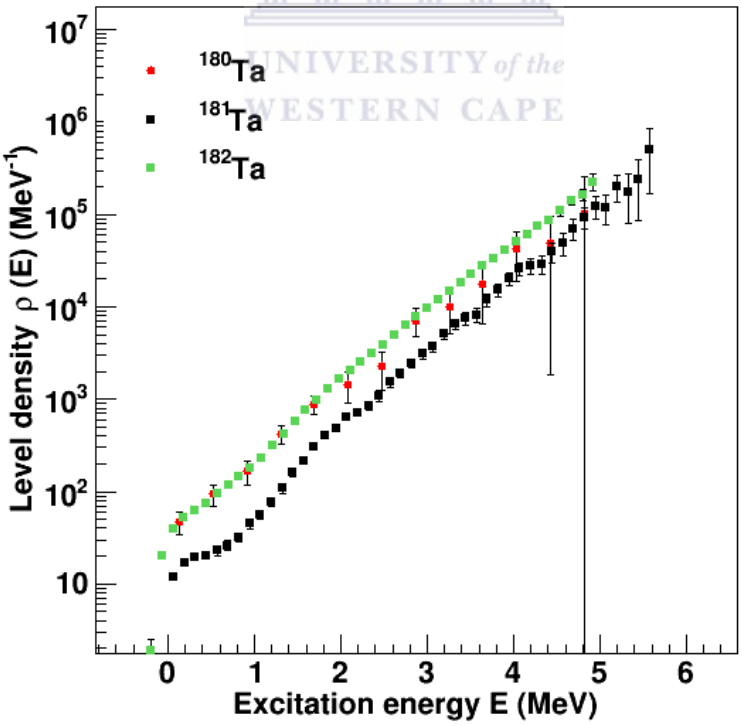

Figure 5.2. Comparison of the extracted ^{180}Ta and ^{182}Ta nuclear level densities as a function of excitation energy, data for ^{182}Ta nuclear level density are taken from Ref. [79].

at E = $2\Delta_0$ is not observed in ^{180}Ta due to the experimental data being re-binned to increase statistics in each bin, which in turn hides small changes.

5.2 Astrophysical neutron capture cross section calculations

Assuming the principle of detailed balance[1] to be valid (refer to section 2.1.5), the neutron capture cross sections and the reverse photo-neutron emission rates of astrophysical relevance, as well as the Maxwellian-averaged cross sections (MACS), were estimated for both ^{180,181}Ta isotopes. The calculations were achieved using the reaction code TALYS which includes many statistical models [15]. The measured experimental γ-ray strength functions and the nuclear level densities, which are primary ingredients for calculations of the transmission coefficient, as required by the HF approach, are now entered directly into TALYS. The ^{180,181}Ta experimental nuclear level density parameters (such as E_0, E_1, T_{ct}, a_{par}, and Pa')[2] are used to calculate the TALYS compatible nuclear level densities, which are considered in (n,γ) reaction cross section calculations. Figure 5.3 shows the TALYS level density and the experimental level density with the corresponding error bars. Excellent agreement is observed between the measured level densities and those obtained from TALYS calculations.

UNIVERSITY of the WESTERN CAPE

The uncertainties of the nuclear level densities and the γ-ray strength functions were estimated from those shown in figure 4.17 and 4.18, the ^{181}Ta data used in this case have been re-binned as well. The upper error bars of both the nuclear level densities and γ-ray strength function were obtained by replacing D_0 with D_0 - ΔD_0 and $\langle \Gamma_\gamma(S_n)\rangle$ with $\langle \Gamma_\gamma(S_n)\rangle$+$\Delta\langle \Gamma_\gamma(S_n)\rangle$, and similarly, the lower error bars are obtained by replacing D_0 with D_0 + ΔD_0 and $\langle \Gamma_\gamma(S_n)\rangle$ with $\langle \Gamma_\gamma(S_n)\rangle$ - $\Delta\langle \Gamma_\gamma(S_n)\rangle$. This modification is important since the error bars obtained using the Oslo method only provide statistical and systematic uncertainties of the unfolding and first generation methods, and do not account for the potentially significant contribution of the uncertainties of the D_0 and $\langle \Gamma_\gamma(S_n)\rangle$ parameters. The estimated error bands are shown together with the measured nuclear level density and γ-ray strength function in figure 5.4 and 5.5, respectively.

[1] The hypothesis that when a system is in equilibrium any process occurs with the same rate as the reverse process.

[2] The parameters E_0, T_{ct}, and Pa' are the energy-shift and constant nuclear temperature parameter, and the deuteron pairing energy for the spin cutoff parameter, respectively. E_1 and a_{par} are the Fermi-gas shift parameter and the level density parameter, respectively.

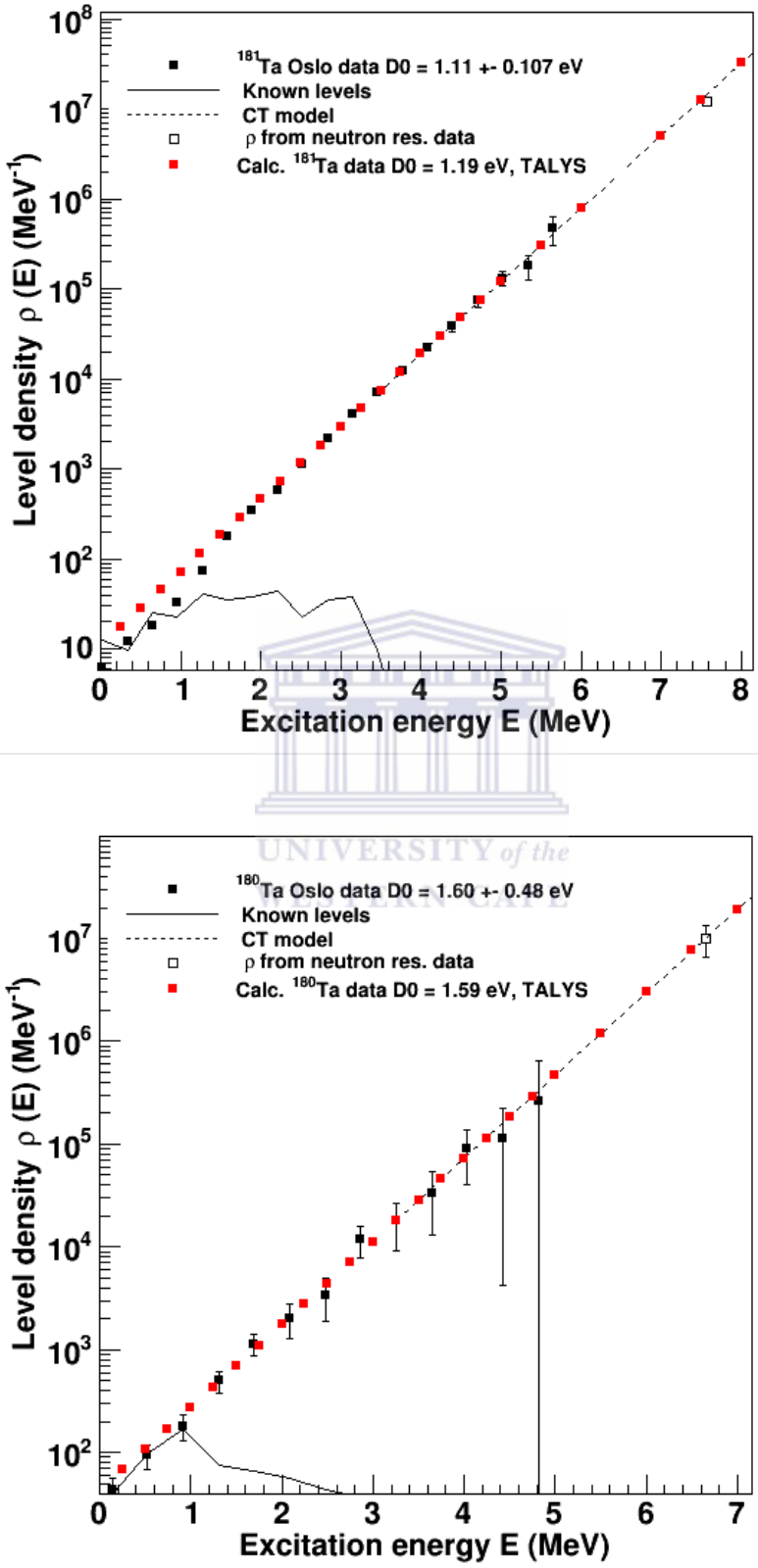

Figure 5.3. Comparison of the TALYS calculated and experimental nuclear level densities of ^{181}Ta (top) and ^{180}Ta (bottom).

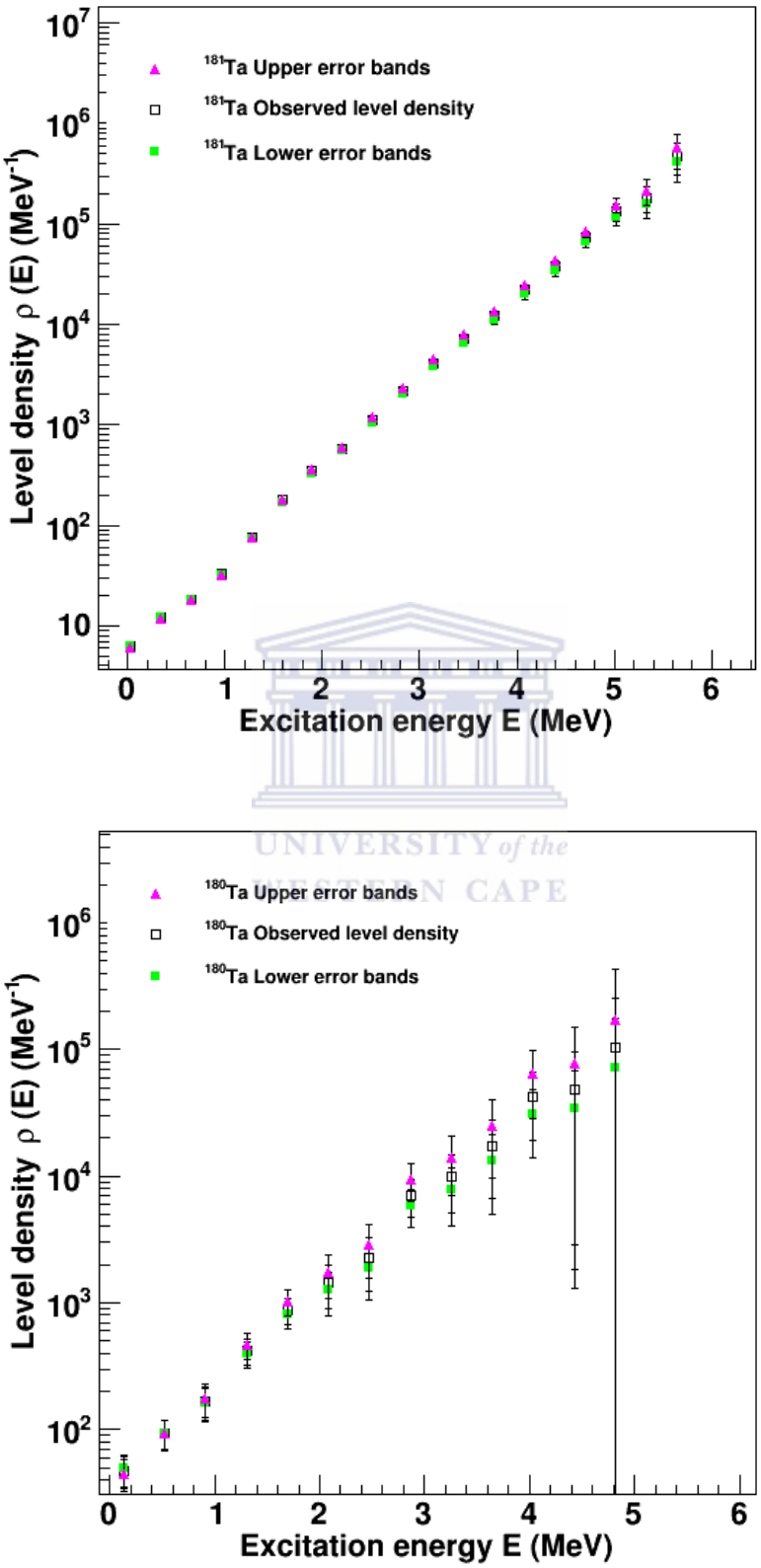

Figure 5.4. The error bands of the $\rho(E_x)$ estimated to account for the contribution of the uncertainties of D_0 parameter to the error bars, relative to the observed $\rho(E_x)$.

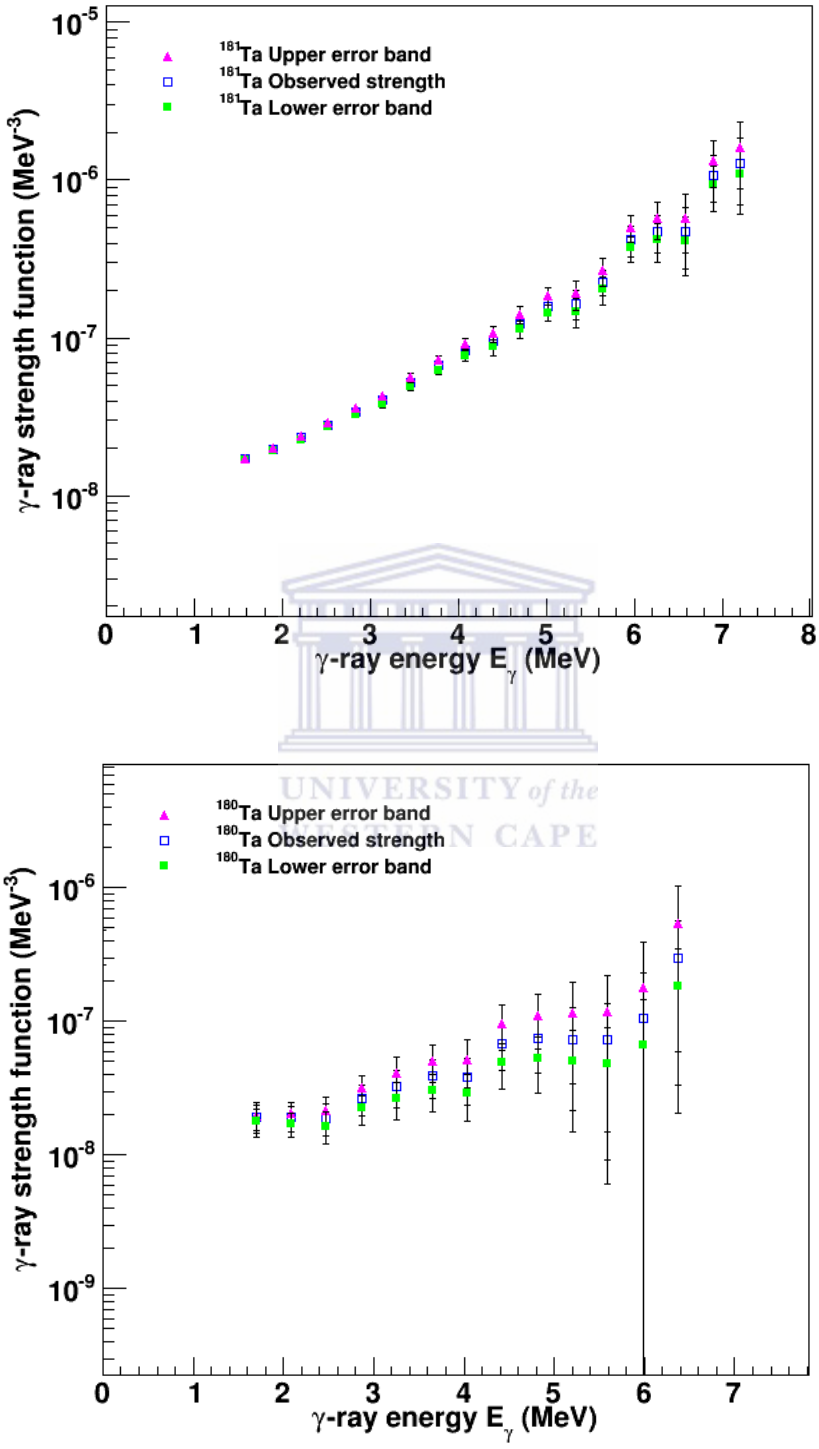

Figure 5.5. The error bands of the $f(E_\gamma)$ estimated to account for the contribution of the uncertainties of D_0 and $\langle \Gamma_\gamma(S_n) \rangle$ parameters to the error bars, relative to the observed $f(E_\gamma)$.

Figure 5.6 shows the final neutron capture cross sections, $\sigma(E_n)$, as a function of neutron energies taking into account the modified uncertainties affecting the γ-ray strength functions and the nuclear level densities (see Table 4.2). The neutron capture cross sections of ^{180m}Ta [80] determined from a time-of-flight experiment, at the Karlsruhe 3.7 MV Van de Graaff accelerator, is shown for comparison. It is observed that the ^{180}Ta(n,γ) cross sections show excellent agreement with the previously measured ^{180m}Ta(n,γ) cross sections, within the error bars, except for one data point which has high uncertainties.

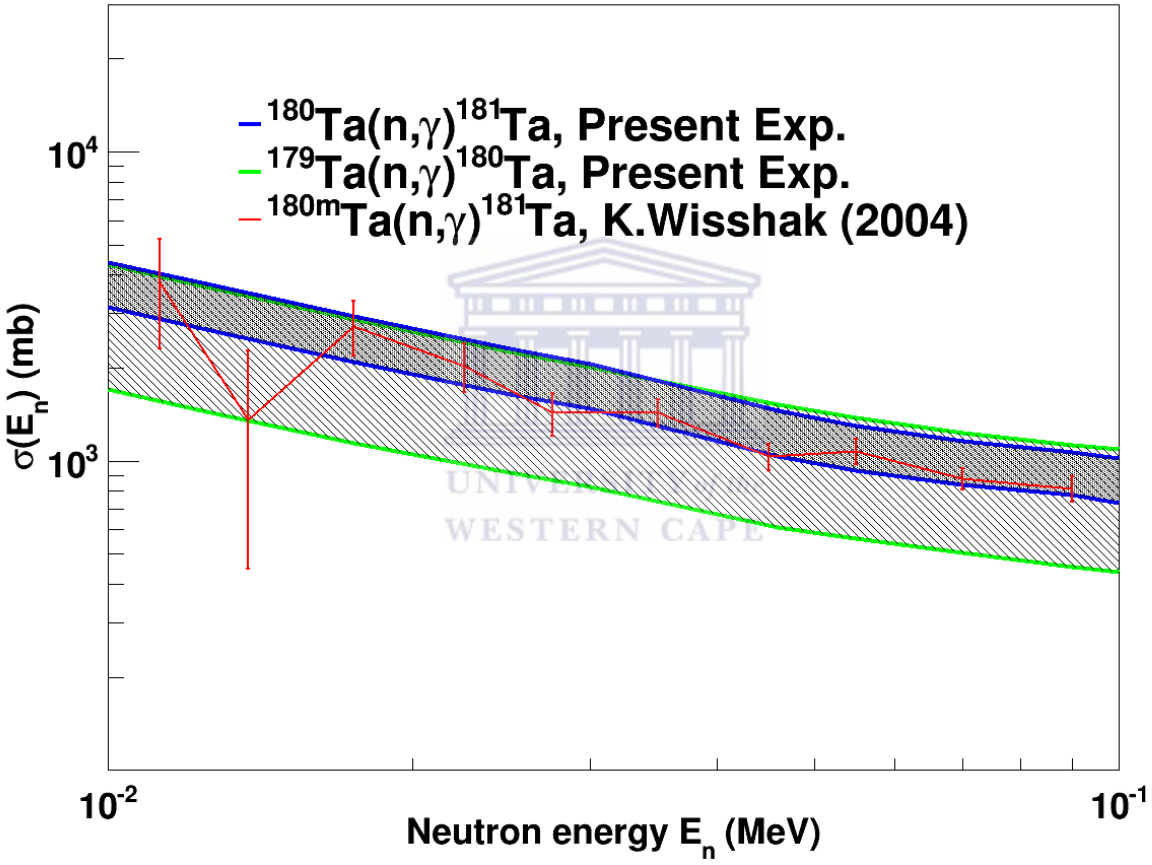

Figure 5.6. The ^{180}Ta (blue line) and ^{179}Ta (green line) neutron capture cross sections as a function of neutron energy, together with the previously measured ^{180m}Ta$(n,\gamma')^{181}$Ta cross sections [80].

Therefore, it is obvious from the excellent agreement that the use of the nuclear level density and the γ-ray strength function can reproduce the ^{180}Ta(n,γ) cross sections accurately. As such the ^{179}Ta cross sections (see figure 5.6, green line), can also be confidently considered to be a very good representation of the (n,γ) cross sections. The large errors in ^{179}Ta(n,γ) are due to the low statistics in the data from which the nuclear level density and the γ-ray strength function are extracted. This is the first (n,γ) cross sections ever obtained for ^{179}Ta

experimentally, since ^{179}Ta is highly radioactive (half-life of $\approx$ 1.83 yr) it can not be easily used to produce a target for direct measurements. Therefore, knowledge of the γ-ray strength function and nuclear level density is currently the only reliable measure from which these cross sections for nuclei with short half-lives can be obtained.

The ^{179,180}Hf(p,γ)^{180,181}Ta and ^{176,177}Lu(α,γ)^{180,181}Ta capture cross sections were also calculated and found to be several order of magnitudes lower than the ^{179,180}Ta(n,γ) cross sections at p and α energies of several MeV, respectively. This suggests that during nucleosynthesis, under typical astrophysical temperatures, neither (α,γ) nor (p,γ) reactions are responsible in any meaningful manner for the synthesis of ^{180}Ta. This is true for the reverse reactions (destruction of ^{180}Ta) through (γ,p) and (γ,α) reactions.

5.3 Nucleosynthesis of ^{180}Ta

5.3.1 The astrophysical Maxwellian-averaged (n,γ) cross sections

The astrophysical Maxwellian-averaged (n,γ) cross sections (MACS) were calculated for both ^{179}Ta(n,γ) and ^{180}Ta(n,γ) reactions, at the s- and p-process thermal energies, respectively. The results are listed in Table 5.1, where $\langle E\rangle = kT$ is the s- or p-process thermal temperature, and $\langle\sigma_\nu\rangle/v_T$ is the Maxwellian-averaged (n,γ) cross section in millibarn (10^{-27}cm^2) at the astrophysical thermal energy kT (where kT = 30 keV for $T = 0.348\times10^9$ K and kT = 215 keV for $T = 2.495\times10^9$ K), and $v_T = (2kT/m)^{1/2}$, where m is the reduced mass.

Table. 5.1. The ^{179}Ta and ^{180}Ta Maxwellian-averaged (n,γ) cross sections at thermal energy kT.

Isotope	$\langle E\rangle$ (keV)	$\langle\sigma_\nu\rangle/v_T$ (mb)
^{179}Ta(n,γ)	30	$1454\ ^{+735}_{-569}$
	215	$423\ ^{+278}_{-191}$
^{180}Ta(n,γ)	30	$2035\ ^{+342}_{-356}$
	215	$583\ ^{+132}_{-129}$

5.3.2 *p*-process

If the *p*-process is considered as the major contribution to the synthesis of ^{180}Ta, the experimentally calculated MACS, at *p*-process thermal energy $kT = 215$ keV, corresponding to ^{181}Ta(γ,n) reaction rates are about 27% larger than the destructive ^{180}Ta(γ,n) reaction rates, on the basis of the principle of detailed balance. From this simple picture it can be deduced that *p*-process predicts that the production rate of ^{180}Ta is larger than the destructive rate in explosive environments. These results are consistent with the previous work, that the *p*-process can explain fully [9], or at least partially explain [11] the galactic production of ^{180}Ta.

5.3.3 *s*-process

At the *s*-process thermal energy $kT = 30$ keV, the MACS of 1454 $^{+735}_{-569}$ mb and 2035 $^{+342}_{-356}$ mb agree within the uncertainties with the recommended values of 1334±422 mb and 1640±260 mb derived in Ref. [81] for ^{179}Ta and ^{180}Ta, respectively. However, the calculated ^{180}Ta MACS, corresponding to ^{180}Ta(n,γ) reaction rates are 29% smaller than the ^{179}Ta(n,γ) reaction rates. The possible *s*-process production of ^{180}Ta occurs mostly via beta-decay branching from an excited state in ^{179}Hf according to Ref. [10]. To fully investigate the *s*-process production of ^{180}Ta, relevant cross sections of neighboring nuclei need to be investigated as well. It is therefore desirable to measure ^{178}Hf(n,γ)^{179}Hf(β^-)^{179}Ta and/or ^{179}Hf(n,γ)$^{180^m}$Hf(β^-)^{180}Ta cross sections in future work, to fully understand the analysis of ^{180}Ta synthesis through the *s*-process.

UNIVERSITY of the WESTERN CAPE

5.3.4 Future outlook

It has been pointed out that ^{180}Hf(υ_e, e)^{180}Ta, *p*-process and ^{181}Ta($\upsilon, \upsilon' n$)^{180}Ta contribute 50, 25 and 25% to the synthesis of ^{180}Ta, respectively [11], a scenario that may be quite likely. Many more measurements in and around the Ta isotopic chain need to be conducted, to establish a solid understanding of the interplay of various astrophysical processes for the production of Ta. In particular, the γ-ray strength function and nuclear level density need to be determined for $^{180-182}$W and $^{177-181}$Hf isotopes. In fact, ideally all nuclei should be measured since the large network calculations is an interplay of thousands of cross sections. For measured Ta results, network calculations are beyond the scope of this thesis. The newly deduced ^{179}Ta(n,γ) and ^{180}Ta(n,γ) cross sections can be utilized in astrophysical network calculations to investigate and constrain the galactic production mechanism of ^{180}Ta.

Chapter 6

Summary and Conclusions

The origin of ^{180}Ta, nature's rarest isotope with its abundance based on a naturally occurring isomer, has remained a puzzle over the years. No consensus exists, and several processes, such as the s- and p-process, have been proposed to exclusively synthesize ^{180}Ta in the Universe. Furthermore, it has been pointed out that a combination of the above processes together with the υ-process can also be responsible for the production of ^{180}Ta. Clearly, many astrophysical processes can theoretically be used to explain the synthesis of ^{180}Ta. The uncertainties in the reaction rates for ^{180,181}Ta exist partly due to the unavailability of experimental nuclear level density and γ-ray strength function data, which are critical ingredients for the Hauser-Feshbach statistical emission model from which astrophysical reaction rates are calculated.

UNIVERSITY of the
WESTERN CAPE

An experiment was successfully performed at the Oslo Cyclotron Laboratory using the (^{3}He,^{3}He'γ) and (^{3}He,$\alpha\gamma$) reactions to obtain particle-γ data, from which the nuclear level densities and γ-ray strength functions were extracted for the first time below S_n for ^{180}Ta, and below 6 MeV excitation energy for ^{181}Ta. These average statistical parameters were extracted from the particle-γ coincidence events utilizing the analytical procedure called the Oslo Method. The charged particles were detected using the SiRi array, while the γ rays were detected using the CACTUS array. The ^{179}Ta(n,γ) and ^{180}Ta(n,γ) cross sections were obtained from the experimental γSF and NLD calculated within the constant temperature (CT) model, that show excellent agreement with experimental results, as implemented in the TALYS reaction code. Further, the astrophysical Maxwellian-averaged (n,γ) cross sections (MACS) have been calculated at s- and p-process temperatures, for ^{180,181}Ta. The calculated MACS of 1454 $^{+735}_{-569}$ mb and 2035 $^{+342}_{-356}$ mb at the p-process temperature, imply that the p-process produces more ^{180}Ta than it destroys. Future measurements of the γ-ray strength function and nuclear level density are

essential to obtain (n,γ) cross sections to probe the importance or irrelevance of the individual processes in the synthesis of ^{180}Ta. Henceforth, the astrophysical network calculations can be performed to investigate the galactic production mechanism of ^{180}Ta from various processes and various astrophysical sites.

UNIVERSITY of the
WESTERN CAPE

Bibliography

[1] Connecting Quarks with the Cosmos: Eleven Science Questions for the New Century, The National Academic Press, 2003.

[2] S. Rosswog *et al.*, Nature 500, 535 (2013).

[3] A. Arcones and F. K. Thielemann, J. Phys. G: Nucl. Part. Phys. 40, 013201 (2013).

[4] B. V. Kheswa *et al.*, Phys. Lett. B. **744**, 268 (2015).

[5] I. J. Thompson and F. M. Nunes, *Nuclear Reactions for Astrophysics*, (Cambridge University Press, 2009).

[6] C. Sneden, J.J. Cowan, and R. Gallino, Annual Review of Astronomy and Astrophysics 46, 241 (2008).

[7] Report of the Nucl. Phys. and Related Computing Science R&D for Advanced Fuel Cycles, DOE Offices of Nuclear Physics and Advanced Scientific Computing Research, 2006.

[8] Japanese Atomic Energy Agency R&D Review, *Supernova Neutrino-Process Nucleosynthesis*, (2010).

[9] M. Rayet *et al.*, A & A **298**, 517 (1995).

[10] M. Loewe *et al.*, Nucl. Phys. A. **719**, 275c (2003).

[11] A. Heger *et al.*, Phys. Lett. B **606**, 258 (2005).

[12] A. Byelikov *et al.*, Phys. Rev. Lett. **98**, 082501 (2007).

[13] T. Hayakawa, *Neutrino-process in supernovae*, NDM15 conference, Finland, (2015).

[14] S. Goriely *et al.*, A&A J. **375**, L35 (2001).

UNIVERSITY of the WESTERN CAPE

[15] A. J. Koning *et al.*, *Nuclear Data for Science and Technology* (EDP Sciences; eds O. Bersillon *et al.*), p. 211 (2008) (see also *http://www.talys.eu*)

[16] M. Guttormsen *et al.*, Eur. Phys. J. A **51** (12), 170 (2015).

[17] A. Gilbert and A. G. W. Cameron, Can. J. Phys. **43**, 1446 (1965).

[18] T. von Egidy and D. Bucurescu, Phys. Rev. C **80**, 054310 (2009).

[19] A. Bohr and B. Mottelson, *Nuclear Structure* (Benjamin, New York, 1969), Vol. I, p. 169.

[20] H. K. Toft *et al.*, Phys. Rev. C **81**, 064311 (2010).

[21] M. Baranger *et al.*, (Plenum Press, New York **7**, 1973).

[22] R. Capote *et al.*, RIPL-3-Reference Input Parameter Library for Calculation of Nuclear Reactions and Nuclear Data Evaluations, Nucl. Data Sheets 110, 3107 (2009). Available online at [http://www-nds.iaea.org/RIPL-3/].

[23] J. M. Blatt and V. F. Weisskopf, *Theoretical Nuclear Physics* (John Wiley and Sons, New York, 1952).

[24] C. Djalali *et al.*, Nucl. Phys. A **388**, 1 (1982).

[25] http://inpp.ohiou.edu/∼voinov/index.html, (2015 Dec).

[26] W. Greiner and J. A. Maruhn, *Nuclear Models*, (Springer, 1996).

[27] J. Speth and J. Wambach, *Electric and Magnetic Giant Resonances in Nuclei*, (World Scientific Publishing Co. Pte. Ltd **7**, 1991).

[28] W. Ziegler *et al.*, Phys. Rev. Lett. **65**, 2515 (1990).

[29] D. Savran *et al.*, Progress in Particle and Nuclear Physics **70**, 210 (2013).

[30] K. Heyde *et al.*, Rev. Mod. Phys. **82**, 2365 (2010).

[31] A.C. Larsen *et al.*, Phys. Rev. C **76**, 044303 (2007).

[32] A. C. Larsen *et al.*, Phys. Rev. C **73**, 064301 (2006).

[33] A. C. Larsen *et al.*, Phys. Rev. C **85**, 014320 (2012).

[34] N. U. H. Syed *et al.*, Phys. Rev. C **80**, 044309 (2009).

[35] M. Guttormsen *et al.*, Phys. Rev. C **83**, 014312 (2011).

UNIVERSITY of the

[36] A. Voinov *et al.*, Phys. Rev. Lett. **93**, 14 (2004).

[37] A. C. Larsen *et al.*, Phys. Rev. Lett. **111**, 242504 (2013).

[38] M. Guttormsen *et al.*, Phys. Rev. C. **71**, 044307 (2005).

[39] A. C. Larsen *et al.*, Phys. Rev. C. **87**, 014319 (2013).

[40] M. Wiedeking *et al.*, Phys. Rev. Lett. **108**, 162503 (2012).

[41] R. Schwengner *et al.*, Phys. Rev. Lett. **111**, 232504 (2013).

[42] B. A. Brown and A. C. Larsen Phys. Rev. Lett. **113**, 252502 (2014).

[43] E. Litvinova and N. Belov, Phys. Rev. C. **88**, 031302(R) (2013).

[44] D. M. Brink, Ph.D. thesis, Oxford University, 1955, pp. 101-110.

[45] J. Kopecky and M. UHL, Phys. Rev. C. **41**, 1941 (1990).

[46] J. Kopecky and R. E. Chrien, Nucl. Phys. A **468**, 285 (1987).

[47] J. Kopecky *et al.*, Phys. Rev. C. **47**, 312 (1993).

[48] A. C. Larsen and S. Goriely, Phys. Rev. C. **82**, 014318 (2010).

UNIVERSITY of the
WESTERN CAPE

[49] S. Goriely, Phys. Lett. B. **436**, 10 (1998).

[50] S. Goriely and M. Arnould, A&A. **312**, 327 (1996).

[51] S. Goriely *et al.*, A&A **487**, 467 (2008).

[52] M. Thoennessen (MSU) adopted from S. Goriely, Phys. Lett. B. **436**, 10 (1998).

[53] H. T. Nyhus, PhD thesis, University of Oslo, 2014.

[54] D. Belkic, *Principles of Quantum Scattering Theory*, (Institute of Physics Publishing, 2004).

[55] A. Schiller *et al.*, Nucl. Instrum. Methods Phys. Res. A **447**, 498 (2000).

[56] A. C. Larsen *et al.*, Phys. Rev. C. **83**, 034315 (2011).

[57] M. Guttormsen *et al.*, Nucl. Instrum. Methods Phys. Res. A **374**, 371 (1996).

[58] M. Guttormsen *et al.*, Nucl. Instrum. Methods Phys. Res. A **255**, 518 (1987).

[59] A. C. Larsen, PhD thesis, University of Oslo, 2008.

[60] E. Fermi, *Nuclear Physics*, (University of Chicago Press, Chicago, 1950).

[61] L. Henden *et al.*, Nucl. Phys. A **589**, 249 (1995).

[62] H. T. Nyhus *et al.*, Phys. Rev. C **81**, 024325 (2010).

[63] Data taken from the NNDC database [http://www.nndc.bnl.gov/chart/], (Dec. 2015).

[64] B. V. Kheswa, PhD thesis, Stellenbosch University, 2014.

[65] M. Guttormsen *et al.*, Nucl. Instrum. Methods Phys. Res. A **648**, 168 (2011).

[66] G. M. Tveten, PhD thesis, University of Oslo, 2013.

[67] M. Guttormsen *et al.*, Phys. Scr. **T32**, 54 (1990).

[68] https://unarydigits.com/jkinz/

[69] W. R. Leo *et al.*, *Techniques for Nuclear and Particle Physics Experiments*, (Springer-Verlag, New York, 1994) 2^{nd} revised ed.

[70] V. C. Rogers *et al.* Nucl. Phys. A **144**, 81 (1970).

[71] L. Bernard *et al.* Phys. Rev. C **123**, 283 (1961).

[72] S. F. Mughabghab, *Atlas of Neutron Resonances*, (Elsevier Science, Amsterdam, 2006). 5^{th} ed.

[73] S. Siem *et al.*, Phys. Rev. C **65**, 044318 (2002).

[74] H. T. Nyhus *et al.*, Phys. Rev. C **85**, 014323 (2012).

[75] H. Utsunomiya *et al.*, Phys. Rev. C **67**, 015807 (2003).

[76] R. Bergere *et al.*, Nucl. Phys. A **121**, 463 (1968).

[77] A. Makinaga *et al.*, Phys. Rev. C **90**, 044301 (2014).

[78] L. G. Moretto *et al.*, arXiv:1406.2642 [nucl-th] (2015).

[79] C. P. Brits, MSc thesis, Stellenbosch University, to be submitted in 2016.

[80] K. Wisshak *et al.*, Phys. Rev. C **69**, 055801 (2004).

[81] Z. Y. Bao *et al.*, *Atomic Data and Nuclear Data Tables* **76**, 70 (2000).

UNIVERSITY of the WESTERN CAPE

Appendix A

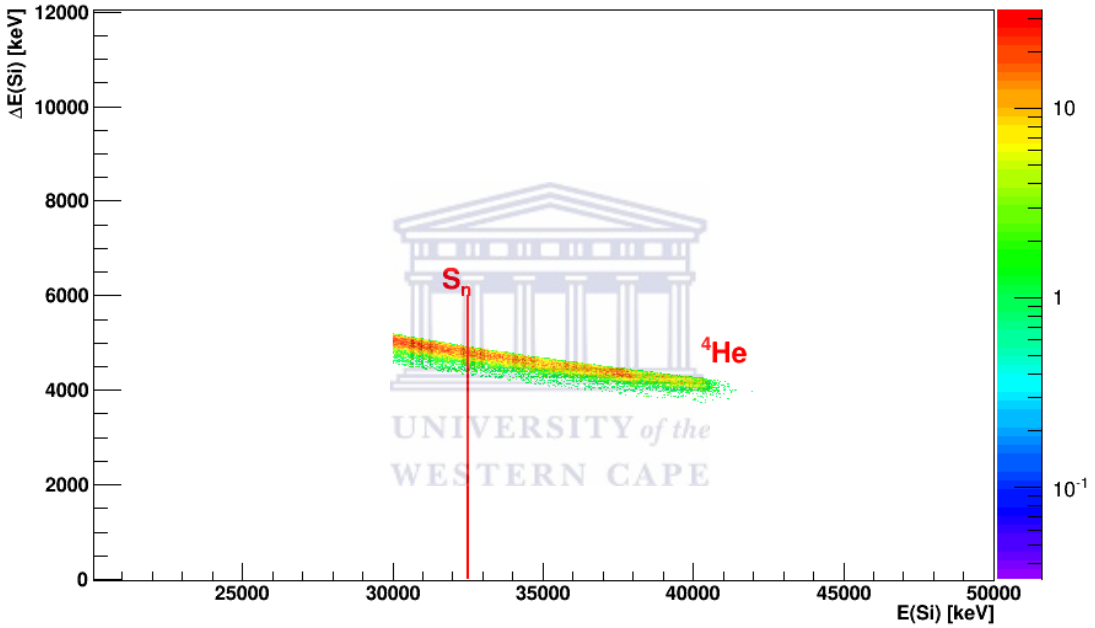

Figure 6.1. The ^{4}He banana gate was cut off around S_n to select only high-energy ^{4}He particles which are more effectively collected in the $\Delta E - E$ telescopes to provide a good TDC start signal.

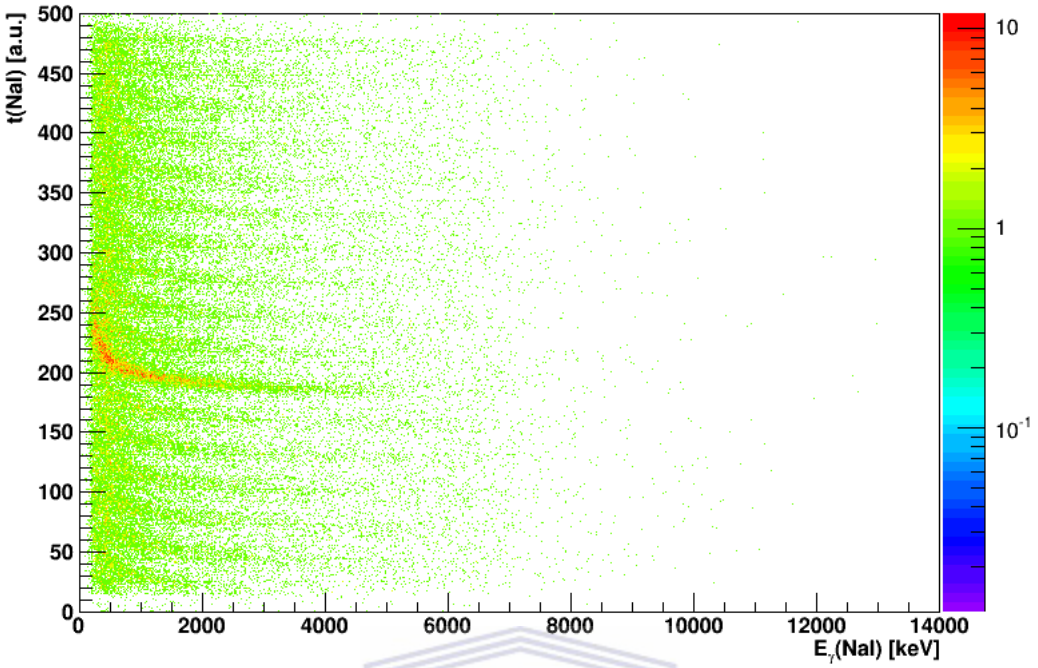

Figure 6.2. The energy-time matrix for the ^{181}Ta(^{3}He, $\alpha\gamma$)^{180}Ta reaction of the CACTUS array.

UNIVERSITY of the
WESTERN CAPE

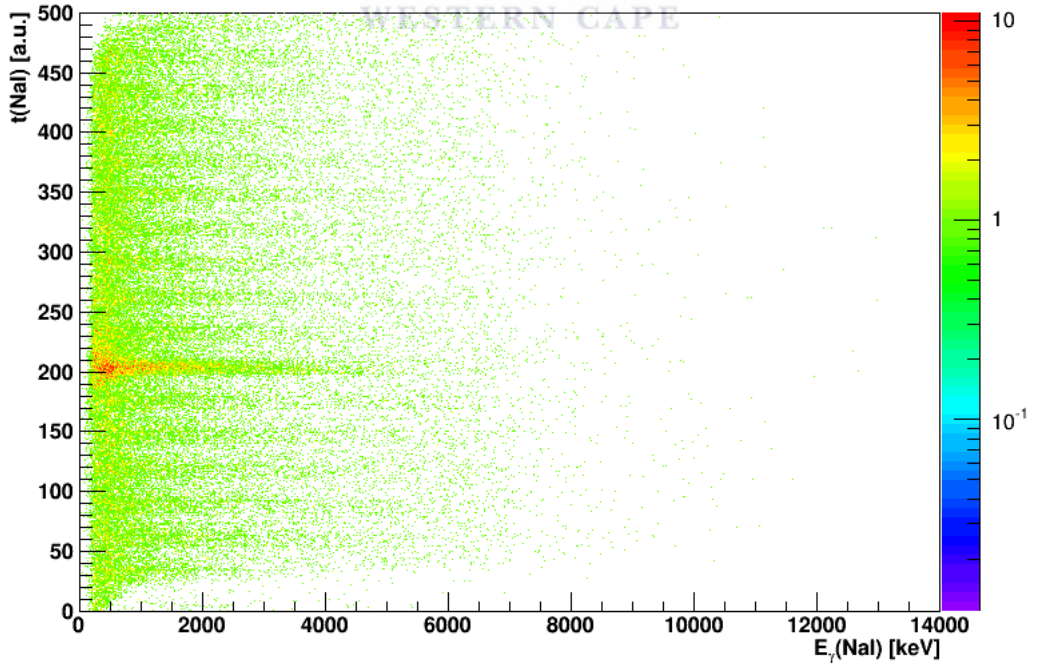

Figure 6.3. The energy-time matrix from the ^{181}Ta(^{3}He, $\alpha\gamma$)^{180}Ta reaction after *walk* correction for the CACTUS array.

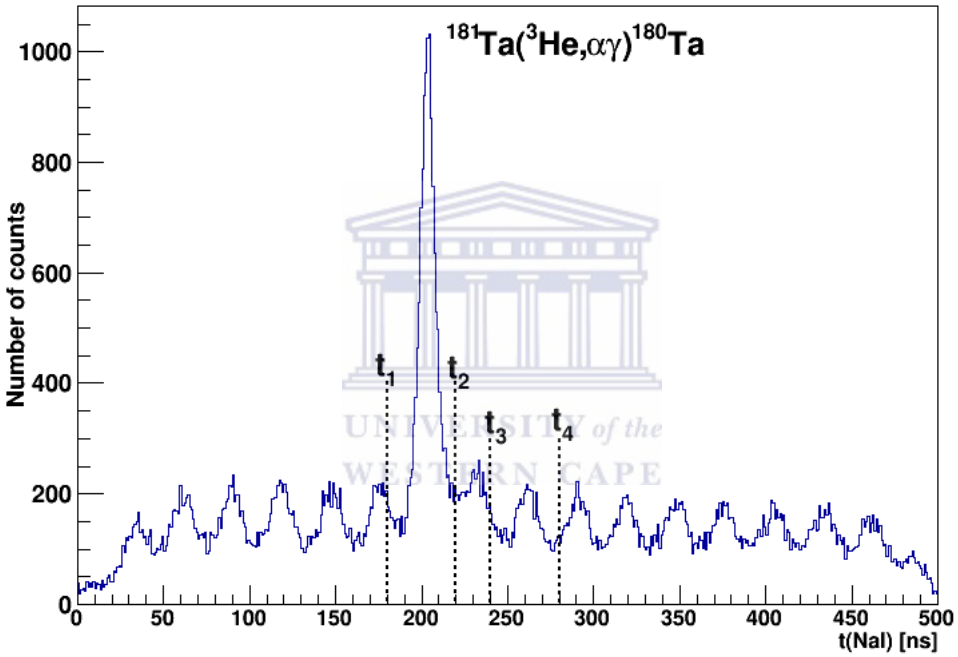

Figure 6.4. The projection of figure 6.3 on the time-axis after signals were time calibrated from CACTUS. The dashed lines (t_1, t_2) and (t_3, t_4) are gates on the prompt and random events, respectively, with same width

Appendix B: Tables

Table. 6.1. The ^{181}Ta and ^{180}Ta γ-ray strength function data extracted according to the Oslo method, using the (^{3}He, $\alpha\gamma$) and (^{3}He, ^{3}Heγ), respectively. $f_{upper}(E_\gamma)$ and $f_{lower}(E_\gamma)$ represent the upper and lower error bands of the γ-ray strength function as explained in the text.

^{181}Ta

No	E_γ(MeV)	$f(E_\gamma) \pm \Delta\ f(E_\gamma)$ (MeV^{-3})	$f_{upper}(E_\gamma)$	$f_{lower}(E_\gamma)$
1	1.585	1.716e-08 ± 1.049e-09	9.068e-10	8.967e-10
2	1.899	1.984e-08 ± 9.084e-10	9.926e-10	9.617e-10
3	2.210	2.345e-08 ± 1.103e-09	1.114e-09	1.058e-09
4	2.523	2.828e-08 ± 1.395e-09	1.367e-09	1.271e-09
5	2.835	3.436e-08 ± 1.739e-09	1.740e-09	1.585e-09
6	3.147	4.052e-08 ± 2.243e-09	2.526e-09	2.256e-09
7	3.460	5.228e-08 ± 3.067e-09	3.639e-09	3.183e-09
8	3.772	6.678e-08 ± 4.414e-09	4.780e-09	4.097e-09
9	4.085	8.325e-08 ± 6.667e-09	7.737e-09	6.498e-09
10	4.397	9.525e-08 ± 1.080e-08	1.217e-08	1.001e-08
11	4.709	1.241e-07 ± 1.452e-08	1.664e-08	1.341e-08
12	5.022	1.598e-07 ± 2.194e-08	2.279e-08	1.800e-08
13	5.334	1.641e-07 ± 3.463e-08	4.032e-08	3.120e-08
14	5.647	2.265e-07 ± 4.151e-08	5.423e-08	4.112e-08
15	5.959	4.189e-07 ± 9.039e-08	9.320e-08	6.924e-08
16	6.271	4.743e-07 ± 1.254e-07	1.556e-07	1.132e-07
17	6.585	4.727e-07 ± 1.980e-07	2.342e-07	1.670e-07
18	6.896	1.074e-06 ± 3.483e-07	4.335e-07	3.029e-07
19	7.209	1.276e-06 ± 5.841e-07	7.219e-07	4.943e-07

^{180}Ta

No	E_γ(MeV)	$f(E_\gamma) \pm \Delta\ f(E_\gamma)$ (MeV^{-3})	$f_{upper}(E_\gamma)$	$f_{lower}(E_\gamma)$
1	1.695	1.926e-08 ± 4.563e-09	4.714e-09	4.259e-09
2	2.085	1.909e-08 ± 3.993e-09	4.321e-09	3.601e-09
3	2.475	1.898e-08 ± 5.173e-09	5.864e-09	4.508e-09
4	2.865	2.658e-08 ± 6.769e-09	8.038e-09	5.700e-09
5	3.255	3.290e-08 ± 1.047e-08	1.302e-08	8.517e-09
6	3.645	3.902e-08 ± 1.229e-08	1.602e-08	9.665e-09
7	4.035	3.824e-08 ± 1.477e-08	2.016e-08	1.122e-08
8	4.425	6.753e-08 ± 2.472e-08	3.535e-08	1.815e-08
9	4.815	7.414e-08 ± 3.274e-08	4.904e-08	2.323e-08
10	5.205	7.383e-08 ± 5.210e-08	8.175e-08	3.572e-08
11	5.595	7.230e-08 ± 6.320e-08	1.039e-07	4.186e-08
12	5.985	1.049e-07 ± 1.252e-07	2.156e-07	8.016e-08
13	6.375	2.995e-07 ± 2.664e-07	4.804e-07	1.647e-07

UNIVERSITY of the WESTERN CAPE

Table. 6.2. The ^{181}Ta and ^{180}Ta nuclear level density, where $\rho_{upper}(E_x)$ and $\rho_{lower}(E_x)$ represent the upper and lower error bands of the nuclear level density as explained in the text.

	^{181}Ta			
No	E_x(MeV)	$\rho(E_x) \pm \Delta\rho(E_x)$ (MeV^{-1})	$\rho_{upper}(E_x)$	$\rho_{lower}(E_x)$
1	0.023	6.258e+00 ± 4.038e-01	3.779e-01	3.953e-01
2	0.336	1.228e+01 ± 5.950e-01	7.069e-01	7.244e-01
3	0.648	1.823e+01 ± 1.129e+00	1.167e+00	1.172e+00
4	0.961	3.247e+01 ± 2.310e+00	2.255e+00	2.218e+00
5	1.273	7.483e+01 ± 4.450e+00	4.454e+00	4.293e+00
6	1.585	1.770e+02 ± 8.719e+00	9.299e+00	8.781e+00
7	1.898	3.457e+02 ± 2.070e+01	2.176e+01	2.013e+01
8	2.210	5.777e+02 ± 3.581e+01	4.322e+01	3.918e+01
9	2.523	1.124e+03 ± 7.533e+01	9.263e+01	8.227e+01
10	2.835	2.178e+03 ± 1.459e+02	1.551e+02	1.350e+02
11	3.147	4.105e+03 ± 3.242e+02	3.424e+02	2.919e+02
12	3.460	7.137e+03 ± 5.214e+02	5.945e+02	4.966e+02
13	3.772	1.223e+04 ± 1.208e+03	1.399e+03	1.145e+03
14	4.085	2.195e+04 ± 2.258e+03	2.834e+03	2.273e+03
15	4.397	3.798e+04 ± 4.708e+03	4.992e+03	3.922e+03
16	4.709	7.370e+04 ± 1.066e+04	1.059e+04	8.154e+03
17	5.022	1.317e+05 ± 2.487e+04	2.713e+04	2.047e+04
18	5.334	1.807e+05 ± 5.293e+04	6.236e+04	4.609e+04
19	5.647	4.715e+05 ± 1.638e+05	2.132e+05	1.544e+05
	^{180}Ta			
No	E_x(MeV)	$\rho(E_x) \pm \Delta\rho(E_x)$ (MeV^{-1})	$\rho_{upper}(E_x)$	$\rho_{lower}(E_x)$
1	0.135	4.721e+01 ± 1.305e+01	1.243e+01	1.354e+01
2	0.525	9.352e+01 ± 2.477e+01	2.473e+01	2.484e+01
3	0.915	1.668e+02 ± 4.894e+01	5.119e+01	4.742e+01
4	1.305	4.212e+02 ± 9.891e+01	1.084e+02	9.261e+01
5	1.695	8.862e+02 ± 2.076e+02	2.382e+02	1.878e+02
6	2.085	1.446e+03 ± 5.354e+02	6.437e+02	4.680e+02
7	2.475	2.256e+03 ± 1.008e+03	1.269e+03	8.511e+02
8	2.865	7.138e+03 ± 2.344e+03	3.092e+03	1.913e+03
9	3.255	9.995e+03 ± 4.913e+03	6.790e+03	3.875e+03
10	3.645	1.732e+04 ± 1.068e+04	1.546e+04	8.138e+03
11	4.035	4.232e+04 ± 2.336e+04	3.542e+04	1.720e+04
12	4.425	4.871e+04 ± 4.688e+04	7.447e+04	3.336e+04
13	4.815	1.032e+05 ± 1.534e+05	2.552e+05	1.055e+05

UNIVERSITY of the WESTERN CAPE